

Editorial corner – a personal view

Nanocellulose – a renewable polymer of bright future

J. V. Seppälä*

Aalto University, Department of Biotechnology and Chemical Technology, PO Box 16100, FI-00076 Aalto, Finland

Cellulose is the most abundant polymer in the world – by nature and by using renewable feedstock! One third of all plant material is cellulose and it is estimated to be the most common organic substance. Only a fraction of cellulose is utilized, mainly for lumber and papermaking. How could we utilize this renewable polymer in a better way?

One highly interesting option is to produce nanoscale cellulose fibers in different forms: fractal branched nanofibers, crystalline rod-shaped nanowhiskers or bacterially produced nanocellulose. Such nanofibrillated cellulose is expectedly ultra-strong and has in addition several other interesting properties like super-hydrophilicity and interesting rheological properties. [Chem. Soc. Rev., DOI: [10.1039/c0cs00108b](https://doi.org/10.1039/c0cs00108b)] Nanofibrillated cellulose (NFC) is in its basic form a dilute aqueous dispersion. This dispersion has interesting and applicable rheological properties, for example the flock formation properties are unique [J. Polym. Environ., DOI: [10.1007/s10924-010-0248-2](https://doi.org/10.1007/s10924-010-0248-2), Cellulose, DOI: [10.1007/s10570-011-9597-9](https://doi.org/10.1007/s10570-011-9597-9)]. To use nanocellulose in concentrated forms, in composites or as films, it usually needs to be chemically modified. Thus the chemistries that enable reactions in aqueous systems are highly interesting in this connection. One can mention Ce-catalysed free radical reactions based on the glucose ring opening, leading to the possibility of free radical graft co-polymerization. This chemical approach has enabled synthesis of thermoplastic, film forming and hydrophobic nanocellulose grades [Carbohydrate Polymers, DOI: [10.1016/J.CARBPOL.2010.12.064](https://doi.org/10.1016/J.CARBPOL.2010.12.064)].

Another interesting aqueous reaction family is the click chemistry in aqueous phase through which several functionalities can be attached to the nano-

cellulose. For example, amine functional nanocellulose grades have been synthesized that in a second stage have formed a covalent bond with functionalized graphene [J. Mater. Chem., DOI: [10.1039/C1JM12134K](https://doi.org/10.1039/C1JM12134K), Cellulose, DOI: [10.1007/s10570-011-9573-4](https://doi.org/10.1007/s10570-011-9573-4)]. Thus conductive cellulose nano composites have been produced utilizing the high surface area and fractal structure of the nanocellulose. Third feasible approach has been to chemically modify nanocellulose at the interphase of a two phase liquid system, where anhydride monomers are dissolved into an organic solvent and react at the interphase with the aqueous dispersion of nanocellulose. As a result, hydrophobic nanocellulose grades even super hydrophobic ones have been successfully produced.

Very interesting property of nanocellulose is its barrier properties as films or coatings. Extremely low permeabilities of oxygen have been reported, especially in dry conditions.

Nanocellulose is an excellent example of renewable natural material that enable a fine platform for polymer scientists to develop novel functional materials. Such not only are eco-friendly, but also show novel functional properties, which exceed those of today's synthetic polymers.



Prof. Dr. Jukka Seppälä
Member of International Advisory Board

*Corresponding author, e-mail: jukka.seppala@aalto.fi
© BME-PT

Rubber composite fibers containing silver nanoparticles prepared by electrospinning and *in-situ* chemical crosslinking

Q. Hu¹, H. Wu¹, L. Zhang¹, H. Fong², M. Tian^{1*}

¹State Key Laboratory of Organic-Inorganic Composites, Beijing University of Chemical Technology, Chao-Yang District, 100029 Beijing, China

²Department of Chemistry, South Dakota School of Mines and Technology, Rapid City, 57701 South Dakota, USA

Received 8 July 2011; accepted in revised form 19 October 2011

Abstract. Rubber composite fibers containing silver nanoparticles with high morphological stability were prepared through combination of electrospinning and *in-situ* chemical crosslinking. The composite fibers included those of Ag/polybutadiene rubber (BR), Ag/polyisobutylene-isoprene rubber (IIR), and Ag/silicon rubber (SiR). During the study, Ag nanoparticles (Ag NPs) were first generated through reducing the Ag⁺ ions in rubber/N,N-dimethylformamide/tetrahydrofuran solutions upon ultraviolet-irradiation; subsequently, rubber composite fibers with uniform diameters from hundreds of nanometers to several micrometers were made by electrospinning the above solutions. The electrospinning was carried out with *in-situ* chemical crosslinking. The results indicated that chemical crosslinking during (and shortly after) electrospinning was able to improve substantially the morphological stability of rubber fibers. As indicated by the results acquired from UV absorption spectroscopy, X-ray photoelectron spectroscopy and transmission electron microscope, Ag nanoparticles with sizes of 10~20 nm were uniformly dispersed in rubber fibers. It was believed that, in addition to the protection of polyvinyl pyrrolidone, a rapid solvent evaporation and limited motion space for a very fine fiber during electrospinning could prevent/mitigate the aggregation of Ag NPs, resulting in a very uniform dispersion. The electrospun Ag NPs/BR composite fibers made of the solution containing very low loading amount (3 wt%) of AgNO₃ demonstrated strong antimicrobial activity.

Keywords: rubber, electrospinning, composite fiber, silver nanoparticles, *in-situ* crosslinking

1. Introduction

Recently, the incorporation of metal nanoparticles into polymer nanofibers has attracted growing attentions, because this type of nanocomposite nanofibers would combine the unique properties of metal nanoparticles (*e.g.*, magnetic, optical, electronic, catalytic, and antimicrobial properties) with the outstanding characteristics of polymer nanofibers (*e.g.*, the high specific surface area and high interpenetrating capacity in other materials, *etc.*) [1–8]. Among various metal nanoparticles, silver nanoparticles (Ag NPs) have been of particular interest due

to their catalytic property, high electrical conductivity, and antimicrobial activity etc [9–12]. Ag NPs have been synthesized in many different ways including chemical reduction, X-ray irradiation, refluxing and heating methods and bio-reduction [13–15]. Nevertheless, Ag NPs have the tendency to form agglomerates; and thus it has been a technological challenge how to disperse them uniformly in polymeric matrices.

To the best of our knowledge, the polymers that have been electrospun into nanofibers with Ag NPs are mostly thermoplastics such as polyvinyl pyrrolidone

*Corresponding author, e-mail: tian71402@126.com
© BME-PT

done (PVP), polyvinyl acetate (PVA), polyacrylonitrile (PAN), *etc.* [17–20]; whereas electrospun Ag NPs/rubber composite fibers have rarely been reported [21]. This is probably due to the reason that rubbers have glass transition temperatures lower than room temperature, and the excellent elasticity might hinder the formation of fibers during electrospinning. Additionally, the macromolecular chains of rubbers are able to move (*i.e.*, rearrange their conformations) in electrospun fibers, such a movement and/or relaxation occurs when the stretching force no longer exists, and is driven by entropy increase. The results often include the breakage and/or conglutination of fibers with prolonging the storage time [22, 23].

It is expected that the rubber fibers would be important for applications in need of large deformation and elasticity. For example, silicon rubber (SiR) and isobutylene-isoprene rubber (IIR) exhibit excellent biocompatibility and low gas permeability in addition to superior elasticity. Herein, three kinds of rubbers including butadiene rubber (BR), IIR, and SiR were studied. *N,N*-dimethylformamide (DMF) was selected as a co-solvent for three rubbers, as well as the reducing agent for converting Ag^+ ions into Ag NPs. The resulting solutions containing Ag NPs were directly used for electrospinning. To improve the morphological stability of Ag NPs/rubber composite fibers, the *in-situ* chemical crosslinking was conducted during and shortly after electrospinning; camphorquinone (CQ) was used as the

UV-photo initiator for BR and IIR, whereas a curing agent containing the catalyst of platinum was used for SiR. The addition of PVP into the Ag^+ /rubber solutions aimed to prevent the Ag NPs from agglomeration, as well as to promote the reduction of Ag^+ ions into Ag NPs.

2. Experimental part

2.1. The preparation of Ag NPs/rubber composite fibers

The preparation process is shown in the Figure 1. AgNO_3 and PVP ($M=1\ 300\ 000$) (mass ratio of AgNO_3 /PVP being 1/1, 1 wt% to rubber), supplied by the Beijing Hua-Teng Chemical Reagent Co. (Beijing, China) and Alfa Co. (America), respectively, were dissolved in *N,N*-dimethylformamide (DMF) and the solution was then added to the solvent of tetrahydrofuran (THF) (mass ratio of THF/DMF being 4/1) drop by drop. Polybutadiene rubber (BR), supplied by the Beijing Yan-Shan Petrochemical Co. (Beijing, China), was first kneaded on a two-roll mill at $\sim 25^\circ\text{C}$ for 10 min. Subsequently, 8 wt% of BR was dissolved in the above THF/DMF solutions. The BR solution was then exposed to ultraviolet irradiation for about 1 h for the reduction of Ag^+ ions into Ag NPs. Prior to electrospinning, camphorquinone (CQ) was added into the solutions for *in-situ* photo-crosslinking. Finally, the solutions were filled in 30 mL plastic syringes having blunt-end stainless-steel needles with inside diameter of 0.30 mm. The electrospinning setup included an

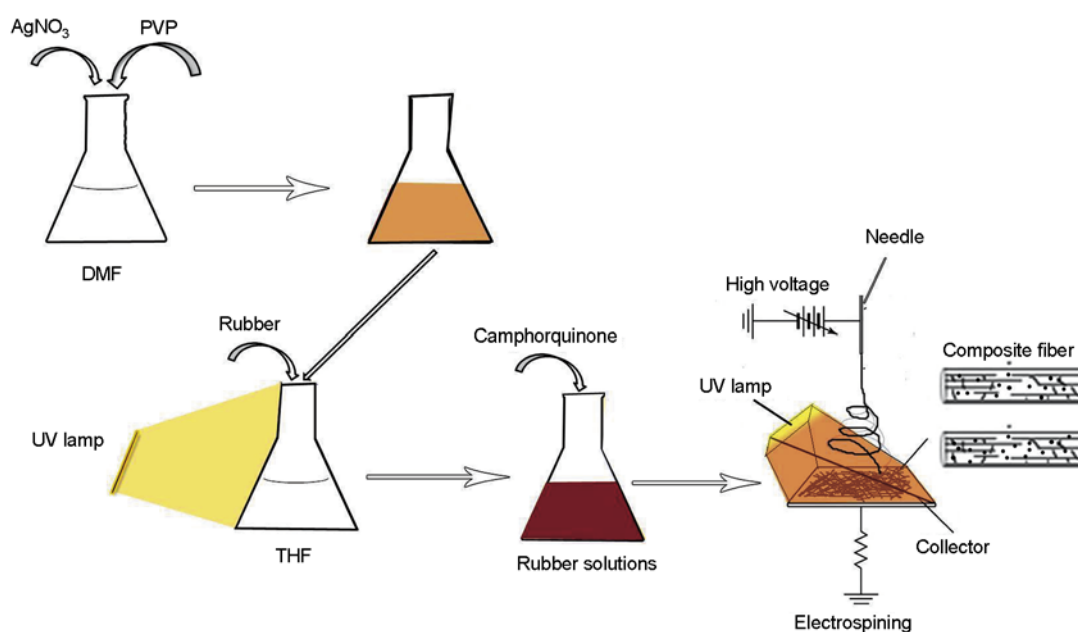


Figure 1. Schematic diagram of experimental process

ES30P high voltage power supply, purchased from the Gamma High Voltage Research, Inc. (Ormond Beach, USA), and a fiber collector of electrically grounded metal plate covered with aluminum foil. The collector was placed at 15~20 cm below the needle and exposed to a 100 W halogen lamp. During electrospinning, a positive high voltage of 10~20 kV was applied to the needle; and the solution feed-rate of 1.5 mL/h was maintained using a syringe pump. Isobutylene-isoprene rubber (IIR), also supplied by the Beijing Yan-Shan Petrochemical Co., had a similar process of electrospinning as BR. Silicon rubber (SiR), supplied by the Dow Corning Co. (USA), also had a similar process of electrospinning as BR except that a curing agent containing the catalyst of platinum (PL-10A: 4%, PL-10B: 6%, SiR: 20%) was chosen for *in-situ* chemical crosslinking.

2.2. Characterization of Ag NPs/rubber composite fibers

For morphological characterizations, electrospun BR, IIR and SiR fibers were collected with glass slides on the metal plate; and the fibers were examined with XSJ-2 optical microscope purchased from the Chongqing Optical Instrument Co. (Chongqing, China). UV absorption spectrum of the Ag/BR fiber mat in the 300–700 nm region was obtained by the UV-3150 spectrophotometer purchased from the Shimadzu Co. (Shimadzu, Japan) and a piece of aluminum foil covering with Ag/BR fiber mat was used for UV measurement. A piece of Ag/BR fiber mat was placed on a copper grid to observe the shape and distribution of silver nanoparticles in electrospun Ag NPs/BR composite fiber by H-800 transmission electron microscopy purchased from Hitachi Co. (Japan). XPS measurements were carried out on an ESCALAB 250 purchased from Thermo Electron Corporation (USA) with an Al K α X-ray source at 1486.6 eV photons. The core-level signals were obtained at a photoelectron take off angle of 45° (with respect to the sample surface). The X-ray source was run at a reduced power of 150 W.

2.3. Antimicrobial activity test of Ag/BR composite fibers

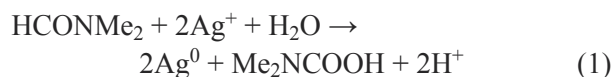
The antimicrobial activity of BR composite fibers with and without Ag NPs was tested against Gram-negative Escherichia coli (E.coli, ATCC 25922) according to Chinese national testing standard of

antimicrobial activity in the ‘Technical Standard For Disinfection’ (2002). For antimicrobial activity characterization, the randomly overlaid fiber mats were obtained by collecting ~1 mg of BR fibers (with and without Ag NPs) with glass slides (25 mm × 25 mm). The agar plates containing test samples and the control (BR fibers without Ag NPs) were incubated at 37°C for 24 h. The reductions of bacteria were calculated according to the equation of ‘Reduction [%] = (B – A)/B · 100’, where A and B are the surviving cells (colony forming unit. mL⁻¹) for the plates containing test samples and the control, respectively.

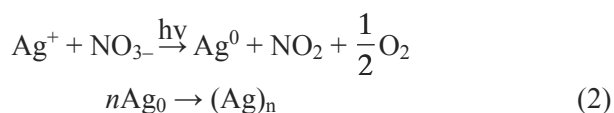
3. Results and discussion

3.1. In-situ formation of silver nanoparticles

In this study, DMF was used as a reducing agent for converting Ag⁺ ions into Ag NPs. During the reactions performed at room temperature, the following reaction according to Equation (1) would occur:



However, the reaction would proceed at a low rate when performed at room temperature. In this study, we obtained the quick *in-situ* synthesis of Ag NPs in the rubber solution with further ultraviolet irradiation. The following reaction given by Equation (2) took place during the ultraviolet irradiation process:



The reduction of Ag⁺ ions by DMF could be monitored from the color evolution of the solution. Visual observation showed that, as the reaction proceeded, the color shifted from light yellow, bright yellow, to dark brown after 10, 30, 60 min, respectively, as depicted in Figure 2. In this study, we also introduced PVP into the rubber solution in order to protect the Ag NPs from agglomeration; so that they could be uniformly dispersed in electrospun composite fibers. The fast evaporation of solvent during the process of electrospinning also prevented from Ag NPs self-aggregation in the rubber fibers because of very limited space. The absorption spectrum of Ag/rubber composite fiber mat is shown in Figure 3 and it can be seen that an absorption band with a sharp maximum at about 424 nm arises. Small metal-

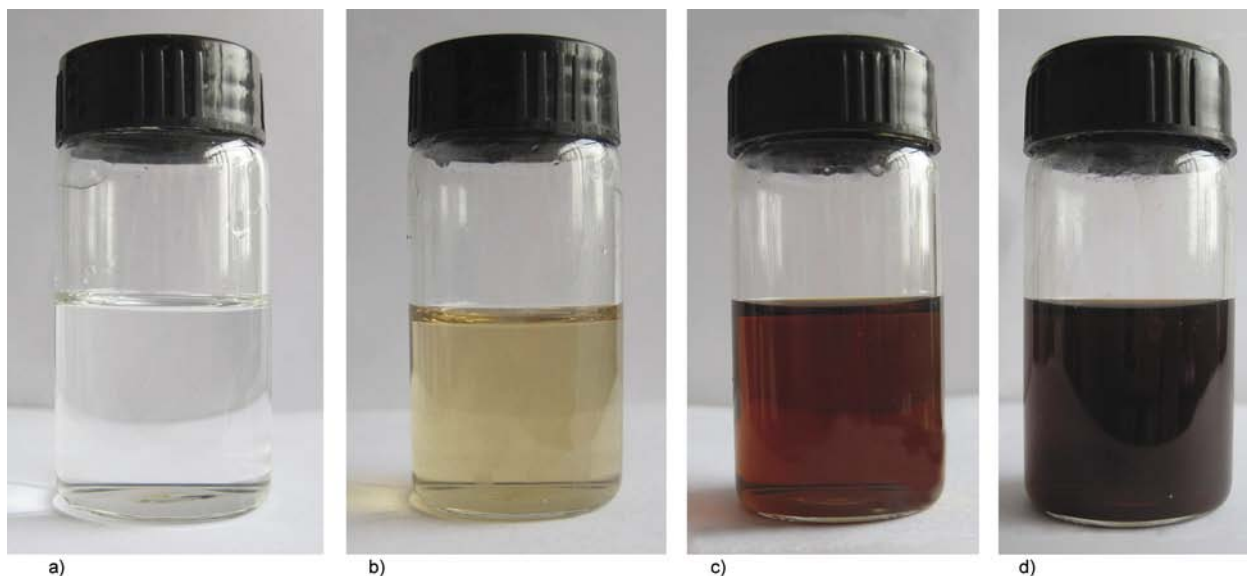


Figure 2. Color evolution of AgNO_3/DMF solution with ultraviolet irradiation for varied time periods of (a) 0 min, (b) 10 min, (c) 30 min, and (d) 60 min

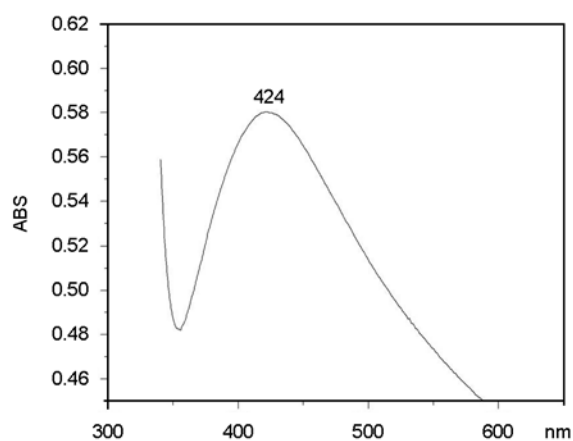


Figure 3. UV spectrum of Ag NPs/BR composite fiber mat prepared from the solution containing 3 wt% AgNO_3

lic particles exhibit a high optical absorbance due to the existence of discrete energy levels of electron and particularly of specific states. Ag NPs with diameters below 5 nm have a rather high absorbance band with a maximum at about 400 nm and with diameters of ~ 10 nm exhibit absorption bands at 410–450 nm depending on their chemical environment. Based on the maximal absorbance at 424 nm caused by Ag/rubber fiber mat, small spherical particles of silver with diameters of 10 nm or less were formed. Figure 4 showed the spectrum in the Ag 3d region of the Ag/rubber composite fibers. It was evident from the spectrum that two peaks occurred at 368.1 and 374.1 eV, corresponding to Ag 3d_{1/2} and 3d_{3/2} binding energies, respectively. The result further confirmed the existence of Ag(0) in the Ag/rubber composite fiber mat [24, 25].

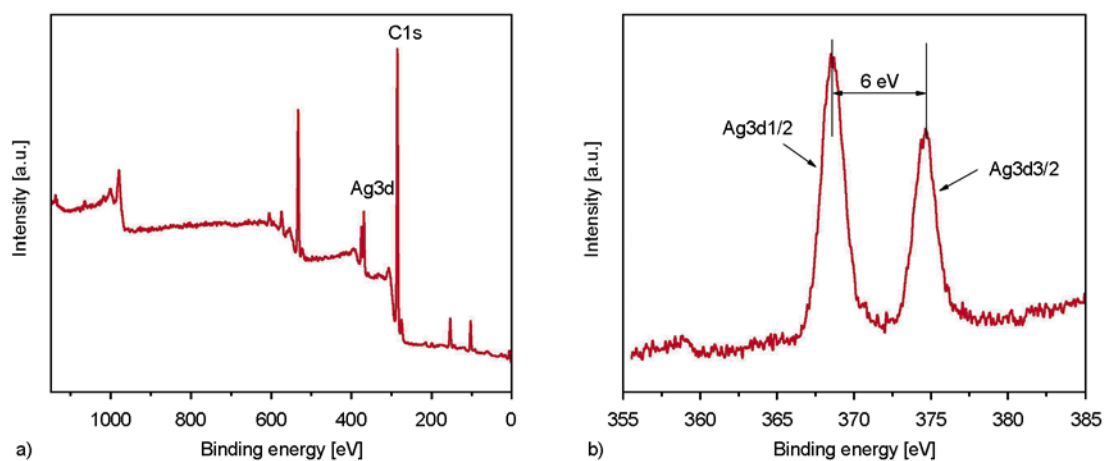


Figure 4. Wide-scan and Ag3d XPS spectra for electrospun Ag NPs/BR composite fiber mat prepared from the solution containing 3 wt% AgNO_3 : (a) wide-scan, (b) Ag3d

3.2. Morphology of Ag/rubber composite fibers

To investigate the morphological stability of electrospun rubber fibers (here only taking BR as an example), the prepared fibers were stored under ambient condition or immersed in THF (a good solvent for BR) (with temperature being $\sim 25^{\circ}\text{C}$ and relative humidity being $\sim 50\%$) for a period of time ~ 20 h. As shown in Figure 5, the Ag/BR composite fibers immediately after electrospinning possessed the cylindrical morphology, while the morphology was partially lost after storage under ambient condition, further prolonging the storage time led to the conglutination and/or breakage of the fibers for 20 h as seen in Figure 5d. When soaked in THF for 20 h, the electrospun Ag/BR composite fiber were completely dissolved (Figure 5e). Upon a series of experiments, the optimal mass ratio of CQ in BR was identified at 5%, the crosslinked Ag/BR composite fibers still well-retained their morphology even soaked in THF for 20 h; the fibers were merely swollen to a certain degree (Figure 5f). It could be concluded that *in-situ* chemical crosslinking during and shortly after electrospinning was able to substantially improve the morphological stability of electrospun BR fibers. During electrospinning, macromolecular chains in the spinning solution are stretched and/or aligned by electric force; simultaneously, the solvent in the electrospinning jet evaporates rapidly. Unlike thermoplastics, BR has the glass transition temperature (T_g) of about -105°C . The macro-

molecular movement and/or relaxation occur when the stretching force no longer exists, so the BR fibers will collapse, conglutinate, even break. In this study, the method of *in-situ* chemical crosslinking combined with electrospinning was established to obtain electrospun rubber composite fibers with stable morphology. The chemically cross-linked network might restrain the motion of rubber chains and extend molecular relaxation time [26–28], so the substantially improved morphological stability of electrospun rubber composite fibers was achieved.

We also prepared morphologically stable electrospun Ag NPs/IIR and Ag NPs/SiR composite fibers successfully through the combination of electrospinning and *in-situ* chemical crosslinking. Similar to BR, prior to electrospinning, CQ for IIR and platinum-containing curing agent for SiR were added into the solutions for *in-situ* chemical crosslinking. The TEM images in Figure 6 showed the morphologies of crosslinked Ag NPs/IIR and Ag NPs/SiR composite fibers made of 15 min kneaded IIR and as-received SiR. The chemically crosslinked Ag NPs/SiR composite fibers possessed approximately cylindrical morphology with uniform diameters of $1\sim 2\ \mu\text{m}$. The diameters of Ag NPs/BR and Ag NPs/IIR composite fibers were $\sim 400\ \text{nm}$, which was smaller than the diameters of Ag NPs/SiR composite fiber because SiR is the most elastic rubber. The typical TEM images of the rubber composite fibers containing Ag NPs are shown in Figure 6.

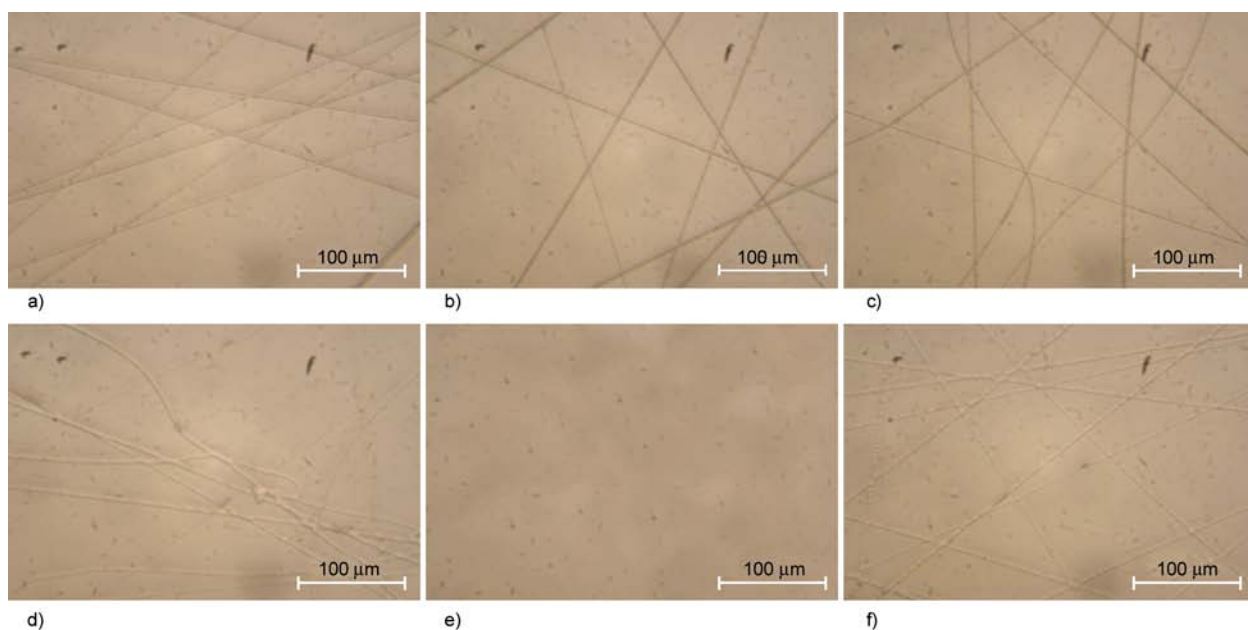


Figure 5. Optical microscope images showing the morphological variations of electrospun Ag NPs/BR composite fibers (un-crosslinked: a, b, d, e; crosslinked: c, f; immediately after electrospinning: a–c; kept for 20 h under ambient condition: d; and immersion in THF for 20 h: e, f)

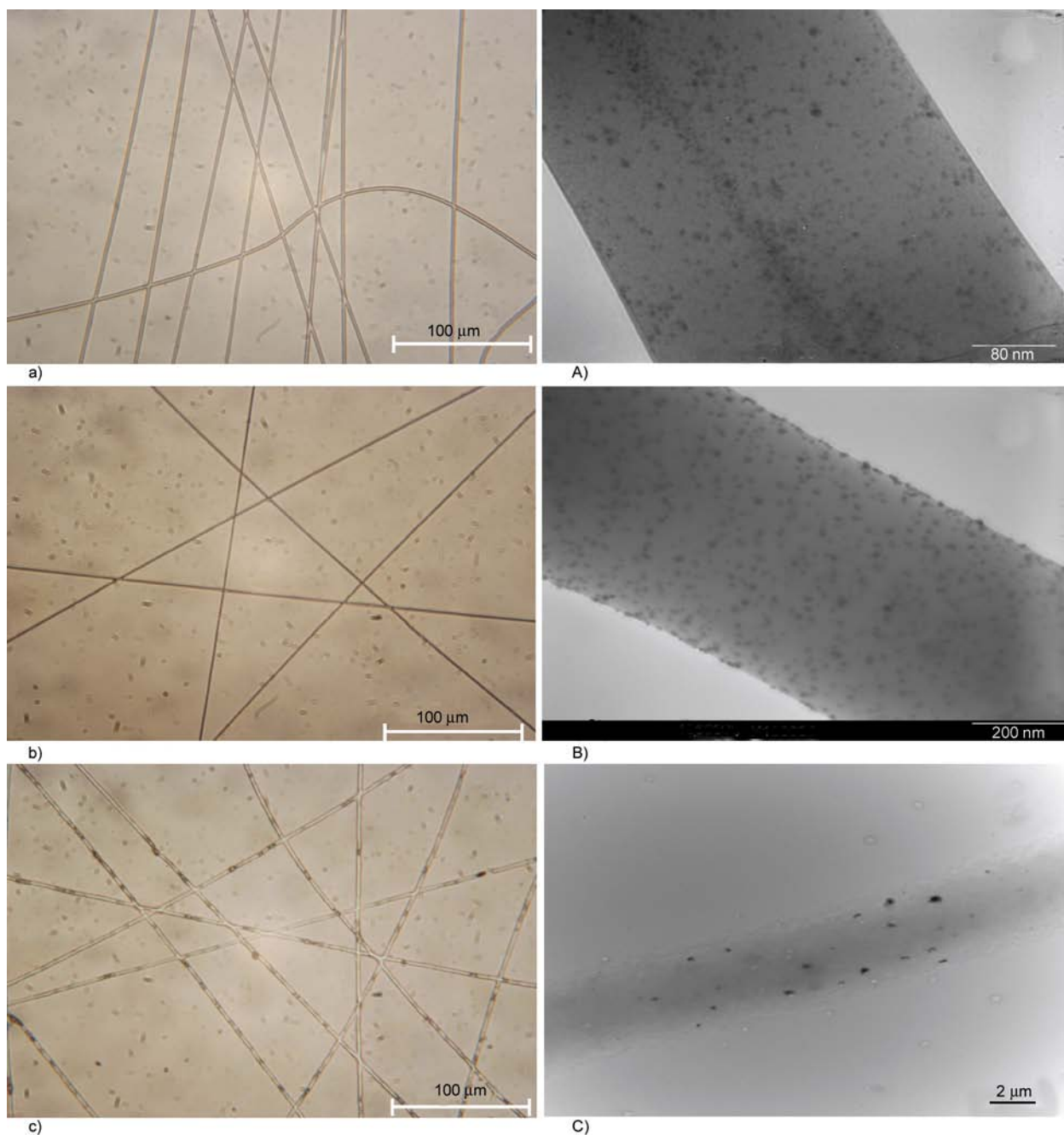


Figure 6. Optical microscope images (a–c) and TEM images (A–C) of Ag NPs-containing composite fibers of rubbers including BR (a, A), IIR (b, B), and SiR (c, C)

The Ag NPs were uniformly dispersed/distributed in the composite fibers and the average diameter of Ag NPs was about 10–20 nm, which was consistent with the results acquired from UV absorption spectra. In this study, we used DMF as a reducing agent for converting Ag^+ ions into Ag NPs at room temperature and UV-irradiation to greatly improve the reaction speed. Different from traditional chemical reduction in solution compounding, besides the protection of PVP, a rapid solvent evaporation and limited motion space in a very fine fiber during

electrospinning could considerably mitigate the agglomeration of the Ag NPs, resulting in a very uniform dispersion and the narrow particle-size distribution as shown in Figure 6.

3.3. Antimicrobial performance of Ag NPs/rubber composite fibers

It is likely that the nanoscale sizes of Ag NPs will allow the increase of contact surface with microorganisms, leading to an enhanced antimicrobial performance. In this study, to evaluate the antimicro-

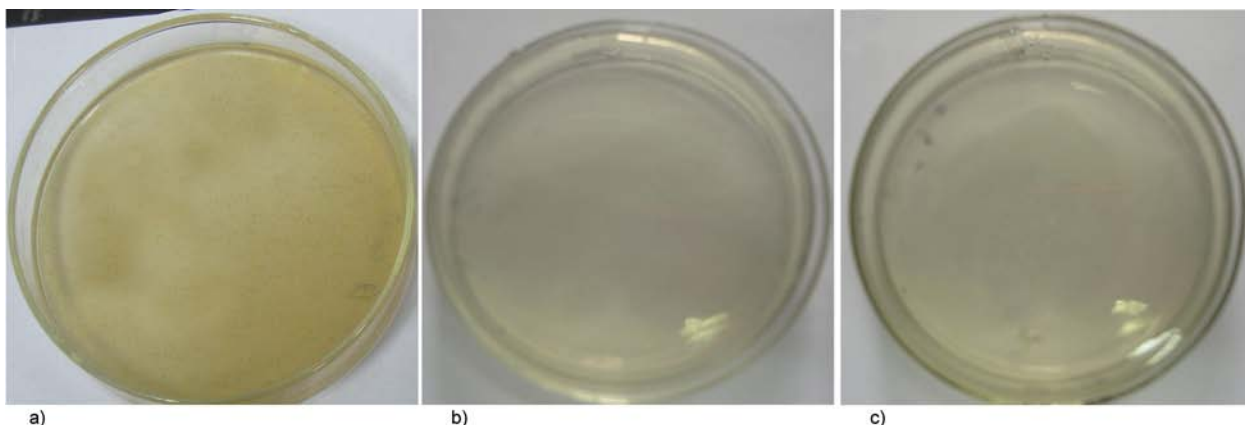


Figure 7. Antibacterial activity of Ag/BR composite fiber mats electrospun from the solutions with different AgNO₃ concentrations of (a) 0 wt% (b) 3 wt% (c) 5 wt% against Gram-negative Escherichia coli (E. coli, ATCC 25922)

bial activity of Ag NPs/BR composite fibers, the fiber mats were tested against E. coli according to the nonwoven fabric attachment method; and the results are shown in Figure 7. Bacteria reductions for the BR fiber mats electrospun from the solutions with the original concentration of AgNO₃ being 3 and 5 wt% were 99.9% after incubation. It is noteworthy that, if the conversion from Ag⁺ ions to Ag NPs could be 100%, the corresponding Ag NP concentrations in the above fiber mats would be ~1.9 and 3.2 wt%, respectively. This indicated that a small amount of Ag NPs in the composite fibers could introduce very strong antimicrobial activity.

4. Conclusions

The rubber (*i.e.*, BR, IIR, and SiR) composite fibers containing Ag NPs with high morphological stability were prepared through combination of electrospinning and *in-situ* chemical crosslinking. The crosslinked composite fibers could well retain their morphologies whether upon prolonged storage under ambient condition or even upon immersion in THF (a good solvent for BR, IIR, and SiR). The results from UV absorption spectroscopy and TEM revealed that Ag NPs with the average size of 10~20 nm were dispersed uniformly in the electrospun fibers. The results from XPS further confirmed the existence of Ag(0) in the composite fiber mats. This study also demonstrated that the rubber composite fibers containing a very amount of Ag NPs possessed strong antimicrobial activity.

Acknowledgements

This research was supported by the National Natural Science Foundation in China (Grant Number: 50873008); the authors would also acknowledge the Chang-Jiang Scholar program of the Ministry of Education in China (Grant Number: IRT0807).

References

- [1] Li D., McCann J. T., Gratt M., Xia Y.: Photocatalytic deposition of gold nanoparticles on electrospun nanofibers of titania. *Chemical Physics Letters*, **394**, 387–391 (2004). DOI: [10.1016/j.cplett.2004.07.044](https://doi.org/10.1016/j.cplett.2004.07.044)
- [2] Wang M., Singh H., Hatton T. A., Rutledge G. C.: Field-responsive superparamagnetic composite nanofibers by electrospinning. *Polymer*, **45**, 5505–5514 (2004). DOI: [10.1016/j.polymer.2004.06.013](https://doi.org/10.1016/j.polymer.2004.06.013)
- [3] Demir M. M., Gulgun M. A., Menceloglu Y. Z., Erman B., Abramchuk S. S., Makhaeva E. E., Khokhlov A. R., Matveeva V. G., Sulman M. G.: Palladium nanoparticles by electrospinning from poly(acrylonitrile-co-acrylic acid)-PdCl₂ solutions. Relations between preparation conditions, particle size, and catalytic activity. *Macromolecules*, **37**, 1787–1792 (2004). DOI: [10.1021/ma035163x](https://doi.org/10.1021/ma035163x)
- [4] Kedem S., Schmidt J., Paz Y., Cohen Y.: Composite polymer nanofibers with carbon nanotubes and titanium dioxide particles. *Langmuir*, **21**, 5600–5604 (2005). DOI: [10.1021/la0502443](https://doi.org/10.1021/la0502443)
- [5] Lu X., Zhao Y., Wang C., Wei Y.: Fabrication of CdS nanorods in PVP fiber matrices by electrospinning. *Macromolecular Rapid Communications*, **26**, 1325–1329 (2005). DOI: [10.1002/marc.200500300](https://doi.org/10.1002/marc.200500300)
- [6] Zhu J., Wei S., Rutman D., Haldolaarachchige N., Young D. P., Guo Z.: Magnetic polyacrylonitrile-Fe@FeO nanocomposite fibers – Electrospinning, stabilization and carbonization. *Polymer*, **52**, 2947–2955 (2011). DOI: [10.1016/j.polymer.2011.04.034](https://doi.org/10.1016/j.polymer.2011.04.034)

- [7] Zhu J., Wei S., Patil R., Rutman D., Kucknoor A. S., Wang A., Guo Z.: Ionic liquid assisted electrospinning of quantum dots/elastomer composite nanofibers. *Polymer*, **52**, 1954–1962 (2011).
DOI: [10.1016/j.polymer.2011.02.051](https://doi.org/10.1016/j.polymer.2011.02.051)
- [8] Zhu J., Wei S., Chen X., Karki A. B., Rutman D., Young D. P., Guo Z.: Electrospun polyimide nanocomposite fibers reinforced with core-shell Fe-FeO nanoparticles. *The Journal of Physical Chemistry C*, **114**, 8844–8850 (2010).
DOI: [10.1021/jp1020033](https://doi.org/10.1021/jp1020033)
- [9] Sondi I., Salopek-Sondi B.: Silver nanoparticles as antimicrobial agent: A case study on *E. coli* as a model for Gram-negative bacteria. *Journal of Colloid Interfaces Science*, **275**, 177–182 (2004).
DOI: [10.1016/j.jcis.2004.02.012](https://doi.org/10.1016/j.jcis.2004.02.012)
- [10] Balogh L., Swanson D. R., Tomalia D. A., Hagnauer G. L., McManus A. T.: Dendrimer-silver complexes and nanocomposites as antimicrobial agents. *Nano Letters*, **1**, 18–21 (2000).
DOI: [10.1021/nl005502p](https://doi.org/10.1021/nl005502p)
- [11] Dai J., Bruening M. L.: Catalytic nanoparticles formed by reduction of metal ions in multilayered polyelectrolyte films. *Nano Letters*, **2**, 497–501 (2002).
DOI: [10.1021/nl025547l](https://doi.org/10.1021/nl025547l)
- [12] Jin W.-J., Lee H. K., Jeong E. H., Park W. H., Youk J. H.: Preparation of polymer nanofibers containing silver nanoparticles by using poly(*N*-vinylpyrrolidone). *Macromolecular Rapid Communications*, **26**, 1903–1907 (2005).
DOI: [10.1002/marc.200500569](https://doi.org/10.1002/marc.200500569)
- [13] Hong K. H.: Preparation and properties of electrospun poly(vinyl alcohol)/silver fiber web as wound dressings. *Polymer Engineering and Science*, **47**, 43–49 (2007).
DOI: [10.1002/pen.20660](https://doi.org/10.1002/pen.20660)
- [14] Huang H., Yuan Q., Yang X.: Preparation and characterization of metal-chitosan nanocomposites. *Colloids and Surfaces B: Biointerfaces*, **39**, 31–37 (2004).
DOI: [10.1016/j.colsurfb.2004.08.014](https://doi.org/10.1016/j.colsurfb.2004.08.014)
- [15] Murugadoss A., Chattopadhyay A.: A 'green' chitosan-silver nanoparticle composite as a heterogeneous as well as micro-heterogeneous catalyst. *Nanotechnology*, **19**, 015603/1–015603/9 (2008).
DOI: [10.1088/0957-4484/19/01/015603](https://doi.org/10.1088/0957-4484/19/01/015603)
- [16] Jin W.-J., Lee H. K., Jeong E. H., Park W. H., Youk J. H.: Preparation of polymer nanofibers containing silver nanoparticles by using poly(*N*-vinylpyrrolidone). *Macromolecular Rapid Communications*, **26**, 1903–1907 (2005).
DOI: [10.1002/marc.200500569](https://doi.org/10.1002/marc.200500569)
- [17] Jin W.-J., Jeon H. J., Kim J. H., Youk J. H.: A study on the preparation of poly(vinyl alcohol) nanofibers containing silver nanoparticles. *Synthetic Metals*, **157**, 454–459 (2007).
DOI: [10.1016/j.synthmet.2007.05.011](https://doi.org/10.1016/j.synthmet.2007.05.011)
- [18] Bai J., Li Y., Li M., Wang S., Zhang C., Yang Q.: Electrospinning method for the preparation of silver chloride nanoparticles in PVP nanofiber. *Applied Surface Science*, **254**, 4520–4523 (2008).
DOI: [10.1016/j.apsusc.2008.01.051](https://doi.org/10.1016/j.apsusc.2008.01.051)
- [19] Song T., Zhang Y., Zhou T., Lim C. T., Ramakrishna S., Liu B.: Encapsulation of self-assembled FePt magnetic nanoparticles in PCL nanofibers by coaxial electrospinning. *Chemical Physics Letters*, **415**, 317–322 (2005).
DOI: [10.1016/j.cplett.2005.09.035](https://doi.org/10.1016/j.cplett.2005.09.035)
- [20] Lu X., Li L., Zhang W., Wang C.: Preparation and characterization of Ag₂S nanoparticles embedded in polymer fibre matrices by electrospinning. *Nanotechnology*, **16**, 2233–2237 (2005).
DOI: [10.1088/0957-4484/16/10/043](https://doi.org/10.1088/0957-4484/16/10/043)
- [21] Abu Bakar N. H. H., Ismail J., Abu Bakar M.: Synthesis and characterization of silver nanoparticles in natural rubber. *Materials Chemistry and Physics*, **104**, 276–283 (2007).
DOI: [10.1016/j.matchemphys.2007.03.015](https://doi.org/10.1016/j.matchemphys.2007.03.015)
- [22] Fong H., Reneker D. H.: Elastomeric nanofibers of styrene-butadiene-styrene triblock copolymer. *Journal of Polymer Science Part B: Polymer Physics*, **37**, 3488–3493 (1999).
DOI: [10.1002/\(SICI\)1099-0488\(19991215\)37:24<3488::AID-POLB9>3.0.CO;2-M](https://doi.org/10.1002/(SICI)1099-0488(19991215)37:24<3488::AID-POLB9>3.0.CO;2-M)
- [23] Hao X., Bai C., Huang Y., Bi J., Zhang C., Cai H., Zhang X., Du L.: Preparation of *cis*-1,4-polyisoprene electrospun microfibers. *Macromolecular Materials and Engineering*, **295**, 305–309 (2010).
DOI: [10.1002/mame.200900284](https://doi.org/10.1002/mame.200900284)
- [24] Pattabi M., Rao K. M., Sainkar S. R., Sastry M.: Structural studies on silver cluster films deposited on softened PVP substrates. *Thin Solid Films*, **338**, 40–45 (1999).
DOI: [10.1016/S0040-6090\(98\)00970-5](https://doi.org/10.1016/S0040-6090(98)00970-5)
- [25] He S., Yao J., Xie S., Pang S., Gao H.: Investigation of passivated silver nanoparticles. *Chemical Physics Letters*, **343**, 28–32 (2001).
DOI: [10.1016/S0009-2614\(01\)00566-8](https://doi.org/10.1016/S0009-2614(01)00566-8)
- [26] Decker C., Zahouily K., Decker D., Nguyen T., Thi V.: Performance analysis of acylphosphine oxides in photoinitiated polymerization. *Polymer*, **42**, 7551–7560 (2001).
DOI: [10.1016/S0032-3861\(01\)00221-X](https://doi.org/10.1016/S0032-3861(01)00221-X)
- [27] Decker C., Nguyen T. T. V.: High-speed photocrosslinking of thermoplastic styrene-butadiene elastomers. *Journal of Applied Polymer Science*, **77**, 1902–1912 (2000).
DOI: [10.1002/1097-4628\(20000829\)77:9<1902::AID-APP6>3.0.CO;2-6](https://doi.org/10.1002/1097-4628(20000829)77:9<1902::AID-APP6>3.0.CO;2-6)
- [28] Phinyocheep P., Duangthong S.: Ultraviolet-curable liquid natural rubber. *Journal of Applied Polymer Science*, **78**, 1478–1485 (2000).
DOI: [10.1002/1097-4628\(20001121\)78:8<1478::AID-APP30>3.0.CO;2-K](https://doi.org/10.1002/1097-4628(20001121)78:8<1478::AID-APP30>3.0.CO;2-K)

Biodegradable polyesters reinforced with triclosan loaded polylactide micro/nanofibers: Properties, release and biocompatibility

L. J. del Valle,* A. Díaz, M. Royo, A. Rodríguez-Galán, J. Puiggali

Departament d'Enginyeria Química, Universitat Politècnica de Catalunya, Av. Diagonal 647, E-08028 Barcelona, Spain

Received 14 July 2011; accepted in revised form 19 October 2011

Abstract. Mechanical properties and drug release behavior were studied for three biodegradable polyester matrices (polycaprolactone, poly(nonamethylene azelate) and the copolymer derived from 1,9-nonanediol and an equimolar mixture of azelaic and pimelic acids) reinforced with polylactide (PLA) fibers. Electrospinning was used to produce suitable mats constituted by fibers of different diameters (i.e. from micro- to nanoscale) and a homogeneous dispersion of a representative hydrophobic drug (i.e. triclosan). Fabrics were prepared by a molding process, which allowed cold crystallization of PLA micro/nanofibers and hot crystallization of the polyester matrices. The orientation of PLA molecules during electrospinning favored the crystallization process, which was slightly enhanced when the diameter decreased. Incorporation of PLA micro/nanofibers led to a significant increase in the elastic modulus and tensile strength, and in general to a decrease in the strain at break. The brittle fracture was clearer when high molecular weight samples with high plastic deformation were employed.

Large differences in the release behavior were detected depending on the loading process, fiber diameter size and hydrophobicity of the polyester matrix. The release of samples with the drug only loaded into the reinforcing fibers was initially fast and then became slow and sustained, resulting in longer lasting antimicrobial activity. Biocompatibility of all samples studied was demonstrated by adhesion and proliferation assays using HEp-2 cell cultures.

Keywords: biodegradable polymers, reinforcements, mechanical properties, electrospinning, drug release

1. Introduction

Polymeric micro/nanofibers are highly interesting materials for applications such as tissue engineering and drug delivery because the large surface area to volume ratio affords interesting new properties [1–3]. Electrospinning is currently one of the most versatile processes for preparing such kind of fibers since it is applicable to a wide range of materials (e.g. synthetic and natural polymers) at a low cost and with high yield. Basically, electrospinning makes use of electrostatic forces (10–100 kV) to stretch a polymer dilute solution as it solidifies. In addition, this technique provides a huge material elongation

rate and significant reduction of the cross-sectional area [4, 5] (i.e. close to 1000 s^{-1} and 10^5 , respectively), which may affect the orientation of molecular chains within the fiber and strongly influence the mechanical properties of nanofibers [6, 7].

The use of reinforcing fillers and fibers in polymers to improve their mechanical properties is commonly encountered in polymer technology. Properties are strongly dependent on the fiber/matrix interface, and nanofibers should therefore deliver particularly good characteristics due to their high specific surface area. Electrospun fibers are highly promising candidates as reinforcing agents in the develop-

*Corresponding author, e-mail: luis.javier.del.valle@upc.edu

ment of advanced nanocomposites due to their continuity, orientation, inherent flexibility and potential high compatibility with polymer matrices. Thus, in recent years interest has extended to biodegradable materials reinforced with electrospun nanofibers [8–10].

Electrospun fibers can be easily loaded with pharmacologically active agents by adding the appropriate drug to the polymer solution prior to the electrospinning process. In this way, bioresorbable three-dimensional tissue scaffolding matrices as drug delivery platforms for therapeutic agents can be prepared. Moreover, results on the ability of different cells to adhere to and proliferate on fibrous scaffolds have encouraged application research in this area [11]. Efficient drug loaded materials must maintain their pharmacological activity throughout a prolonged period of time, the drug release pattern being mainly governed by the interactions between polymer and drug. In this work, we consider the possibility of achieving a sustained release by embedding mats constituted by drug loaded micro/nanofibers into a biodegradable polymeric matrix. In addition to the minimization of the Burst effect and the delay in the release, an improvement of mechanical properties and performance of the matrix is expected. Triclosan (2,4,4'-trichloro-2'-hydroxydiphenyl ether), a well known antimicrobial drug [12], was chosen as a model for studying the release behavior of a hydrophobic drug from polyester matrices having a high methylene content.

Aliphatic polyesters currently constitute the main family of biodegradable polymers despite generally lacking good thermal and mechanical properties. Polylactide (PLA) is a remarkable exception because of its high melting point (173–178°C) and tensile modulus (2.7–16 GPa) [13, 14].

In summary, the main goals of the present work concern to the use of electrospun polylactide micro/nanofibers as reinforcing materials of biocompatible polyester matrices with low mechanical performance and also to the evaluation of their use as drug delivery platforms to attain a sustained release. Specifically, polycaprolactone (PCL), poly(nonamethylene azelate) (P99) and poly(nonamethylene azelate-*co*-pimelate) (COP) were selected as matrices due to their different hydrophobicity, crystallinity and synthesis procedures (i.e. ring opening poly-

merization or melt polycondensation), which render samples with very different molecular weights.

2. Experimental section

2.1. Materials

Triclosan and polycaprolactone (M_w : 65 000 g/mol) were purchased from Sigma-Aldrich (St. Louis, USA). Polylactide, a product of Natureworks® (polymer 2002D), was kindly supplied by Nupik International (Polinyà, Spain). According to the manufacturer, this PLA has a D content of 4.25%, a residual monomer content of 0.3%, a density of 1.24 g/cc, a glass transition temperature (T_g) of 58°C and a melting point of 153°C.

Poly(nonamethylene azelate) and poly(nonamethylene azelate-*co*-pimelate) were synthesized by thermal polycondensation of azelaic acid or a mixture of azelaic and pimelic acids (1:1 molar ratio) with an excess of 1,9-nonanediol (2.2:1 molar ratio), and following a synthetic procedure that was applied for relative polyalkylene dicarboxylate [15–17]. Titanium tetrabutoxyde was used as a catalyst and the reaction was firstly performed in a nitrogen atmosphere at 150°C for 6 h and then in vacuum at 180°C for 18 h. Both polymers were purified by precipitation with ethanol of chloroform solutions (10 wt%). The polymerization yield was always close to 70%. Weight average molecular weights of 19 600 and 38 500 g/mol were determined by gel permeation chromatography (GPC) (using PMMA standards and 1,1,1,3,3,3-isopropanol as a solvent) for P99 and COP, respectively.

2.2. Electrospinning and fiber assembly

Polylactide (PLA) was electrospun from a chloroform-acetone mixture (2:1 v/v) using different polymer weight percentage (10–2.5%). The electrospun fibers were collected on a target placed at different distances from the syringe tip (inside diameter of 0.84 mm). The voltage was varied between 10 and 30 kV and applied to the collecting target using a high-voltage supply (Gamma High Voltage Research, ES30-5W) (Ormond Beach, FL, USA). The polymer solutions were delivered via a KDS100 infusion syringe pump from KD Scientific (Holliston, MA, USA) to control the mass-flow rate (from 0.5 to 10 mL/h). All electrospinning experiments were carried out at room temperature. Triclosan

loaded electrospun fibers were prepared under optimized conditions established for the corresponding polymer solutions. The triclosan weight percentage of these solutions was always 3 wt%.

PCL, P99 and COP matrices were prepared by pressing (25 Ton Ring Press, Research & Industrial Instruments Company, London, UK) approximately 300 mg of the appropriate polymer. The sample was placed into a flat mold covered with teflon sheets to avoid polymer adhesion to the mold. The PCL, P99 and COP samples were pre-heated at 10°C above their melting points (60, 67 and 61°C, respectively) for 3 min and using heating plates and a temperature controller (Graseby Specac, Kent, England). Pressure was progressively increased from 1 to 4 bar. Polymer films with a thickness close to 100 µm were recovered after cooling the mold to room temperature.

Matrices loaded with triclosan were prepared in a similar way with a homogeneous mixture previously prepared by solvent-casting. Specifically, 300 mg of the appropriate polymer and 9 mg (3 wt%) of triclosan were dissolved in 5 mL of acetone. The solvent was removed by evaporation at room temperature.

In order to prepare the reinforced matrices, electrospun PLA mats were cut into square pieces with the same lateral dimensions of the previously molded

polymer films. These PLA mats with a weight of ca. 400 mg were placed between the polyester films and pressed following the above indicated procedure (Figure 1). The reinforced material had a PLA weight percentage close to 40% and a thickness of approximately 330 µm

2.3. Measurements

Molecular weights were estimated by GPC (Shimadzu, model LC-8A) (Tokyo, Japan) equipped with an Empower computer program (Waters Corporation, Massachusetts, USA). A PL HFIP gel column (Polymer Lab) (Agilent Technologies Spain, S.L.; Madrid, Spain) and a refractive index detector (Shimadzu RID-10A) (Tokyo, Japan) were employed.

Optical morphological observations were performed using a Zeiss Axioskop 40 microscope (Carl Zeiss, Göttingen, Germany). Micrographs were taken with a Zeiss AxiosCam MRC5 digital camera. The diameter of the electrospun fibers was measured with a Philips TECNAI 10 transmission electron microscope (TEM) (Philips Electron Optics, Eindhoven, Holland) at an accelerating voltage of 80 kV. Fibers were directly electrospun over carbon coated grids. Inspection of fiber surfaces was conducted by scanning electron microscopy (SEM) using a Focus Ion Beam Zeiss Neon 40 instrument (Carl Zeiss, Göttingen, Germany). Carbon coating was accomplished by using a Mitec K950 Sputter Coater (endowed with a film thickness monitor $k150\times$) (Quorum Technologies Ltd., West Sussex, UK).

Mechanical properties were determined with a Zwick Z2.5/TN1S (Zwick/Roell; Ulm, Germany) testing machine in stress-strain tests carried out at a deformation rate of 10 mm/min. Measurements were performed on rectangular samples ($30\times 5\times 0.35\text{ mm}^3$) cut from the above melt-pressed pieces. The mechanical parameters were averaged from a minimum of six measurements for each polymer sample.

Contact angles were determined using the water drop method. Images of water drops (3 µl) on the surface of the films were recorded with a contact angle meter (Contact Angle System OCA 15+) (Dataphysics Instruments GmbH, Filderstadt, Germany) after stabilization (30 s). Image analysis and contact angle measurements were carried out with SCA20

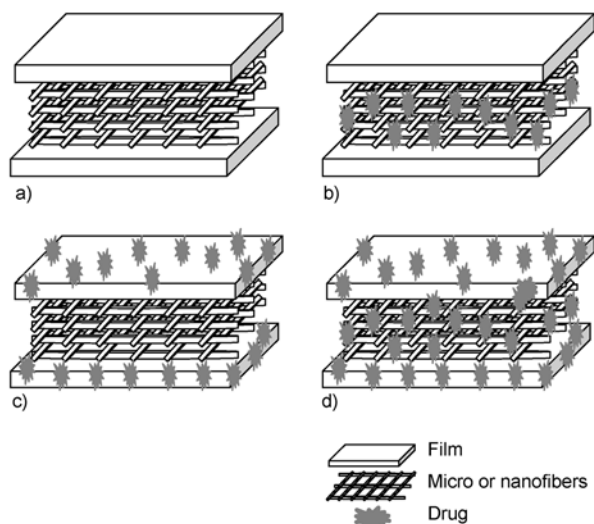


Figure 1. Schematic representation showing samples prepared by melt pressing a mat constituted by PLA micro/nanofibers between two films of PCL, P99 or COP biodegradable polyesters. Samples can be unloaded (a) or loaded with triclosan in the polylactide mat (b), the base polyester films (c) or both the polylactide mat and the base polyester films (d).

software. Values were averaged for each material over six measurements.

Wide angle X-ray diffraction (WAXD) patterns were acquired at the CRG beamline (BM16) of the European Synchrotron Radiation Facility of Grenoble. The beam was monochromatized to a wavelength of 0.098 nm. Samples were confined between Kapton films. WAXD profiles were acquired in time frames of 12 s during heating experiments performed at a rate of 3°C/min. The WAXD detector was calibrated with diffractions of a standard of an alumina (Al₂O₃) sample. Diffraction profiles were normalized to the beam intensity and corrected considering the empty sample background. WAXD peaks were deconvoluted with the PeakFit v4 program by Jandel Scientific Software.

2.4. Release experiments

Controlled release measurements were made with mats of electrospun samples and polyester/polylactide fabrics cut into square pieces (10 × 10 × 0.35 mm³). These were weighed and incubated at 37°C in an orbital shaker at 60 rpm in vessels with 50 mL of Sørensen medium (pH 7.4) containing an ethanol volume percentage of 70%. Triclosan concentration in the release medium was evaluated by UV spectroscopy using a UV-3600 (Shimadzu, Tokyo, Japan) UV-Vis-NIR spectrophotometer controlled by the UVProbe 2.31 software. Calibration curves were obtained by plotting the absorbance measured at 283 nm against triclosan concentration. Samples were drawn from the release medium at predetermined intervals and returned to the release vessel after measuring the absorbance. All drug release tests were carried out using six replicates to control the homogeneity of the release, and the results obtained from the samples were averaged. The total triclosan content in the samples was determined after extraction with chloroform.

2.5. Cell adhesion and proliferation test

HEp-2 cells (human laryngeal epidermoid carcinoma) were obtained from ATCC (Virginia, USA). HEp-2 cells were cultured in Dulbecco's Modified Eagle Medium (DMEM) supplemented with 10% foetal bovine serum, 50 U/mL penicillin, 50 µg/mL streptomycin and 2 mM L-glutamine at 37°C in a humidified atmosphere with 5% CO₂ and 95% air. The culture medium was changed every two days

and, for sub-culture, cell monolayers were rinsed with phosphate buffered saline (PBS) and detached by incubation with trypsin-EDTA (0.25%) at 37°C for 2–5 min. Cell concentration was determined by count with a Neubauer camera using 4% vital trypan-blue staining. Detached cells (viability ≥ 95%) were cultured under the conditions required for biocompatibility assays.

Electrospun fibers were collected on a glass coverslip (1.4 cm of diameter), and then placed on a 24-well culture plate (TCPS) and sterilized by UV irradiation for 15 min. The cells were exposed to direct contact with the material surface for evaluation of cell adhesion and proliferation.

Aliquots of 100 µl containing 5 · 10⁴ cells (for adhesion assay) or 2 · 10⁴ cells (for proliferation assay) were deposited onto fiber coated disks. The plate was incubated under culture conditions for 60 min to allow cell attachment to the material surface. Finally, 1 mL of the culture medium was added to each well. Cell adhesion and proliferation were monitored by culturing cells on the studied surfaces (e.g. TCPS control and polymer matrices).

Cell proliferation was evaluated by MTT (3-(4,5-dimethylthiazol-2-yl)-2,5-diphenyl-2H-tetrazolium bromide) after 7 days of culture. Cell adhesion was also evaluated by MTT after 24 h of culture and the results were normalized to surface unit (cm²). Five replicates were averaged and graphically represented for each independent experiment. ANOVA and Tukey tests were performed as statistical analysis at a confidence level of 95% (*p* < 0.05).

Fiber coated disks were fixed in 2.5% glutaraldehyde-PBS overnight at 4°C, dehydrated by washing in an alcohol battery (30, 50, 70, 90, 95 and 100°) at 4°C for 30 min per wash, and finally dyed with Giemsa 1% for observation in the optical microscope.

3. Results and discussion

3.1. Morphology of electrospun polylactide micro/nanofibers

Chloroform-acetone mixtures (2:1 v/v) with polymer weight percentages of 10 and 2.5% were successfully assayed and electrospinning parameters were optimized to obtain electrospun fibers with average diameters in the micrometer and nanometer scale (Figure 2), respectively. These diameter sizes were selected to compare reinforcing properties and

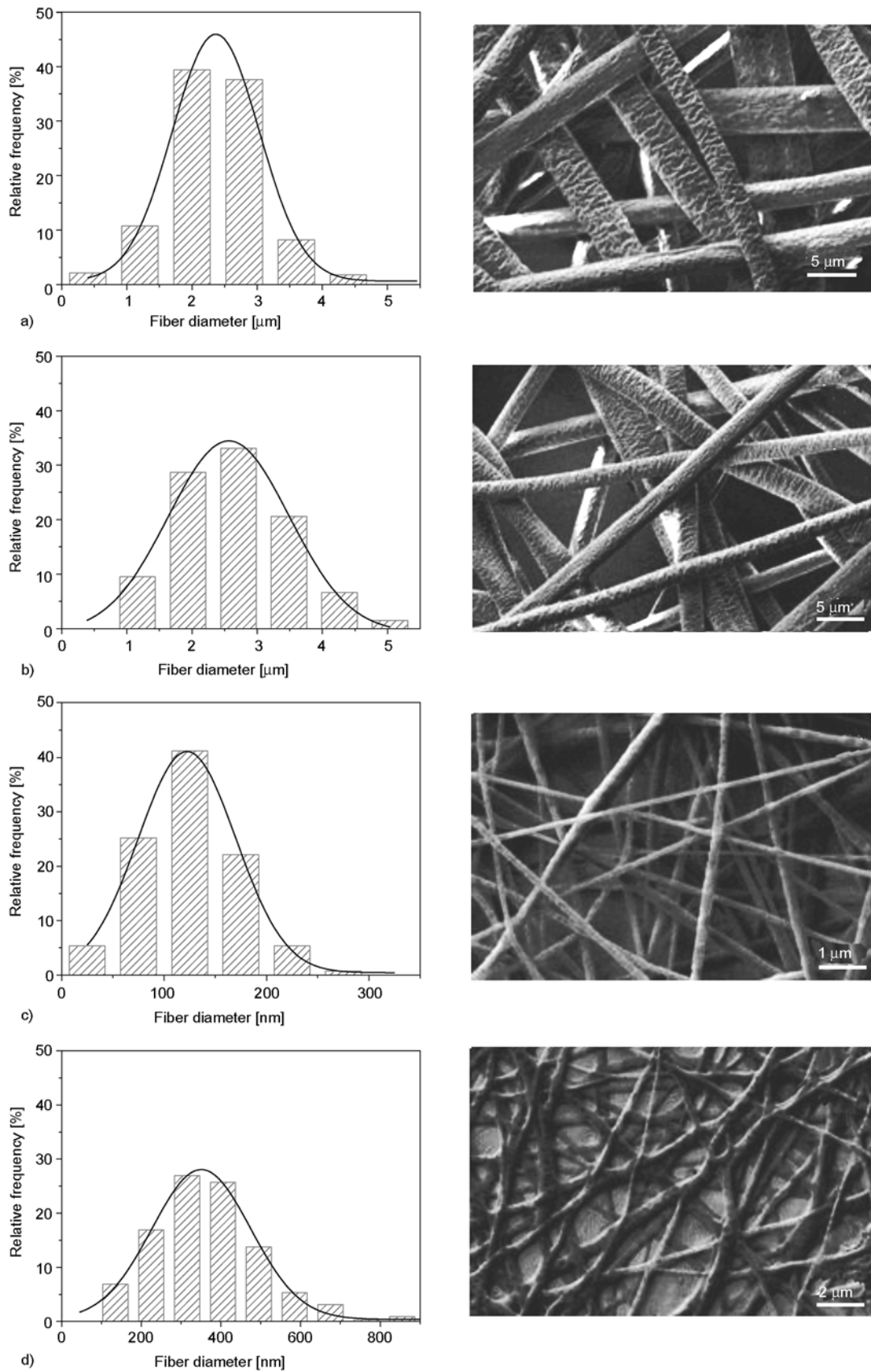


Figure 2. Fiber diameter distribution with Gaussian fitted functions (left) and SEM images (right) of: a) Electrospun PLA microfibers, b) Electrospun PLA microfibers loaded with 3 wt% of triclosan, c) Electrospun PLA nanofibers, d) Electrospun PLA nanofibers loaded with 3 wt% of triclosan.

triclosan release behavior. Accurate fiber diameter distributions were obtained by TEM micrographs using the standard software of the Philips TECNAI 10 electron microscope. Representative histograms of the diameter distributions are given in Figure 2. In all cases, a narrow monomodal distribution was observed and fitted to Gaussian curves which gave average diameters of 2.36 ± 0.01 , 2.56 ± 0.04 μm for unloaded and triclosan loaded microfibers and 122 ± 1 and 350 ± 4 nm for unloaded and triclosan loaded nanofibers. Specifically, the wide diameter range was attained by changing the polymer concentration, whereas tip-collector distance (12.5 cm), voltage (15 kV) and flow rate (10 mL/h) were crucial to obtain homogeneous fibers without electrospinning effect and bead formation. The spinning voltage (V) was carefully selected to ensure a stable conical liquid jet which also minimized bead formation. Note that the surface tension and solution viscosity, which also have a strong influence on fiber morphology, could not be modified since the solvent and polymer concentration remained unchanged for a given micrometer or nanometer diameter size. Once the voltage was optimized, the distance between the target and the syringe tip (h) was varied, and so was the flow rate (Φ), thus avoiding the coalescence favored by low rates. The diameters of unloaded and triclosan loaded microfibers were highly similar whereas loaded nanofibers were significantly thicker than unloaded ones (i.e. 350 nm versus

122 nm). SEM micrographs showed that in all cases microfibers had extremely rough surfaces with characteristic transversal striations whereas unloaded nanofibers showed relatively smooth surfaces that became rough with pores when triclosan was incorporated. The texture of microfibers suggests a dense lamellar stacking perpendicular to the fiber axis with amorphous regions between them [18].

3.2. Crystallinity of polyester matrices reinforced with PLA electrospun micro/nanofibers

The degree of crystallinity has a great influence on the mechanical properties of polymers and even on their drug release profiles. Thus, it has been found that release can be enhanced by increasing crystallinity, probably due to the increase in drug concentration in the amorphous phase and the partitioning of drug molecules to the sample surface [19]. Specifically, it has been demonstrated that the transformation from amorphous to semicrystalline of a PLA matrix leads to faster drug diffusion through the polymer matrix and an increase of the drug release rate [20]. Hence, the evaluation of the crystallinity of the studied samples is key considering that the preparation method should allow hot crystallization of the polyester matrix (i.e. by slow cooling from the melt state) and indeed cold crystallization of electrospun PLA micro/nanofibers (i.e. by the molding process performed at a temperature

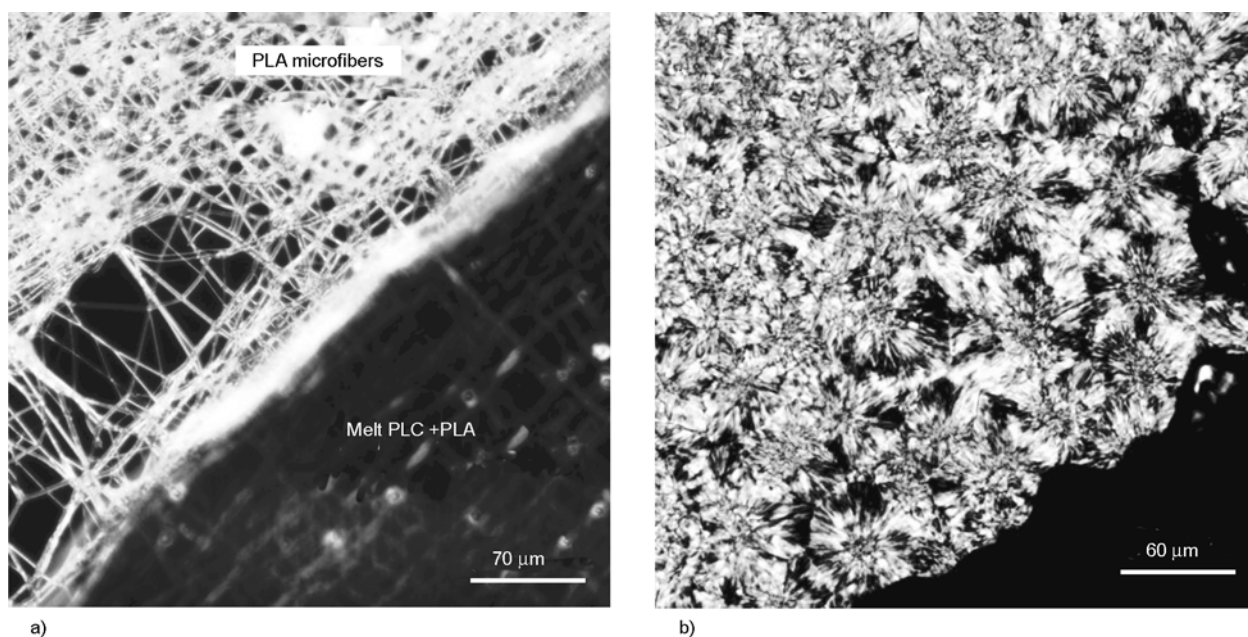


Figure 3. Polarizing optical micrographs showing PLA microfibers embedded into a melted PCL sample (a) and spherulitic morphologies obtained after cooling to room temperature (b)

higher than the PLA glass transition temperature). Optical micrographs of a fabric of polycaprolactone and electrospun PLA microfibers showed that the highly birefringent microfibers were preserved at the molding temperature and that the melted polyester matrix easily crystallized as negative spherulites when the sample was cooled ($3^{\circ}\text{C}/\text{min}$) to room temperature (Figure 3). A similar behavior was observed for preparations involving P99 or COP matrices.

WAXD profiles taken during heating scans of electrospun PLA samples (Figure 4a) showed that these were initially almost amorphous since only two predominant amorphous halos at 0.433 and 0.349 nm were detected. However, at higher temperatures three Bragg peaks gradually developed at 0.542, 0.472, and 0.403 nm, indicating crystallization of PLA into the well known α -form (10_3 helical conformation) since the observed peaks could be indexed as the corresponding (200)+(110), (203) and (015) reflections [21, 22]. Although PLA hardly crystallizes, it is clear that molecular chains attain a high unidirectional orientation during electrospinning, which makes feasible a subsequent reordering process on heating [23, 24]. The final degree of crystallinity was evaluated from the intensity of the above crystalline and amorphous reflections after deconvolution of the WAXD profile corresponding to the end of the cold crystallization process (Figure 4b). A slight increase in the degree of crystallinity was found when the fiber diameter decreased (i.e. 18 and 23% were determined for micro and nanofibers, respectively), suggesting that a higher molecular orientation was obtained from the dilute solutions chosen to produce nanofibers. X-ray diffraction patterns of PLA micro- and nanofibers loaded with triclosan (3 wt%) were different since characteristic triclosan reflections were only detected in the pattern of nanofibers (Figure 4c). Thus, drug molecules were well mixed in the PLA amorphous phase or formed independent crystalline domains depending on the fiber diameter size. Probably not all triclosan molecules could be incorporated in the nanofibers, and crystallized over their surface, in agreement with recent release studies.

Figure 5 compares the WAXD profiles of PCL, P99 and COP matrices containing PLA micro/nanofibers (i.e. after the molding process). In all cases, very intense reflections corresponding to each poly-

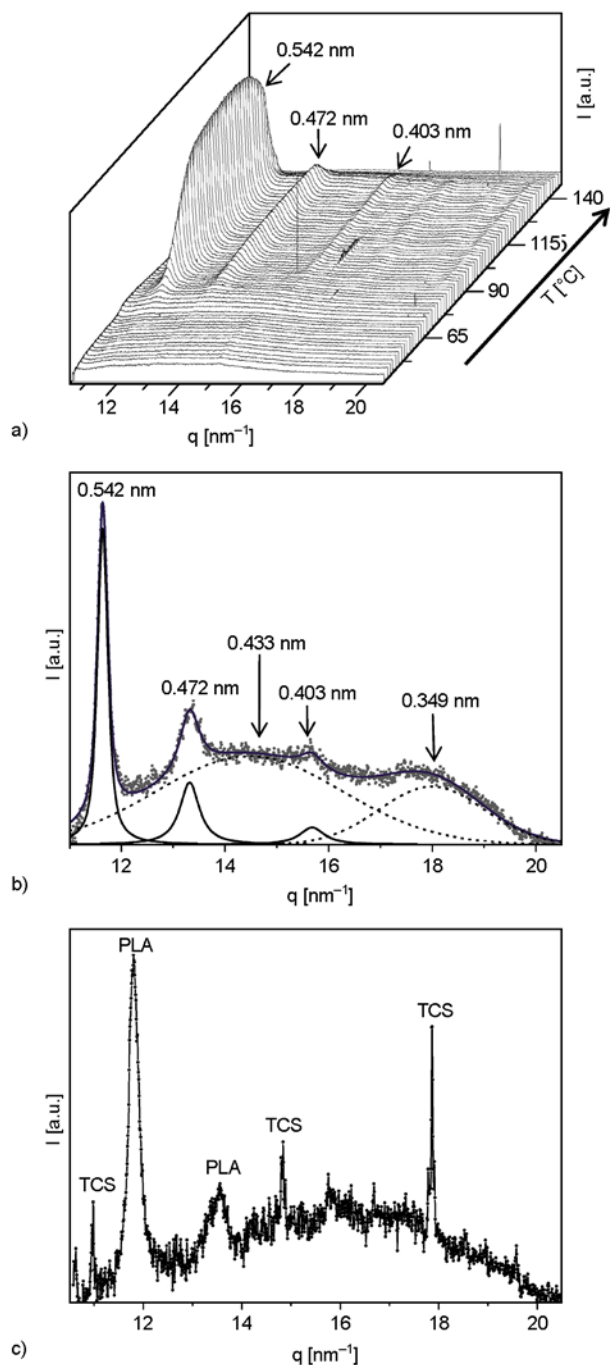


Figure 4. a) Three-dimensional WAXD profiles taken during a heating scan ($3^{\circ}\text{C}/\text{min}$) of a mat constituted by electrospun PLA nanofibers. b) WAXD profile corresponding to a cold crystallized mat of PLA nanofibers. Deconvoluted amorphous halos (dashed lines) and crystalline peaks (solid lines) are indicated, along with the corresponding simulated profiles (gray solid lines). c) WAXD profile corresponding to a cold crystallized mat of PLA nanofibers loaded with triclosan where characteristic peaks of triclosan crystals (TCS) can be observed. Abscise axis corresponds to the scattering vector ($q = 2\pi/d_B$, where d_B is the Bragg spacing).

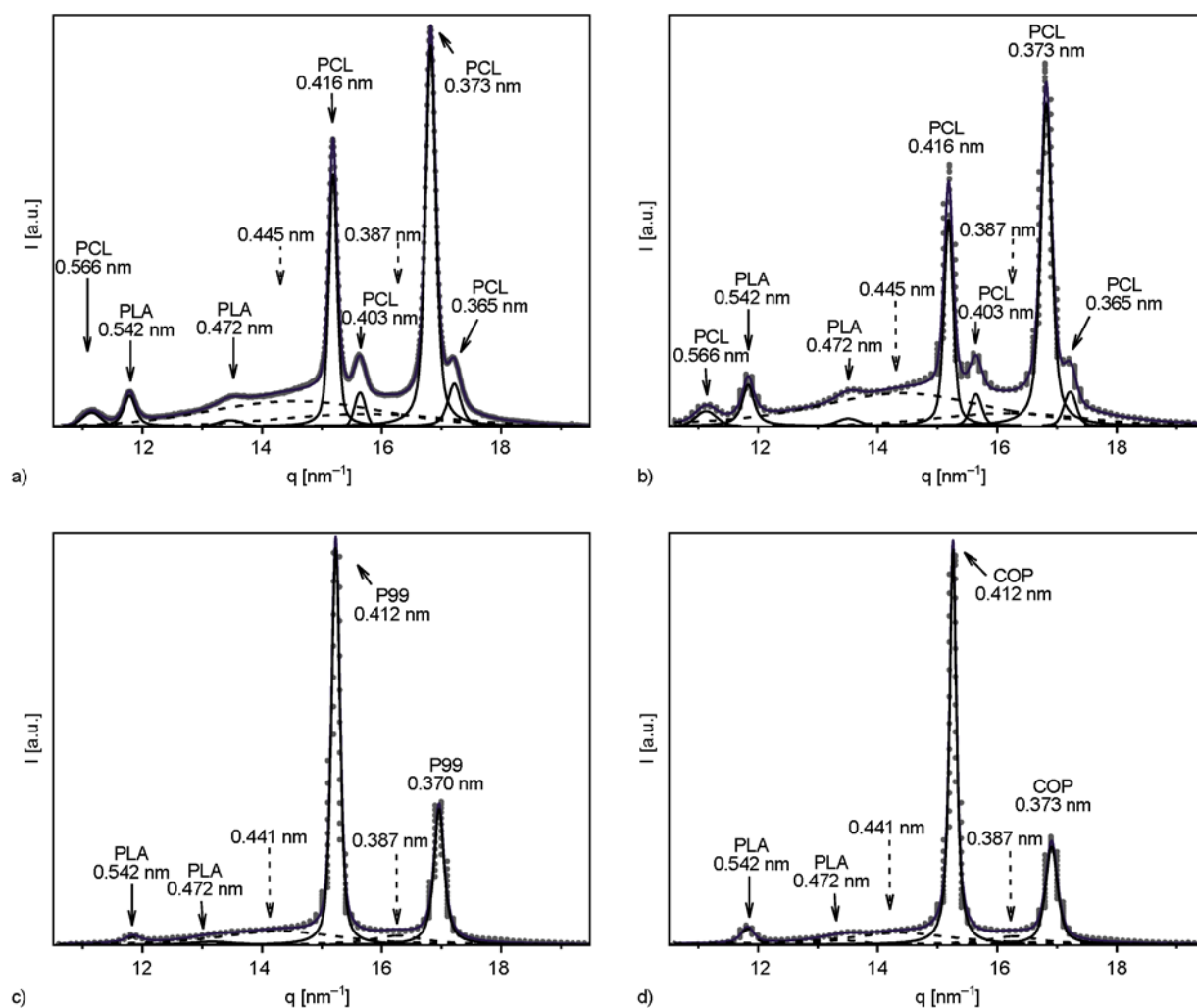


Figure 5. WAXD profiles corresponding to PCL (a, b), P99 (c) and COP (d) samples reinforced with PLA nanofibers (a, c, d) and PLA microfibers (b). Deconvoluted amorphous halos (dashed lines) and crystalline peaks (solid lines) are indicated, along with the corresponding simulated profiles (blue solid lines). Abscise axes correspond to the scattering vector ($q = 2\pi/d_B$, where d_B is the Bragg spacing).

ester, together with amorphous halos and the above peaks associated with cold crystallized PLA, were observed. Thus, PCL samples showed peaks at 0.566, 0.416, 0.403 and 0.373 nm, which correspond to the (102), (110), (111) and (200) reflections of polycaprolactone [25, 26] whereas both P99 and COP samples showed peaks at 0.412 and 0.373–0.370 nm, which are indicative of similar molecular packing arrangements. In all cases, the relative intensity of PLA reflections slightly increased when using nanofibers whereas the relative intensity of the polyester matrix reflections remained almost constant. The degree of crystallinity was rather similar for micro- and nanofiber assemblies since the polyester matrix was always predominant, although slight differences could be detected when only PLA reflections and amorphous halos were considered (Table 1).

The low molecular weight of P99 and COP samples gave rise to slightly higher crystallinities for assemblies based on these polyester matrices.

WAXD patterns of triclosan loaded samples did not show any peaks attributable to the drug and demonstrated that triclosan was well mixed in the PCL, P99, COP and PLA polyester matrices. Diffraction patterns of loaded and unloaded samples were rather similar although a slight decrease in the degree of crystallinity was logically detected in samples containing triclosan. It should be pointed out that PLA reflections could still be detected in all cases, indicating that the drug could not completely avoid the cold crystallization process. Table 1 summarizes the crystallinity data determined for all samples studied.

Table 1. Estimated crystallinities from X-ray diffraction data for the different studied samples

Sample ^a	Crystallinity 100. $I_{PLA}/(I_{PLA} + I_{am})^b$			
	0T ^c	3T ^c	0T ^c	3T ^c
PLA-N ^d	23	23 ^e	23	23
PLA-M ^d	18	17	18	17
PCL	49	–	–	–
PE99	69	–	–	–
COP	62	–	–	–
PCL/PLA-N/PCL	44	44 ^f	12	11 ^f
PCL/PLA-M/PCL	57	56 ^f	9	8 ^f
PE99/PLA-N/PE99	65	63 ^f	14	12 ^f
PE99/PLA-M/PE99	63	62 ^f	11	10 ^f
COP/PLA-N/COP	65	63 ^f	20	18 ^f
COP/PLA-M/COP	63	62 ^f	17	15 ^f

^aN and M indicate nanofibers and microfibers, respectively.

^bRatio between the intensity of PLA reflections and the total intensity once the crystalline reflections of the polyester matrix were discarded. Note that amorphous halos of the matrix are still considered.

^c0T and 3T denote samples containing triclosan weight percentages of 0 and 3%, respectively.

^dCold crystallized samples.

^eWithout considering diffraction peaks associated to triclosan.

^fTriclosan was only loaded into the PLA fibres and the percentage refers to the PLA content.

3.3. Mechanical properties of polyester matrices reinforced with PLA micro/nanofibers

Very few works address the development of electrospun fibers as reinforcing materials despite their high potential interest [8, 9, 27]. For example, it has been clearly demonstrated that addition of nylon 6 electrospun nanofibers to an epoxy resin enhances the stiffness and strength of the polymer matrix significantly. It has also been established that electrospun nanofibers should have advantages [28] over traditional fillers since the reinforcing effect of the former is mainly influenced by fiber size. Hence, the integrity of the polymer matrix should be enhanced by the use of fibers with nanometer dimensions instead of conventional fibers. Furthermore, the high porosity of electrospun fiber mats can result in an interpenetrating structure after their incorporation into the polymer matrix and an increase of the mechanical strength caused by the interlocking mechanism [9, 27]. Another advantage of smaller fiber diameters is that they should lead to higher tensile strengths since the fiber surface becomes dominant over the core region with bulk-like properties, and segmental motion is more constrained when dimensions approach the polymer radius of

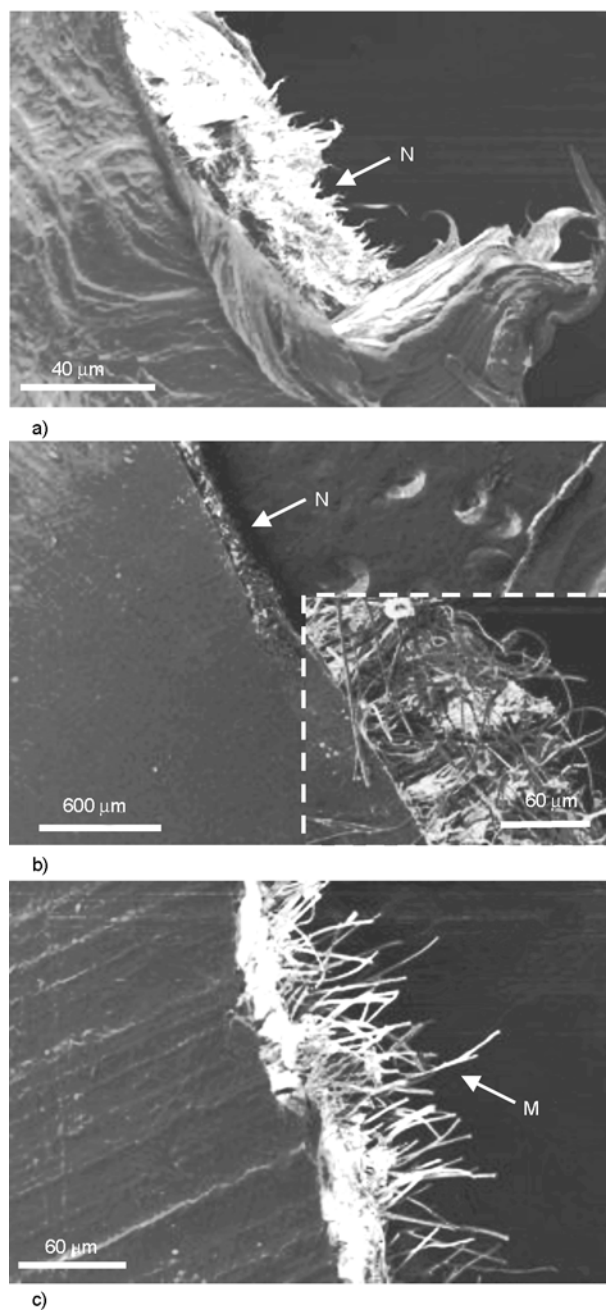


Figure 6. SEM micrographs showing the fracture surface of PCL reinforced with PLA nanofibers (a), P99 reinforced with PLA nanofibers (b) and COP reinforced with PLA microfibers (c). Arrows point to PLA nanofibers (N) and microfibers (M).

gyration [27, 29]. Finally, it must be pointed out that oriented and stretched polymer chains in electrospun samples lead to a decrease in the tensile deformation with respect to the bulk polymer [27, 30]. Representative fracture surfaces of samples after mechanical testing show micro/nanofiber pullout (Figure 6) as well as good dispersion of fibers inside the matrix. Note also that fibers appear aligned after breaking in the direction of the applied stress, a fea-

ture that contrasts with the structure of the inserted mats, which is characterized by a random orientation of long micro/nanofibers. Crack damage appears to start in the polyester matrix; then fibers are affected by the external force and pulled out and aligned before breaking. The strength of these fiber composites depends on the evolution of damage, which is a combination of matrix cracking, fiber fracture, fiber pullout, debonding and inelastic matrix deformation throughout the application of loading [31, 32].

Figure 7a compares the stress-strain curves obtained with the PCL matrix and PCL samples reinforced with PLA micro/nanofiber mats. Curves exhibited linear behavior at early stages of loading, which became non-linear before maximum load was reached. A drop in load followed as a result of failure initiation. Table 2 summarizes the main mechanical parameters determined for all samples studied before and after incorporation of PLA mats. Some conclusions can be drawn from these values: a) The incorporation of the reinforcing fibers clearly enhanced the stiffness of the material; consequently, the elastic modulus increased by 115 and 48% by adding the microfiber and nanofiber mats, respectively, b) The increase in the maximum tensile strength was greater when microfibers were employed (i.e. 21%), c) The unfilled PCL matrix showed a plastic deformation that led to a high strain at break which contrasted with the reduced values determined for filled samples. Figure 7 also shows that the elastic modulus and tensile strength of triclosan loaded samples decreased slightly and significantly, respectively, probably due to a slight decrease in the

PLA crystallinity (Table 1) and a more significant reduction of the surface interactions between the matrix and added fibers.

Figure 7b and Table 2 point out that properties were greatly improved by reinforcing low molecular weight polymers (i.e. P99 and COP) since these matrices had brittle fracture, low deformation at break and low tenacity. Hence, the enhancement of tensile strength became highly relevant when PLA mats were added. Note that the best results were obtained again by using fibers with micrometer diameter sizes (e.g. the modulus increased by 313 and 80% when COP was reinforced with microfiber and nanofiber mats, respectively).

In general, mechanical properties showed less improvement when nanofibers were used. This striking feature may be an inherent consequence of the fabric procedure where mats with randomly oriented fibers and different porosity were employed. Note that SEM micrographs of electrospun mats

Table 2. Mechanical properties of the different studied samples

Sample ^a	Young modulus [MPa]	Maximum stress [MPa]	Strain at break [%]
PCL	19±2	18±2	1400±80
PCL/PLA-M/PCL	41±3	22±2	150±10
PCL/PLA-N/PCL	28±2	19±2	170±10
PE99	11±1	2±0.5	17±2
PE99/PLA-M/PE99	60±4	7±1	10±2
PE99/PLA-N/PE99	22±2	5±1	18±3
COP	15±1	7±1	68±6
COP/PLA-M/COP	62±3	11±1	17±3
COP/PLA-N/COP	27±2	8±1	33±3

^aN and M indicate nanofibers and microfibers, respectively.

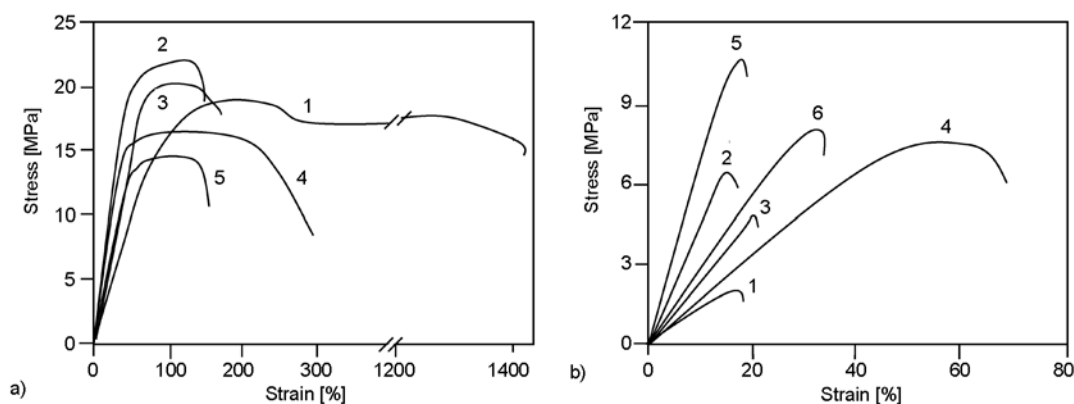


Figure 7. a) Stress-strain curves of PCL without reinforcing PLA fibers (1), with PLA microfibers (2, 4) and with PLA nanofibers (3, 5). Fibers were unloaded (2, 3) or loaded with 3 wt% of TCS (4, 5). b) Stress-strain curves of P99 (1, 2, 3) and COP (4, 5, 6) samples without reinforcing PLA fibers (1, 4), with PLA microfibers (2, 5) and with PLA nanofibers (3, 6).

showed a higher spacing between microfibers than between nanofibers (i.e. 5 μm versus ca. 1 μm as shown in Figures 2a and 2c). Thus, nanofibers gave rise to a highly compact and scarcely porous three-dimensional arrangement that made it difficult to achieve optimal surface interactions with the melted polyester matrix by the subsequent molding process.

3.4. Triclosan release from mats of PLA micro/nanofibers and polyester matrices filled with PLA micro/nanofibers

The release rates can be calculated from experimental results by considering several theoretical models, typically first-order [33, 34], Higuchi [35, 36] and their combination [37]. The release from mat samples constituted by fibers and even from film samples usually occurred in two different steps, i.e. rapid release of molecules that should be deposited on the surface area and slow release that should involve the diffusion of molecules through the polymer matrix towards the release medium. Thus, the Higuchi (Equation (1)) and first-order (Equation (2)) models were usually combined to describe the first (0–60%) and second (40–100%) parts of the release, respectively:

$$\frac{M_t}{M_0} = k_h t^{1/2} \quad \left(0 \leq \frac{M_t}{M_0} \leq 0.6 \right) \quad (1)$$

$$\ln\left(1 - \frac{M_t}{M_0}\right) = a - k_1 t \quad \left(0 \leq \frac{M_t}{M_0} \leq 1.0 \right) \quad (2)$$

where k_h is the Higuchi release constant, k_1 is the first-order release constant, a takes into account the release in the first step, M_t is the percentage of drug released at time t , and M_0 is the triclosan equilibrium percentage (considered as the maximum triclosan percentage that can be delivered in the medium). The assumption of the late-time Equation (2) implies that the amount of drug released at each time is proportional to the residual drug inside the dosage form.

Triclosan release in Sørensen medium [38] is characterized by the achievement of an equilibrium condition where the affinity between drug and polymer matrix plays a substantial role. This equilibrium can be modified by increasing the hydrophobicity of the release medium, which is easily achieved by adding ethanol. A volume percentage of 70% had been previously found to give similar release results to more

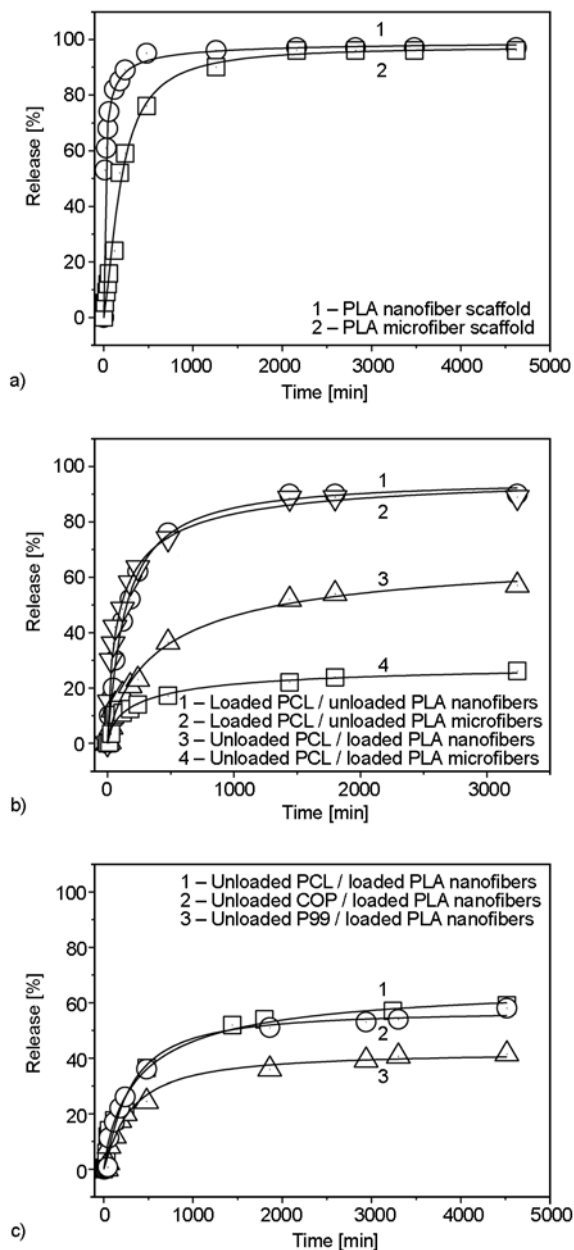


Figure 8. Comparison between cumulative triclosan release in a Sørensen/ethanol (30/70 v/v) medium from PLA scaffolds (a, curves: 1, PLA nanofiber; 2, PLA microfiber), differently loaded PCL samples (b, curves: 1, loaded PCL / unloaded PLA nanofibers; 2, loaded PCL / unloaded PLA microfibers; 3, unloaded PCL / loaded PLA nanofibers; 4, unloaded PCL / loaded PLA microfibers), and different polyester matrices filled with PLA microfiber mats (c, curves: 1, unloaded PCL / loaded PLA nanofibers; 2, unloaded COP / loaded PLA nanofibers; 3, unloaded P99 / loaded PLA nanofibers).

expensive serum-based media [38]. It should also be pointed out that ethanol may have some swelling effect that could facilitate the drug release.

The cumulative triclosan release from PLA scaffolds constituted by electrospun fibers with micrometer or nanometer diameter sizes is compared in Figure 8a. Release profiles are significantly different and indicate a logically higher rate when fibers had smaller diameter sizes since the drug should be closer to the fiber surface, decreasing the drug diffusion path length. Furthermore, a significant Burst effect was observed, in agreement with the existence of triclosan crystalline domains probably located on the fiber surface, as revealed by WAXD data. Table 3 compares the release constants for the two samples when the combined model was used. It is clear that both k_h and k_1 release constants decreased drastically for the electrospun microfibers. It should be noted that, in this case, k_1 became close to the value previously determined for similar PLA scaffolds (i.e. 0.09 and 0.08 min⁻¹) [24]. Release data also indicate that all the triclosan was practically released in the selected medium and only an increase in the time required for complete delivery was observed when the diameter was increased (i.e. 700 and 1600 min for the nanofibers and microfibers with average diameters of 2.56 and 0.350 μm). An asymptotic release percentage was clearly detected when PCL fabric samples were employed (Figure 8b), suggesting that equilibrium conditions were achieved when the medium was not renewed or that some molecules were entrapped in the dosage form. No remaining percentage was observed for PLA scaffolds but it should be taken into account that release behaviors could not be strictly compared due to the different texture (i.e. compact or

porous) and geometry of samples. However, it should be reminded that previous results on similar PCL scaffold samples [24] showed greater affinity of triclosan with the more hydrophobic PCL polymer and a lower final release percentage when PLA scaffolds were progressively enriched with PCL. As can be seen in Table 3 and Figure 8b, very few differences were found when triclosan loaded PCL matrices were reinforced with PLA micro/nanofibers. Nevertheless, the kinetic constant values (Table 3) indicate that the initial and faster release step was slightly disfavored by addition of nanofibers, suggesting greater difficulty for triclosan molecules to diffuse through the nanofilled polymer matrix.

Release behavior changed drastically when the drug was only loaded into the reinforcing PLA micro/nanofibers, as shown in Figure 8b. First, a small time period (t_0 values summarized in Table 3) seemed to be required for the start of the release. Consequently, the experimental data can only be fitted to a Higuchi behavior after the observed ‘induction’ time. Apparently, drug molecules need a significant time period to reach the surface of the polymer matrix from the filled fibers. Second, the release initially progressed at a moderate rate (note that k_h was always significantly lower than the values calculated for samples with the drug directly loaded into the polymer matrix). Third, the release rate also decreased during the second step defined by a first-order kinetics. It is important to point out that the release tended to an asymptotic value which was clearly lower than that found for samples with the

Table 3. Correlation coefficients and release rate constant for the fitting to the combined model of release profiles corresponding to the indicated samples loaded with 3 wt% of triclosan and delivered in a Sørensen/ethanol medium (30/70 v/v)

Sample	Early-Time		Late-Time		t_0^a [min]	t_f^b [min]
	k_h [h ^{-0.5}]	r	k_1 [h ⁻¹]	r		
PLA Nano ^c	0.957	0.957	0.378	0.991	0	700
PLA Micro ^c	0.160	0.977	0.090	0.994	0	1600
PCL + PLA Nano ^d	0.320	0.981	0.198	0.996	0	2500
PCL + PLA Micro ^d	0.379	0.976	0.084	0.986	0	2500
PCL + PLA Nano ^e	0.159	0.998	0.072	0.996	15	5000
PCL + PLA Micro ^e	0.139	0.980	0.060	0.993	30	6000
COP + PLA Nano ^e	0.265	0.999	0.036	0.990	45	6300
P99 + PLA Nano ^e	0.215	0.970	0.036	0.995	45	6300

^aTime necessary to initiate the Higuchi release.

^bTime necessary to reach a constant release.

^cScaffold samples.

^dTriclosan was only loaded in the PCL matrix.

^eTriclosan was only loaded in the PLA electrospun fibers.

drug directly loaded into the matrix and that the final release percentage was lower when the drug was loaded into PLA microfibers instead of PLA nanofibers. This large difference between the three loaded samples cannot be justified by the achievement of equilibrium conditions since practically the same value should be deduced. Results suggest that triclosan was entrapped in the PLA fibers and could not effectively diffuse through the PCL matrix at an appreciable rate. The amount of retained triclosan logically increased with the fiber diameter. As a result, a lower cumulative release percentage was found for samples containing microfibers. The initial fast release step may be a consequence of the preparation method since at the molding temperature some diffusion from PLA nano/microfibers to the melted PCL matrix could have occurred, and then (i.e. at room temperature) diffusion was clearly hindered.

Table 4. Contact angle (Θ) for the polyester films (PCL, P99, COP) and polyester matrices reinforced with mats of PLA microfibers (M) and nanofibers (N).

Sample	Θ [$^\circ$] ^a
PCL	81.4±2.5
PCL/PLA-M/PCL	77.3±5.3
PCL/PLA-N/PCL	66.2 ±4.9 ^b
P99	90.5±6.2 ^c
P99/PLA-M/P99	80.5±1.9 ^b
P99/PLA-N/P99	79.4±3.4 ^b
COP	87.7±6.0 ^c
COP/PLA-M/COP	78.8±3.9 ^b
COP/PLA-N/COP	74.4±0.8 ^b

^aAverage values and standard deviation over six measurements.

^bTukey test, $p < 0.05$, composite vs. polymer film.

^cTukey test, $p < 0.05$, reference film (PCL) vs. polymer film.

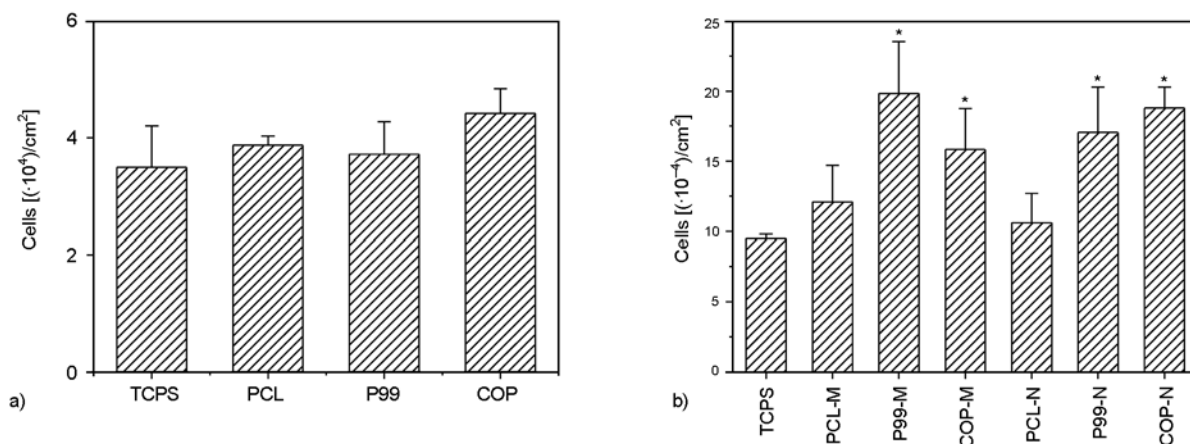


Figure 9. a) Attachment of HEp-2 cells to the surface of PCL, P99 and COP samples. b) Cell proliferation on TCPS and the above polyesters loaded with PLA microfibers (M) or PLA nanofibers (N) after 7 days of culture. The vertical bars are the average values \pm SD. (*) $p < 0.05$ vs control sample (TCPS or surface plate), t -Student test.

Figure 8c shows that release behavior depended on the hydrophobicity of the polymer matrix, which could be evaluated by the contact angle measurements summarized in Table 4. Hence, the release rate constants (Table 3) and even the asymptotic release value decreased with hydrophobicity, which depended on the methylene content of the repeat unit and increased in the order P99 > COP > PCL. Samples containing triclosan loaded micro/nanofibers appear highly interesting since a relatively fast release is observed at the beginning of the delivery process; hence, a rapid antimicrobial effect should be expected; as found from the release of the similar systems [24, 38]. Furthermore, a considerable amount of drug could be retained, and therefore pharmacological activity may be observed again when degradation of the polymer matrix reaches a considerable level. Furthermore, the amount of retained drug can be tuned by varying the fiber diameter size and the hydrophobic character of the polymer matrix.

3.5. Biocompatibility of polyester matrices reinforced with PLA micro/nanofibers

The adhesion assay was carried out on the film surfaces of the processed materials to evaluate the quality of the new polyesters (P99 and COP) as substrates for cell attachment. These polymers showed slightly improved adhesion in comparison to TCPS or PCL (used as a reference). The increase was more evident for COP, although the number of cells adhered to the studied surfaces was not statistically different (Figure 9a). Figure 10 qualitatively compares the aspect of the cells adhered to the selected

polyester surfaces. Cells spread extensively on the PCL and COP surfaces (Figures 10a–b and 10e–f, respectively) whereas very little spreading was detected on the P99 surface where cells clearly had a more rounded morphology (Figure 10c–d). This morphology-based approach suggests again that the COP surface supports cell adhesion better. Cell proliferation assays were conducted to evaluate the three reinforced polyester matrices, which were characterized by a three-dimensional array

that may be a first approximation to more conventional scaffolds. Figure 9b shows the results of the HEp-2 cell culture for 7 days on all materials studied. The number of cells in the PCL matrix reinforced with mats constituted by PLA micro/nanofibers (PCL-M and PCL-N, respectively) suggested a similar growth to that observed for the control (TCPS). However, cell growth in reinforced P99 and COP matrices was significantly higher than in the control ($p < 0.05$) and in PCL samples, although

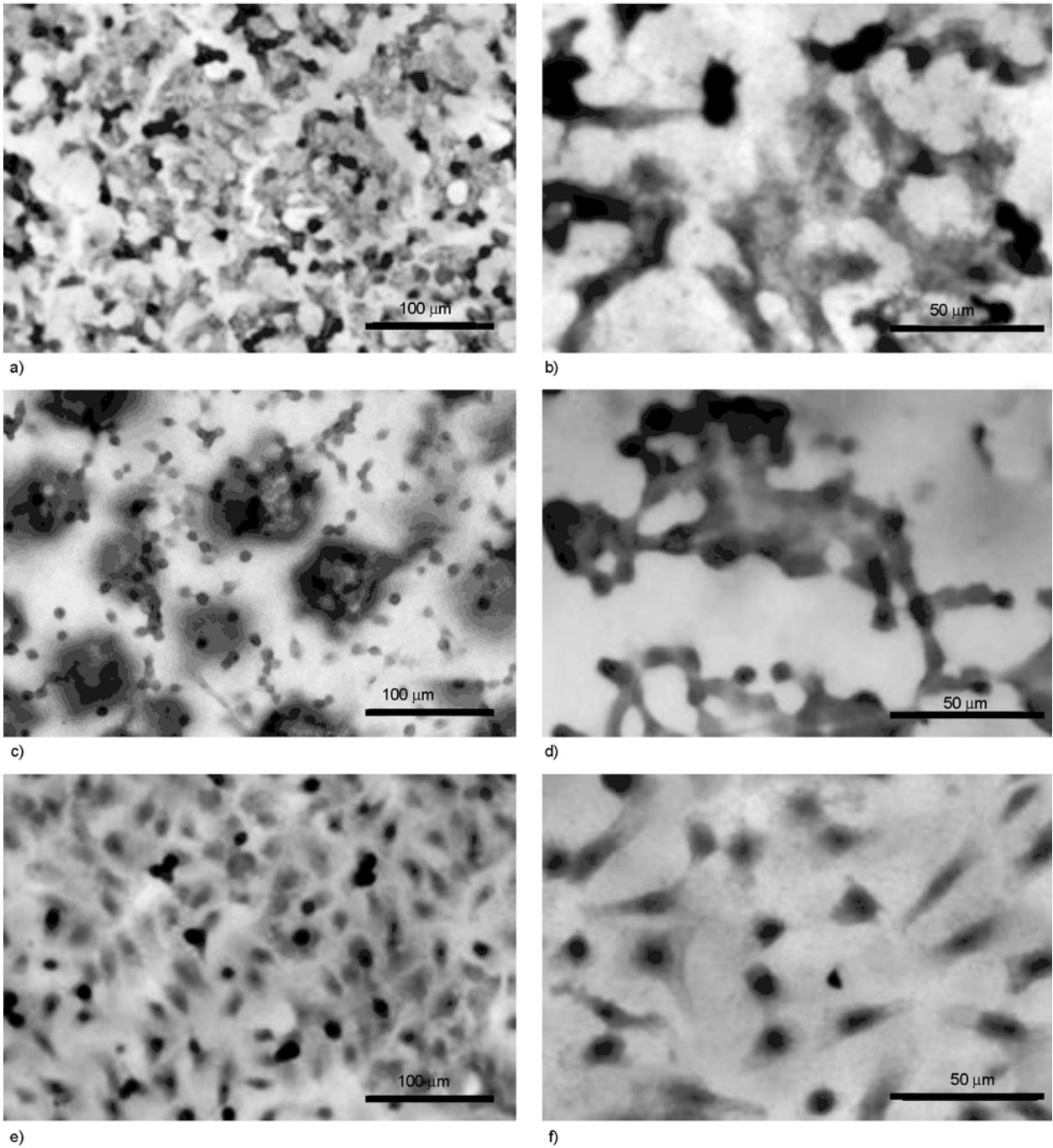


Figure 10. Optical micrographs showing the morphology of HEp-2 cells adhered to PCL (a, b), P99 (c, d) and COP (e, f) substrates

in this case the difference did not reach a significant statistical value. These results can be justified considering that all polyester samples corresponded to three-dimensional architectures while the TCPS control corresponded to a cell growth in a two-dimensional system, and consequently with a smaller available surface. It should also be highlighted that no significant differences were detected by using reinforcing mats constituted by PLA micro/nanofibers. Note that all surfaces studied had a similar number of cells in the initial event of adhesion. Differences in their colonization can therefore be directly related to the structure and properties of materials. The present study indicates that all polyester fabrics evaluated appear highly biocompatible because they supported cell growth well.

4. Conclusions

Mats constituted by PLA micro/nanofibers can be easily prepared by changing only the polymer concentration of the solution used in the electrospinning process. These fibers showed a high molecular orientation that was more significant with smaller fiber diameter sizes and favored the cold crystallization process.

Fabrics constituted by PLA mats inserted in polyesters with lower melting points had high crystallinity when prepared by a molding and slow cooling process that allowed both PLA cold crystallization and hot crystallization of the polyester matrix. These fabrics showed also a significant enhancement of both elastic modulus and tensile strength respect to the corresponding polyester matrices. Materials were biocompatible and were successful to provide a sustained drug release when the pharmacological agent was directly loaded into the reinforcing PLA mat. Applications concerning an enlargement of antimicrobial effect (e.g. by incorporation of triclosan) can be considered.

Acknowledgements

This research has been supported by grants from MCYT/FEDER and AGAUR (MAT2009-11503, 2009SGR-1208). We are grateful to Drs. François Fauth and Ana Labrador of the CRG BM16 beamline staff of CELLS (Consortium for the Exploitation of the Synchrotron Light Laboratory). We are also grateful to Dr. Trifon Trifonov for FIB micrographs.

References

- [1] Boudriot U., Dersch R., Greiner A., Wendorff J. H.: Electrospinning approaches toward scaffold engineering – A brief overview. *Artificial Organs*, **30**, 785–792 (2006).
DOI: [10.1111/j.1525-1594.2006.00301.x](https://doi.org/10.1111/j.1525-1594.2006.00301.x)
- [2] Katti D. S., Robinson K. W., Ko F. K., Laurencin C. T.: Bioresorbable nanofiber-based systems for wound healing and drug delivery: Optimization of fabrication parameters. *Journal of Biomedical Materials Research Part B: Applied Biomaterials*, **70**, 286–296 (2004).
DOI: [10.1002/jbm.b.30041](https://doi.org/10.1002/jbm.b.30041)
- [3] Li S., Patel S., Hashi C., Huang N. F., Kurpinski K.: Biomimetic scaffolds. U.S. Patent 20070269481, USA (2007).
- [4] Reneker D. H., Yarin A. L., Fong H., Koombhongse S.: Bending instability of electrically charged liquid jets of polymer solutions in electrospinning. *Journal of Applied Physics*, **87**, 4531–4547 (2000).
DOI: [10.1063/1.373532](https://doi.org/10.1063/1.373532)
- [5] Yarin A. L., Koombhongse S., Reneker D. H.: Bending instability in electrospinning of nanofibers. *Journal of Applied Physics*, **89**, 3018–3027 (2001).
DOI: [10.1063/1.1333035](https://doi.org/10.1063/1.1333035)
- [6] Dror Y., Salalha W., Khalfin R. L., Cohen Y., Yarin A. L., Zussman E.: Carbon nanotubes embedded in oriented polymer nanofibers by electrospinning. *Langmuir*, **19**, 7012–7020 (2003).
DOI: [10.1021/la034234i](https://doi.org/10.1021/la034234i)
- [7] Stephens J. S., Chase D. B., Rabolt J. F.: Effect of the electrospinning process on polymer crystallization chain conformation in nylon-6 and nylon-12. *Macromolecules*, **37**, 877–881 (2004).
DOI: [10.1021/ma0351569](https://doi.org/10.1021/ma0351569)
- [8] Bergshoeff M. M., Vancso G. J.: Transparent nanocomposites with ultrathin, electrospun nylon-4,6 fiber reinforcement. *Advanced Materials*, **11**, 1362–1365 (1999).
DOI: [10.1002/\(SICI\)1521-4095\(199911\)11:16<1362::AID-ADMA1362>3.0.CO;2-X](https://doi.org/10.1002/(SICI)1521-4095(199911)11:16<1362::AID-ADMA1362>3.0.CO;2-X)
- [9] Fong H.: Electrospun nylon 6 nanofiber reinforced BIS-GMA/TEGDMA dental restorative composite resins. *Polymer*, **45**, 2427–2432 (2004).
DOI: [10.1016/j.polymer.2004.01.067](https://doi.org/10.1016/j.polymer.2004.01.067)
- [10] Pinho E. D., Martins A., Araújo J. V., Reis R. L., Neves N. M.: Degradable particulate composite reinforced with nanofibres for biomedical applications. *Acta Biomaterialia*, **5**, 1104–1114 (2009).
DOI: [10.1016/j.actbio.2008.11.018](https://doi.org/10.1016/j.actbio.2008.11.018)
- [11] Grafahrend D., Heffels K-H., Beer M. V., Gasteier P., Möller M., Boehm G., Dalton P. D., Groll J.: Degradable polyester scaffolds with controlled surface chemistry combining minimal protein adsorption with specific bioactivation. *Nature Materials*, **10**, 67–73 (2011).
DOI: [10.1038/NMAT2904](https://doi.org/10.1038/NMAT2904)

- [12] Jones R. D., Jampani H. B., Newman J. L., Lee A. S.: Triclosan: A review of effectiveness and safety in health care settings. *American Journal of Infection Control*, **28**, 184–196 (2000).
DOI: [10.1016/S0196-6553\(00\)90027-0](https://doi.org/10.1016/S0196-6553(00)90027-0)
- [13] Södergård A., Stolt M.: Properties of lactic acid based polymers and their correlation with composition. *Progress in Polymer Science*, **27**, 1123–1163 (2002).
DOI: [10.1016/S0079-6700\(02\)00012-6](https://doi.org/10.1016/S0079-6700(02)00012-6)
- [14] Middleton J. C., Tipton A. J.: Synthetic biodegradable polymers as orthopedic devices. *Biomaterials*, **21**, 2335–2346 (2000).
DOI: [10.1016/S0142-9612\(00\)00101-0](https://doi.org/10.1016/S0142-9612(00)00101-0)
- [15] Pouget E., Almontassir A., Casas M. T., Puiggali J.: On the crystalline structures of poly(tetramethylene adipate). *Macromolecules*, **36**, 698–705 (2003).
DOI: [10.1021/ma0214052](https://doi.org/10.1021/ma0214052)
- [16] Almontassir A., Gestí S., Franco L., Puiggali J.: Molecular packing of polyesters derived from 1,4-butanediol and even aliphatic dicarboxylic acids. *Macromolecules*, **37**, 5300–5309 (2004).
DOI: [10.1021/ma0499391](https://doi.org/10.1021/ma0499391)
- [17] Gestí S., Casas M. T., Puiggali J.: Single crystal morphology and structural data of a series of polyesters derived from 1,8-octanediol. *European Polymer Journal*, **44**, 2295–2307 (2008).
DOI: [10.1016/j.eurpolymj.2008.04.049](https://doi.org/10.1016/j.eurpolymj.2008.04.049)
- [18] Lim C. T., Tan E. P. S., Ng S. Y.: Effects of crystalline morphology on the tensile properties of electrospun polymer nanofibers. *Applied Physics Letters*, **92**, 141908/1–141908/3 (2008).
DOI: [10.1063/1.2857478](https://doi.org/10.1063/1.2857478)
- [19] Hurrell S., Cameron R. E.: The effect of initial polymer morphology on the degradation and drug release from polyglycolide. *Biomaterials*, **23**, 2401–2409 (2002).
DOI: [10.1016/S0142-9612\(01\)00376-3](https://doi.org/10.1016/S0142-9612(01)00376-3)
- [20] Miyajima M., Koshika A., Okada J., Ikeda M., Nishimura K.: Effect of polymer crystallinity on papaverine release from poly(L-lactic acid) matrix. *Journal of Controlled Release*, **49**, 207–215 (1997).
DOI: [10.1016/S0168-3659\(97\)00081-3](https://doi.org/10.1016/S0168-3659(97)00081-3)
- [21] de Santis P., Kovacs A. J.: Molecular conformation of poly(S-lactic acid). *Biopolymers*, **6**, 299–306 (1968).
DOI: [10.1002/bip.1968.360060305](https://doi.org/10.1002/bip.1968.360060305)
- [22] Hoogsteen W., Postema A. R., Pennings A. J., Ten Brinke G., Zugenmaier P.: Crystal structure, conformation and morphology of solution-spun poly(L-lactide) fibers. *Macromolecules*, **23**, 634–642 (1990).
DOI: [10.1021/ma00204a041](https://doi.org/10.1021/ma00204a041)
- [23] Zeng J., Chen X., Liang Q., Xu X., Jing X.: Enzymatic degradation of poly(L-lactide) and poly(ϵ -caprolactone) electrospun fibers. *Macromolecular Bioscience*, **4**, 1118–1125 (2004).
DOI: [10.1002/mabi.200400092](https://doi.org/10.1002/mabi.200400092)
- [24] del Valle L. J., Camps R., Díaz A., Franco L., Rodríguez-Galán A., Puiggali J.: Electrospinning of polylactide and polycaprolactone mixtures for preparation of materials with tunable drug release properties. *Journal of Polymer Research*, **18**, 1903–1917 (2011).
DOI: [10.1007/s10965-011-9597-3](https://doi.org/10.1007/s10965-011-9597-3)
- [25] Chatani Y., Okita Y., Tadokoro H., Yamashita Y.: Structural studies of polyesters. 3. Crystal structure of poly-epsilon-caprolactone. *Polymer Journal*, **1**, 555–562 (1970).
- [26] Iwata T., Doi Y.: Morphology and enzymatic degradation of poly(ϵ -caprolactone) single crystals: Does a polymer single crystal consist of micro-crystals? *Polymer International*, **51**, 852–858 (2002).
DOI: [10.1002/pi.858](https://doi.org/10.1002/pi.858)
- [27] Baji A., Mai Y-W., Wong S-C., Abtahi M., Chen P.: Electrospinning of polymer nanofibers: Effects on oriented morphology, structures and tensile properties. *Composites Science and Technology*, **70**, 703–718 (2010).
DOI: [10.1016/j.compscitech.2010.01.010](https://doi.org/10.1016/j.compscitech.2010.01.010)
- [28] Tian M., Gao Y., Liu Y., Liao Y., Xu R., Hedin N. E., Fong H.: Bis-GMA/TEGDMA dental composites reinforced with electrospun nylon 6 nanocomposite nanofibers containing highly aligned fibrillar silicate single crystals. *Polymer*, **48**, 2720–2728 (2007).
DOI: [10.1016/j.polymer.2007.03.032](https://doi.org/10.1016/j.polymer.2007.03.032)
- [29] Arinstein A., Burman M., Gendelman O., Zussman E.: Effect of supramolecular structure on polymer nanofibre elasticity. *Nature Nanotechnology*, **2**, 59–62 (2007).
DOI: [10.1038/nnano.2006.172](https://doi.org/10.1038/nnano.2006.172)
- [30] Lu J-W., Zhang Z-P., Ren X-Z., Chen Y-Z., Yu J., Guo Z-X.: High-elongation fiber mats by electrospinning of polyoxymethylene. *Macromolecules*, **41**, 3762–3764 (2008).
DOI: [10.1021/ma702881k](https://doi.org/10.1021/ma702881k)
- [31] Kroll L., Hufenbach W.: A physically based failure criterion for laminated composites. *Mechanics of Composite Materials*, **35**, 277–284 (1999).
DOI: [10.1007/BF02259715](https://doi.org/10.1007/BF02259715)
- [32] Brauer D. S., Rüssel C., Vogt S., Weisser J., Schnabelrauch M.: Degradable phosphate glass fiber reinforced polymer matrices: Mechanical properties and cell response. *Journal of Materials Science: Materials in Medicine*, **19**, 121–127 (2008).
DOI: [10.1007/s10856-007-3147-x](https://doi.org/10.1007/s10856-007-3147-x)
- [33] Gibaldi M., Feldman S.: Establishment of sink conditions in dissolution rate determinations. Theoretical considerations and application to nondisintegrating dosage forms. *Journal of Pharmaceutical Sciences*, **56**, 1238–1242 (1967).
DOI: [10.1002/jps.2600561005](https://doi.org/10.1002/jps.2600561005)
- [34] Wagner J. G.: Interpretation of percent dissolved-time plots derived from *in vitro* testing of conventional tablets and capsules. *Journal of Pharmaceutical Sciences*, **58**, 1253–1257 (1969).
DOI: [10.1002/jps.2600581021](https://doi.org/10.1002/jps.2600581021)

- [35] Higuchi T.: Rate of release of medicaments from ointment bases containing drugs in suspension. *Journal of Pharmaceutical Sciences*, **50**, 874–879 (1961).
DOI: [10.1002/jps.2600501018](https://doi.org/10.1002/jps.2600501018)
- [36] Higuchi T.: Mechanism of sustained-action medication. Theoretical analysis of rate of release of solid drugs dispersed in solid matrices. *Journal of Pharmaceutical Sciences*, **52**, 1145–1149 (1963).
DOI: [10.1002/jps.2600521210](https://doi.org/10.1002/jps.2600521210)
- [37] Baker R. W.: *Controlled release of biologically active agents*. Wiley, New York (1987).
- [38] Zurita R., Puiggali J., Rodríguez-Galán A.: Triclosan release from coated polyglycolide threads. *Macromolecular Bioscience*, **6**, 58–69 (2006).
DOI: [10.1002/mabi.200500147](https://doi.org/10.1002/mabi.200500147)

Functionalized graphene – poly(vinyl alcohol) nanocomposites: Physical and dielectric properties

I. Tantis, G. C. Psarras*, D. Tasis

Department of Materials Science, School of Natural Sciences, University of Patras, Patras 26504, Hellas (Greece)

Received 29 July 2011; accepted in revised form 19 October 2011

Abstract. Chemically derivatized graphene/poly(vinyl alcohol) (PVA) nanocomposites were successfully fabricated by combination of solution processing and compression molding. SEM imaging combined with XRD measurements revealed that graphene platelets were fully incorporated into the polymer matrix after their chemical modification through adsorption of amphiphilic copolymer. The chemical functionalities onto the graphitic surface prevented particle aggregation and provided compatibility with the polymer matrix. Thermogravimetric analysis demonstrated enhanced thermal stability for the composites containing modified graphenes at loading above 1 wt%. Differential scanning calorimetry thermograms showed that graphene nanoplatelets induced the crystallization of matrix with optimum loading at 2 wt%. Dielectric spectroscopy measurements showed enhanced electrical permittivity for the graphene oxide/PVA system, compared to the one of graphene/copolymer/PVA. This could be attributed to the formation of an insulating coating between graphite inclusions and PVA because of the presence of the copolymer.

Keywords: polymer composites, nanocomposites, graphene, dielectric properties, thermal stability

1. Introduction

Polymer composites, filled by graphitic nanostructures, have attracted increased attention owing to their unique mechanical, electric and optical properties [1–3]. Nano-sized conductive fillers, including graphene nanoplatelets, can create a percolative network within the polymer matrix at a low weight fraction, while the presence of conductive nanoinclusions within a polymer matrix could alter the permittivity of the composite systems resulting in enhancement of their energy storing capability [4]. Nanoinclusions can be considered as a distributed network of nanocapacitors, which can be charged and discharged defining an energy storing process, at the nanoscale level [5]. Graphene platelets, prepared via natural graphite exfoliation, have been widely used as a conducting filler in the fabrication of conductive polymer composites [6–9]. Graphite

has a layered crystal structure, in which the carbon atoms are strongly bonded on a two-dimensional network consisting of hexagons. Because the layers are bound by weak van der Waals forces, the idea of separating the bulk graphite into platelets consisting of few carbon layers having nanometer-scale thickness, or even into a single layer, has long been considered as the goal for obtaining super-strong and conductive polymer composites. Different types of graphite nanoplatelets, such as thermally expanded graphite [10, 11], graphene oxide (GO) [12, 13] and chemically modified graphene [14–17], have been used to make functional polymer composites. Chemical functionalization of graphene surface by either oxidation procedure or physical adsorption/grafting protocols have been found to be a feasible and effective means for improving the dispersion of graphenes in organic and/or aqueous media. In addi-

*Corresponding author, e-mail: G.C.Psarras@upatras.gr
© BME-PT

tion, the attached functional groups may enhance the interfacial interactions between the graphenes and the polymer matrix. The advantage of modifying the graphene surface by physical adsorption is that the structural integrity of the conjugated network remains unaltered, whereas formation of defects is observed after treatment of the graphitic nanostructures by oxidative conditions and/or grafting reactions.

To the best of our knowledge, there is no report on fabricating graphene/polymer composites by using noncovalently modified pristine graphene nanoplatelets. In addition, dielectric data such as dielectric permittivity, ac conductivity, and electric modulus have not been widely studied in graphene/polymer composites. We show here a simple and environmentally friendly preparation of graphene/PVA nanocomposites by incorporating amphiphilic block copolymer-modified graphenes into a PVA matrix using water as the compounding solvent. PVA is one of the most important commodity polymers due to its good mechanical and thermal properties. Its semicrystalline nature allows us to circumvent complexities of interpreting property changes associated with crystallization versus graphite addition. Here, we report a comparative study of PVA nanocomposites based on noncovalently modified graphene sheets, GO, and pristine graphite. The effect of graphene content on the physical and dielectric properties of PVA/graphene nanocomposites is investigated. The effect of filler's chemical functionalities as well as loading on various dielectric data (dielectric permittivity, ac conductivity, and electric modulus) was studied in detail.

2. Experimental section

2.1. Materials

Graphite with an average particle size of 45 μm and a purity of >95% was supplied from TIMCAL Ltd. (batch TIMREX KS44). Concentrated H_2SO_4 , $\text{K}_2\text{S}_2\text{O}_8$, P_2O_5 and PVA with $M_w \approx 145\,000$ were purchased from Sigma-Aldrich. The materials were directly used without further purification. The block

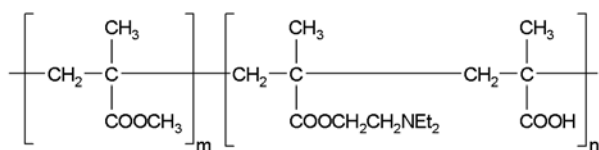


Figure 1. Chemical structure of the amphiphilic block copolymer

copolymer, the chemical structure of which is shown in Figure 1, was synthesized by hydrolysis of the t-butylmethacrylate units of the precursor sample. The latter was kindly supplied by Prof. C. Tsitsilianis (Univ. of Patras).

2.2. Preparation of graphene oxide

GO was synthesized from graphite powder by a previously reported method [18]. The graphite powder (15 g) was put into an 80°C solution of concentrated H_2SO_4 (60 mL), $\text{K}_2\text{S}_2\text{O}_8$ (7.8 g), and P_2O_5 (8.4 g). After reaching the temperature, the mixture was left to cool down to room temperature over a period of 6 h. The mixture was then carefully diluted with 300 mL of distilled water, filtered through 0.2 μm PTFE membrane (Millipore), and washed on the filter until the pH of the rinsing water became neutral. The product was dried in vacuum at 55°C for 48 hours.

2.3. Preparation of graphene/PVA composites

The synthesis procedure for a typical well-dispersed graphene/PVA nanocomposite (1.0 wt%) was as follows: Graphite powder (33 mg) was dispersed in distilled water (15 mL) in an ultrasonic bath (Branson 2510) for 60 min at room temperature. Subsequently, an aqueous solution (10 mL) of the amphiphilic copolymer (10 mg) was added to the graphite suspension. Sonication was continued for an extra 60 min to yield a stable black-colored suspension. Meanwhile, PVA (~3.25 g) was dissolved in distilled water (100 mL) at 90°C and the solution was subsequently cooled to room temperature. After the PVA/ H_2O solution had cooled to around 50°C, the graphene/copolymer aqueous dispersion was gradually added to the PVA solution and sonicated for an additional 30 min at room temperature. Finally, this homogeneous graphene/copolymer/PVA solution was poured into a Teflon Petri dish and kept at 60°C for film formation until its weight equilibrated. This film was peeled from of the substrate and was hot pressed at 200°C in order to eliminate the remaining air voids. A series of graphene/copolymer/PVA nanocomposite films with different loadings of graphene nanoplatelets (1, 2, 3 and 5 wt%) were similarly prepared. In all the aforementioned samples, the ratio between graphene and copolymer was kept constant and was approximately 3:1. For comparison, GO/PVA composite films were pre-

pared by the same protocol with loadings 1, 2, 3 and 5 wt%, respectively, as well as one sample of pristine graphite/PVA film (1 wt%). As a reference sample, neat PVA film was prepared by the hot casting technique.

2.4. Characterization

Fourier transform infrared spectra (FTIR) of graphite material were obtained on a EXCALIBUR FTS-300 (Digilab) spectrometer by the KBr pellet method. The thermal transitions of the samples were investigated by Differential Scanning Calorimetry (DSC) using a DSC Q200 (TA instruments). The experiments were carried out in nitrogen atmosphere using about 7 mg sample sealed in aluminium pans. The samples were heated from room temperature to 250°C. The heating rate was 10°C/min in all cases. Thermogravimetric analysis (TGA) was performed on a TGA Q500 (TA instruments) at a heating rate of 10°C/min in a nitrogen atmosphere. Scanning electron microscopy (LEO SUPRA 35 VP) was used to observe the edge as well as the top surfaces of the graphene/PVA nanocomposite films. The samples were coated with gold before analysis. The crystalline structure of the samples was analyzed with an X-ray powder diffractometer (Bruker D8 Advance) using Cu K α radiation ($\lambda = 0.15418$ nm). The XRD measurements were carried out in the 2 θ angle with the range of 5–35°. Electrical characterization was carried out by means of Broadband Dielectric Spectroscopy (BDS) in the frequency range of 0.1 Hz to 1 MHz, using an Alpha-N Frequency Response Analyser, supplied by Novocontrol. A BDS-1200, parallel-plate capacitor with two gold-plated electrodes system, supplied also by Novocontrol, was used as dielectric test cell. The electrically tested samples were in the form of a circular disk with diameter 12 mm and thickness 0.5 mm. The amplitude of the time-varying applied voltage was kept constant at 1000 mV. Temperature was controlled via a Novotherm system (Novocontrol). Measurements were performed in the range of 30 to 120°C. Isothermal scans were carried out for each sample with a temperature step of 10°C. The dielectric cell was electrically shielded and both instruments were interfaced to a PC for simultaneous control and data acquisition.

3. Results and discussion

The oxidation of graphite can be confirmed by infrared spectroscopy. The FTIR spectrum (data not shown) of graphene oxide showed a broad band at about 3450 cm⁻¹ which is due to vibrations of O–H bonds. The peak at about 1100 cm⁻¹ indicates the existence of the oxygen-containing functional groups on GO, such as epoxide, which were formed during oxidation reactions [19].

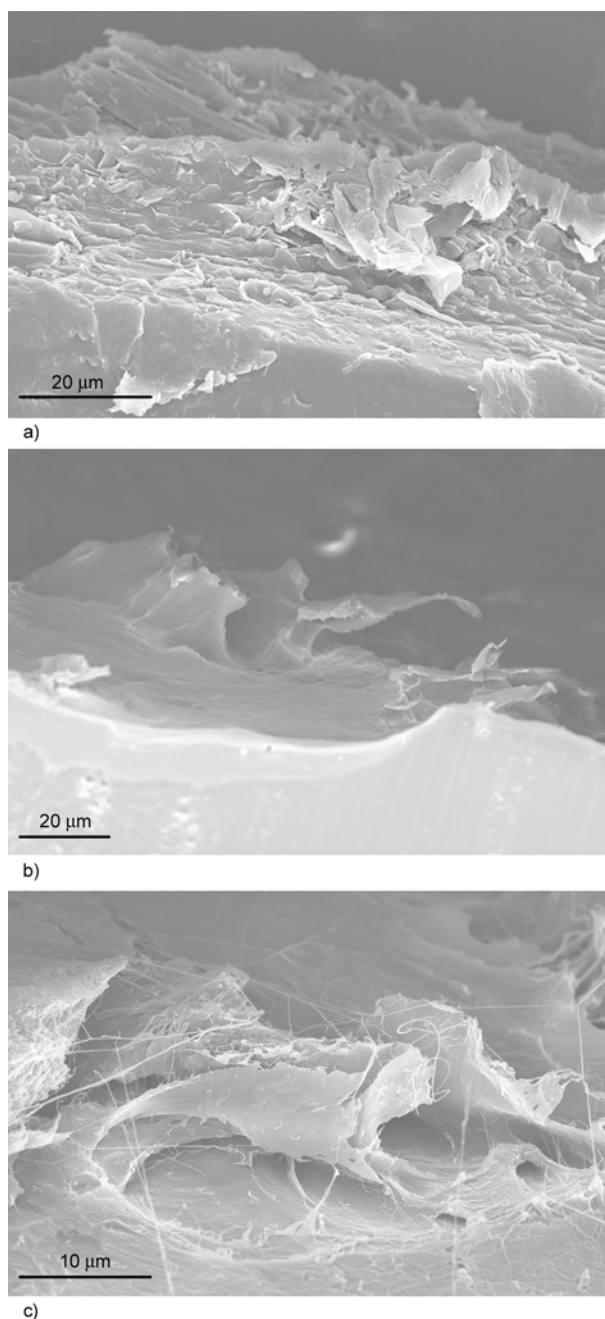


Figure 2. SEM images of composite films (1 wt% graphene loading). Cross sections of pristine- (a), GO- (b) and copolymer-modified graphene-polymer composites (c)

In order to investigate the influence of the graphene chemical functionalities on the morphology, as well as the dielectric properties of PVA-based composites, GO and copolymer-modified graphene were blended with the polymer matrix by solution mixing/hot casting process. SEM images (Figure 2) show cross sections of composite films containing 1 wt% pristine or modified nanographite. As shown in image a), pristine graphite is poorly dispersed in the composite, with agglomerates at length scales of tens of microns. Poor dispersion of unmodified graphite in solution-cast samples was expected and was a driving force for the use of chemically modified graphite, such as graphene oxide and surfactant-modified material. Characterization via SEM of the corresponding samples (images b) and c)) showed much better distribution of graphite particles homogeneously covered by the polymer. As graphene oxide does, our copolymer-modified graphene nanoplatelets can be homogeneously integrated within hydrophilic PVA matrix. The presence of ionic moieties, such as alkylamino- and carboxylates in the polymer backbone result in enhanced interfacial interactions between the filler and the matrix, whereas its amphiphilic character is responsible for the efficient exfoliation of graphene nanoplatelets by noncovalent approach. This property makes copolymer-modified graphenes a potential candidate as filler material in functional polymer composites.

The structures of GO powder, the neat polymer matrix as well as the composite films was studied by XRD (Figure 3). The XRD diffraction peak of GO sheets is appeared at 26.7° , implying that its d-spacing resembles the one of pristine graphite.

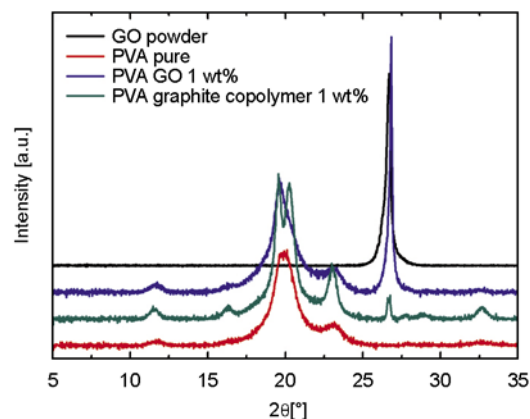


Figure 3. XRD patterns of GO powder, PVA matrix, 1 wt% GO/PVA and 1 wt% graphite/copolymer/PVA

The lack of graphene expansion can be attributed to the mild oxidative treatment of the starting material. Diffraction peaks of neat PVA film are found at 19.9° (main), as well as 11.7° , 23.1° , and 32.7° (minor) [13]. The XRD pattern of the 1 wt% GO/PVA composite film has all the peaks assigned to both GO and the matrix. This means that GO sheets were not individually dispersed in PVA matrix but rather in the form of few-layer GO platelets. On the contrary, the XRD profile of the 1 wt% graphite/copolymer/PVA composite film shows a peak of diminished intensity at 26.7° . This result indicated that graphite has been efficiently exfoliated within the PVA matrix, through its noncovalent functionalization with the amphiphilic copolymer. In addition, the crystalline structure of the matrix was slightly affected due to the incorporation of the graphene platelets.

The thermal stability of the composite materials was assessed by thermogravimetric analysis (TGA) in inert atmosphere. Figure 4a showed that the onset temperature for neat PVA degradation was about

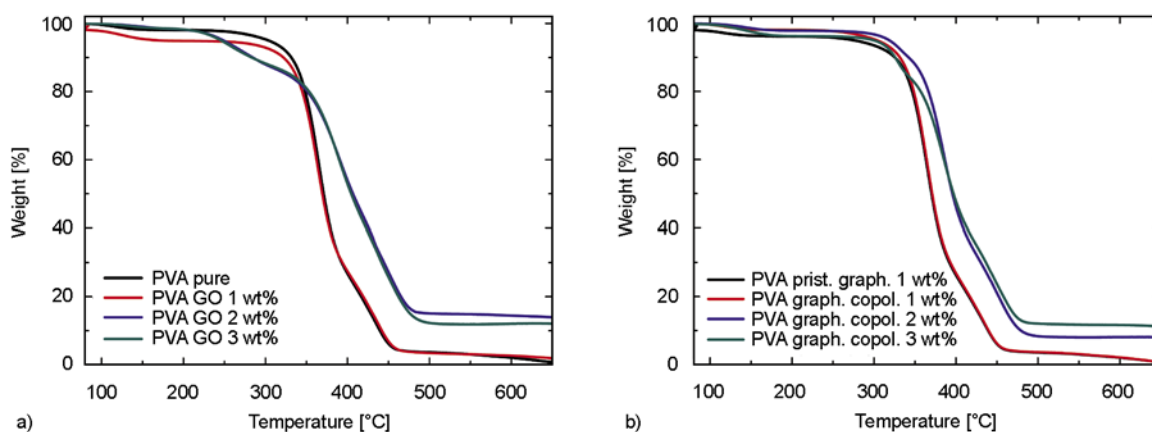


Figure 4. TGA profiles of: (a) neat matrix and GO/PVA (1, 2 and 3 wt%), (b) 1 wt% pristine graphite/PVA and graphene/copolymer/PVA (1, 2 and 3 wt%)

300°C, which was attributed to main-chain pyrolysis. At about 450°C, the total amount of polymer was seemed to be pyrolyzed. From the TGA profiles of the composite samples, it was shown that the ones containing 1 wt% pristine graphite, 1 wt% GO and 1 wt% copolymer-modified graphene exhibited similar thermal stability, as that of neat matrix. In the TGA curves of the 2 and 3 wt% GO-based composites (Figure 4), there were two steps in the degradation of the composites: The first step, from 200 to 280°C, was attributed to the elimination of the oxygen-containing groups onto the oxidized graphene nanoplatelets; the second step, roughly from 350 to 480°C, which is the degradation of the polymer, has mildly shifted to a higher temperature range with respect to the neat polymer matrix [13]. This indicates that there is a strong interaction between PVA and GO nanoplatelets at the interface, and, because of this, the mobility of the polymer chains near the interface has decreased. Similarly, concerning the graphene/copolymer/PVA samples, enhanced thermal stability was observed for the composites bearing 2 and 3 wt% graphene, comparing to the neat matrix.

To confirm the strong interaction of graphene nanostructures with the polymer matrix, differential scanning calorimetry (DSC) was used. DSC thermograms (Figure 5) obtained on heating scans showed that the integrated area of the melting transition (ΔH_m) of the samples, containing either GO or copolymer-modified graphene nanoplatelets, reached a maximum at 2 wt% filler loading. In this graphene weight fraction, it was estimated that the relative crystallinity of the copolymer-modified graphene/PVA sample was increased by about

150%, compared to the one of neat matrix. Similar results have been demonstrated for CNT/PVA composite films [20]. This crystallinity increase indicates that the polymer chains were indeed immobilized by hydrophobic and/or hydrogen bonding interactions with the graphene nanoplatelets, an effect which could support the slightly enhanced thermal stability of the composites with filler loading > 1 wt% (see TGA data). In a recent study [13], researchers observed no deviations of crystallinity values in GO/PVA composites, yet, the filler loading of the studied samples was between 0.3 and 0.7 wt%. Overall, the order of relative crystallinity in our samples (at 1 wt% graphene loading) was: copolymer-modified graphene > GO > neat matrix > pristine graphite. The fact that the sample of pristine graphite 1% wt/PVA exhibited a 15% decrease in crystallinity compared to neat PVA could be attributed to the inhomogeneous dispersion of graphite aggregates into the matrix. The melting endothermic peak of neat matrix (at about 225°C) was slightly decreased in the composites. This could be attributed to the relatively smaller crystal size of PVA, due to the intercalation of graphene platelets.

The interest in graphene-based composites stems from their potential high electrical conductivity and permittivity. Dielectric data can be analyzed by means of different formalisms, such as dielectric permittivity, ac conductivity, and electric modulus. Although, all three formalisms can be employed on the description and analysis of the occurring electrical effects, a certain formalism can be proved more effective in extracting information regarding the occurring physical mechanisms under specific con-

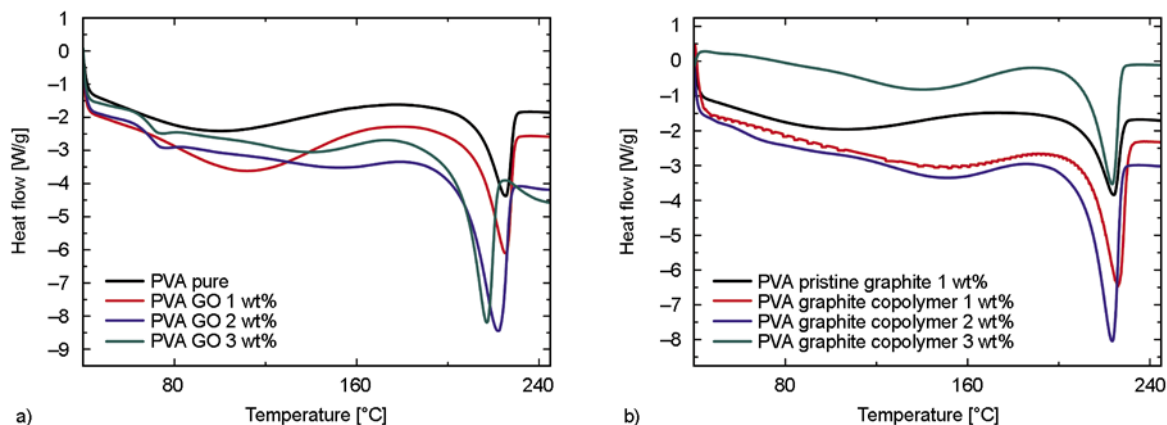


Figure 5. DSC thermograms of: (a) neat matrix and GO/PVA (1, 2 and 3 wt%), (b) 1 wt% pristine graphite/PVA, and graphene/copolymer/PVA (1, 2 and 3 wt%)

ditions. In the present study, experimental data were firstly expressed via the real and imaginary part of dielectric permittivity and then transformed into electric modulus formalism [21–23]. Figure 6a depicts the variation of real part of dielectric permittivity (ϵ') with frequency for all types of the produced composites at constant temperature (30°C) and nanofiller content (1 wt%). At low frequencies, permittivity attained higher values, in all cases, which diminished rapidly with frequency. This is reasonable since – in the low frequency region – the alternation of the field is slow, providing thus sufficient time to permanent and induced dipoles to align themselves according to the applied field, leading to enhanced polarization. Neat PVA sample and graphene/copolymer/PVA nanocomposite exhibited almost identical values, while the pristine graphite/PVA sample exhibited slightly higher values than neat matrix. On the other hand, pronounced alteration of permittivity was evident in the spectrum of GO/PVA nanocomposite. Enhanced values of (ϵ'), especially at low frequencies, can be attributed to increased conductivity, and/or interfacial polarization, and/or electrode polarization. Electrode polarization is related to the build up of space charges at the specimen-electrode interfaces and is characterized by very high values of both real and imaginary part of dielectric permittivity [21–23]. Examined samples were tested under identical experimental conditions, having similar geometrical characteristics and composition. Thus, if electrode polarization was the prevalent effect in a certain type of nanocomposite, should be also the prevalent tendency to all other types. Under this point of view, the higher values of (ϵ') could be attributed to enhanced conductivity and interfacial polarization (IP). IP results from the accumulation of unbounded charges at the interfaces of the constituents, where they form large dipoles. Its intensity is connected to the extent of the existing interfacial area within the composite system, giving thus indirect evidence of the achieved distribution of nanoinclusions [24]. Therefore, the low values of (ϵ') in graphene/copolymer/PVA and pristine graphite/PVA spectra could be assigned to lower overall conductivity and less satisfactory distribution of nanofiller, respectively. Figures 6b and 6c, respectively, present the variation of permittivity with respect of frequency for the graphene/copolymer/PVA and

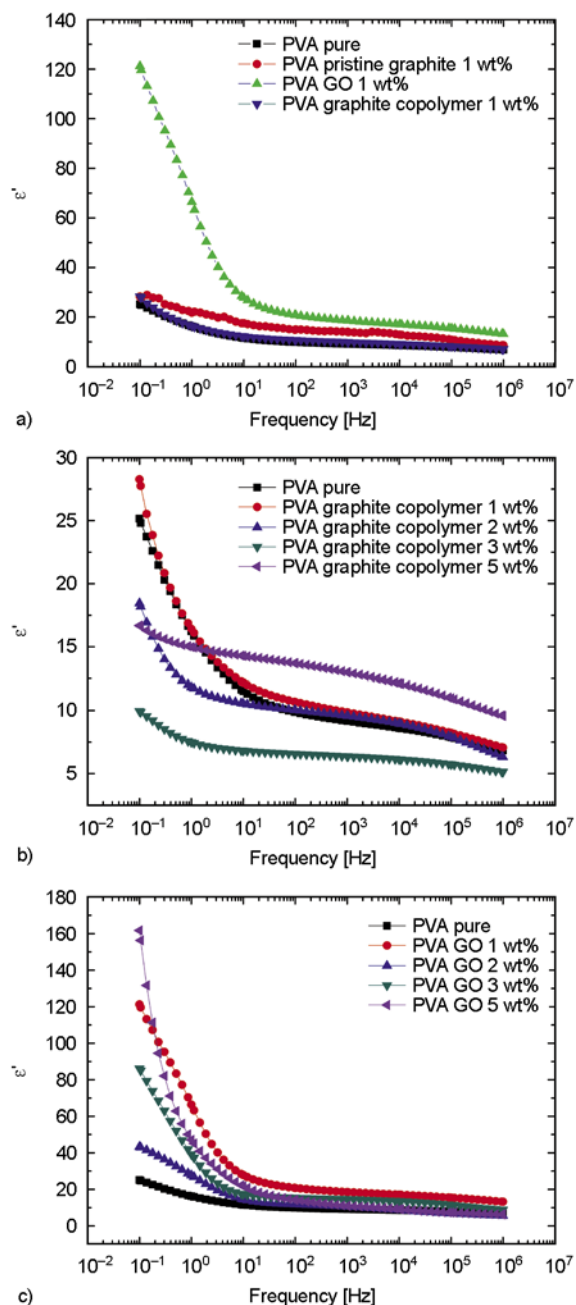


Figure 6. Variation of real part of dielectric permittivity (ϵ') with frequency for: (a) all types of the produced composites at constant temperature (30°C) and at constant filler content (1 wt%), (b) composites with copolymer-modified graphite varying the filler content, and (c) composites with GO nanoplatelets varying the filler content. In all cases pure PVA spectrum is given for comparison.

GO/PVA systems, in various filler loadings. The graphene/copolymer/PVA system displayed a tendency for diminished values of permittivity with filler content, which could be attributed to the formation of an insulating coating between graphite inclusions and PVA because of the presence of the

copolymer. On the contrary, in the spectra of GO/PVA samples, a systematic increase of (ϵ') with filler content was recorded for all samples, with the unexpected exception of PVA GO 1% wt. Since polarization and stored energy is directly proportional to permittivity, Figure 6 implies that – under the specific processing conditions – GO nanofiller provides the best, from all the examined cases, electrical enhancement.

The variation of imaginary part of electric modulus (M'') versus frequency for the PVA samples containing 2 wt% fraction of copolymer-modified graphite and GO nanoplatelets, at various temperatures, is depicted in Figure 7. The imaginary part of electric modulus (M'') vs frequency spectra revealed two relaxation mechanisms. The one recorded at high frequencies was attributed to glass transition of the polymer matrix (α -mode) and the slower one to (IP). The α -mode, which is present also in the dielectric spectrum of pure PVA, is related to motions of large parts of the main polymer chain. Dielectric loss peak position shifts to higher frequencies with increasing temperature, since thermal agitation facilitates the orientation of polar parts. Further, in the case of GO/PVA systems, loss peaks at constant temperature were recorded at relatively higher frequencies in comparison to the same set of peaks of the graphene/copolymer/PVA systems. Shift of α -mode's loss peak to higher frequency has been considered as an indication for lowering of glass transition temperature, because of weak or moderate interactions between host medium and filler [25]. Thus, the graphene/copolymer/PVA systems should be characterized by higher T_g , which is also supported by DSC spectra. In the low frequency range spectra of Figure 7, a second peak or

'hump' was observed, which corresponds to a slower process, characterized by enhanced relaxation time. As already mentioned, this process was assigned to IP. The latter appears to electrically heterogeneous systems due to the accumulation of charges at the system's interface. The presence of these charges originates from the stage of specimens' preparation. At the interface, the formed dipoles try to follow the alternation of the applied field and because of their inertia a relaxation process occurs [26].

Relaxation dynamics is related to the temperature-induced dielectric loss peak shift. Figure 8 depicts the temperature dependence of the loss peak frequency for the GO/PVA and copolymer/PVA systems for the main relaxation process (α -mode). In all cases the recorded temperature dependence deviates from a pure Arrhenius behaviour, and can be better described via the Vogel-Fulcher-Tamann (VFT) equation, according to which relaxation rate increases rapidly at lower temperatures, because of the reduction of free volume. VFT can be expressed as Equation (1):

$$f_{\max} = f_0 \exp\left(-\frac{AT_0}{T - T_0}\right) \quad (1)$$

where f_0 is a pre-exponential factor, A a constant (being a measure of activation energy), and T_0 the Vogel temperature or ideal glass transition temperature. Parameters resulted via fitting data with Equation (1) are listed in Table 1. Note that the parameter T_0 attains higher values in the systems with the copolymer, being in accordance with the obtained results from different experimental techniques, mentioned previously. In the literature it is well accepted that the glass to rubber transition follows the VFT equation [24, 27, 28], thus Figure 8 gives

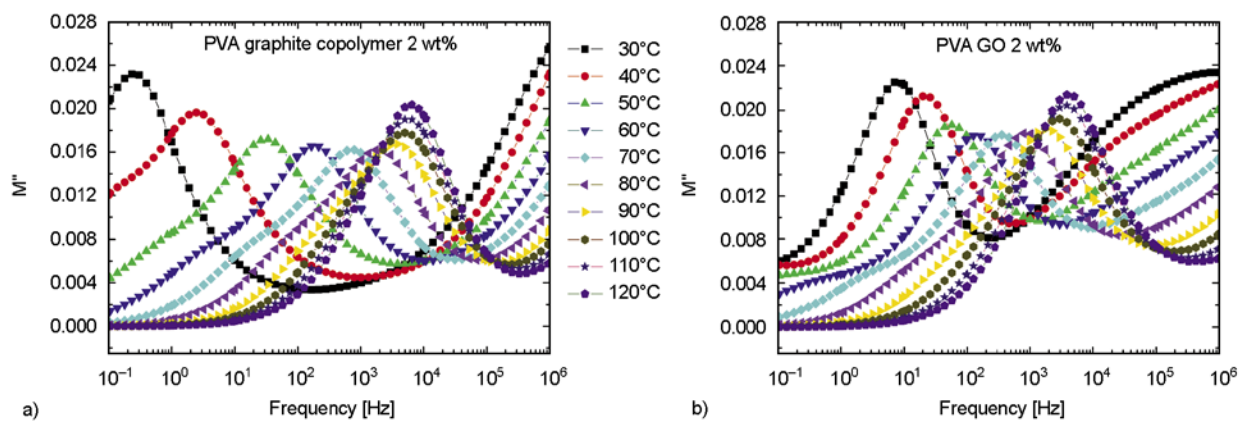
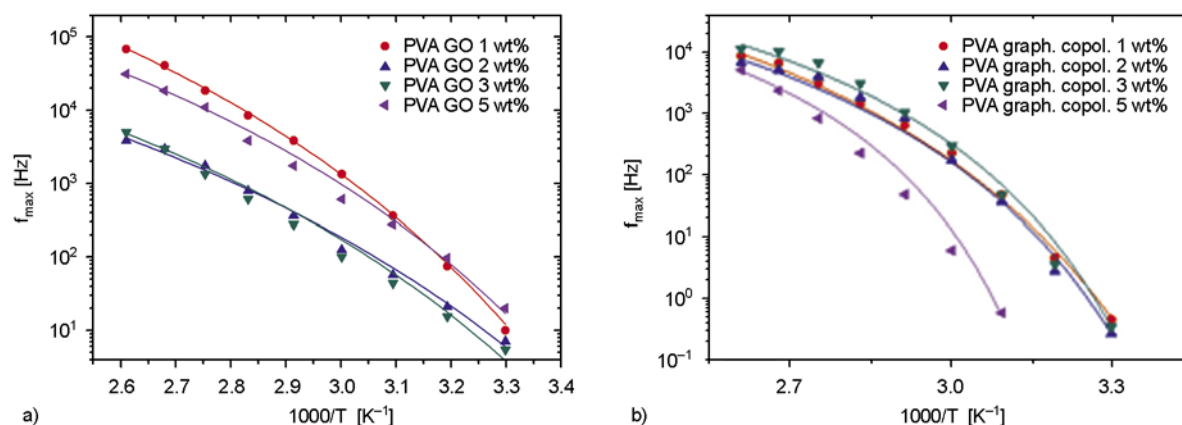


Figure 7. Variation of imaginary part of electric modulus (M'') versus frequency for the PVA samples containing 2 wt% fraction of: (a) copolymer-modified graphite and (b) GO nanoplatelets, at various temperatures

Table 1. Fitting parameters of VFT equation for α -mode of the examined systems

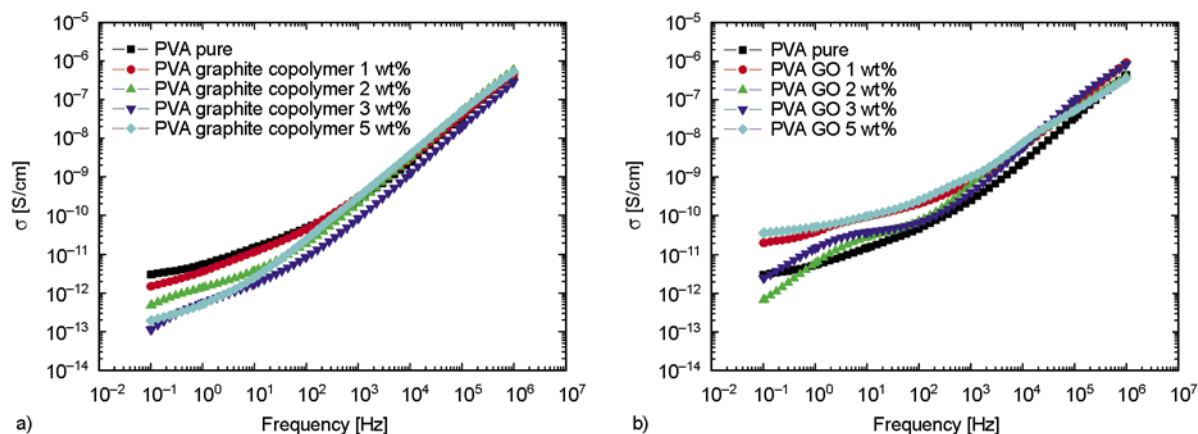
Sample	A	T_0 [K]	Sample	A	T_0 [K]
PVA GO 1% wt	6.6	220.4	PVA Graphite Copolymer 1% wt	4.3	220.4
PVA GO 2% wt	6.7	207.2	PVA Graphite Copolymer 2% wt	2.8	258.2
PVA GO 3% wt	6.3	213.7	PVA Graphite Copolymer 3% wt	2.4	264.2
PVA GO 5% wt	6.1	217.8	PVA Graphite Copolymer 5% wt	1.8	287.5

**Figure 8.** Loss peak position as a function of the reciprocal temperature for the: (a) GO/PVA systems and (b) the graphite/copolymer/PVA systems

secondary support in assigning the main relaxation mechanism of Figure 8 as α -mode.

Figure 9 shows the variation of ac conductivity with frequency for the graphene/copolymer/PVA and GO/PVA nanosystems at 30°C. Conductivity appears to be frequency dependent. In the low frequency range, conductivity tends to acquire constant values approaching its dc value, while after a critical value varies exponentially with frequency [29, 30]. This type of behaviour is common in disordered solids, appears to be in accordance with the so-called ‘ac universality law’, and is considered as a strong indication for charge migration via the hopping mechanism [25, 30]. GO/PVA systems

exhibited relatively higher values of conductivity, which was in general altered with GO loading. On the contrary, conductivity of graphene/copolymer/PVA systems was diminished with the graphene weight fraction. The latter is in accordance with the variation of permittivity with copolymer-modified graphene content (Figure 6b), providing extra support to the assumption that treating of graphenes with the copolymer results in better distribution and mutual isolation of conductive nanoinclusions. In insulating matrix-conductive inclusions composites the area between adjacent isolated conductive elements appears to be crucial. The local contact regions, between conductive inclusions, control the

**Figure 9.** Variation of ac conductivity with frequency for the: (a) graphene/copolymer/PVA and (b) GO/PVA nanosystems, at 30°C

overall conductance of the system. Abutting conductive elements separated by polymer chains restrict the conductivity values [31, 32]. Copolymer produces an electrical insulation of graphene inclusions, leading to lower values of conductivity. Finally, it should be stated that in all studied specimens, conductivity was not altered abruptly, implying that the transition from insulating to conductive behaviour has not been achieved at the examined set of composites.

4. Conclusions

In this study, PVA polymer was blended with either graphene oxide or functionalized graphene sheets. A surfactant-like block copolymer was employed as exfoliation/dispersion agent of the graphene nanoplatelets within PVA matrix through solution processing and compression molding. Concerning the graphene/PVA samples, enhanced thermal stability was observed for the composites bearing graphene loading above 1 wt%, comparing to the neat matrix. DSC thermograms showed that the integrated area of the melting transition (ΔH_m) of the samples, containing either GO or copolymer-modified graphene nanoplatelets, reached a maximum at 2 wt% filler loading. Dielectric measurements revealed that graphene/copolymer/PVA system displayed a tendency for diminished values of permittivity (ϵ') with filler content, which could be attributed to the formation of an insulating coating between graphite inclusions and PVA because of the presence of the copolymer. On the contrary, in the spectra of GO/PVA samples, a systematic increase of (ϵ') with filler content was recorded.

References

- [1] Spitalsky Z., Tasis D., Papagelis K., Galiotis C.: Carbon nanotube–polymer composites: Chemistry, processing, mechanical and electrical properties. *Progress in Polymer Science*, **35**, 357–401 (2010). DOI: [10.1016/j.progpolymsci.2009.09.003](https://doi.org/10.1016/j.progpolymsci.2009.09.003)
- [2] Cai D., Song M.: Recent advance in functionalized graphene/polymer nanocomposites. *Journal of Materials Chemistry*, **20**, 7906–7915 (2010). DOI: [10.1039/c0jm00530d](https://doi.org/10.1039/c0jm00530d)
- [3] Kim H., Abdala A. A., Macosko C. W.: Graphene/polymer nanocomposites. *Macromolecules*, **43**, 6515–6530 (2010). DOI: [10.1021/ma100572e](https://doi.org/10.1021/ma100572e)
- [4] Zhang L. L., Zhao S., Tian X. N., Zhao X. S.: Layered graphene oxide nanostructures with sandwiched conducting polymers as supercapacitor electrodes. *Langmuir*, **26**, 17624–17628 (2010). DOI: [10.1021/la103413s](https://doi.org/10.1021/la103413s)
- [5] Psarras G. C.: Nanodielectrics: An emerging sector of polymer nanocomposites. *Express Polymer Letters*, **2**, 460 (2008). DOI: [10.3144/expresspolymlett.2008.55](https://doi.org/10.3144/expresspolymlett.2008.55)
- [6] Wakabayashi K., Pierre C., Dikin D. A., Ruoff R. S., Ramanathan T., Brinson L. C., Torkelson J. M.: Polymer–graphite nanocomposites: Effective dispersion and major property enhancement via solid-state shear pulverization. *Macromolecules*, **41**, 1905–1908 (2008). DOI: [10.1021/ma071687b](https://doi.org/10.1021/ma071687b)
- [7] Du X. S., Xiao M., Meng Y. Z.: Facile synthesis of highly conductive polyaniline/graphite nanocomposites. *European Polymer Journal*, **40**, 1489–1493 (2004). DOI: [10.1016/j.eurpolymj.2004.02.009](https://doi.org/10.1016/j.eurpolymj.2004.02.009)
- [8] Wu H., Zhao W., Hu H., Chen G.: One-step *in situ* ball milling synthesis of polymer-functionalized graphene nanocomposites. *Journal of Materials Chemistry*, **21**, 8626–8632 (2011). DOI: [10.1039/c1jm10819k](https://doi.org/10.1039/c1jm10819k)
- [9] Biswas S., Fukushima H., Drzal L. T.: Mechanical and electrical property enhancement in exfoliated graphene nanoplatelet/liquid crystalline polymer nanocomposites. *Composites Part A: Applied Science and Manufacturing*, **42**, 371–375 (2011). DOI: [10.1016/j.compositesa.2010.12.006](https://doi.org/10.1016/j.compositesa.2010.12.006)
- [10] Raghu A. V., Lee Y. R., Jeong H. M., Shin C. M.: Preparation and physical properties of waterborne polyurethane/functionalized graphene sheet nanocomposites. *Macromolecular Chemistry and Physics*, **209**, 2487–2493 (2008). DOI: [10.1002/macp.200800395](https://doi.org/10.1002/macp.200800395)
- [11] Ansari S., Giannelis E. P.: Functionalized graphene sheet–poly(vinylidene fluoride) conductive nanocomposites. *Journal of Polymer Science Part B: Polymer Physics*, **47**, 888–897 (2009). DOI: [10.1002/polb.21695](https://doi.org/10.1002/polb.21695)
- [12] Dutta K., De S. K.: Electrical conductivity and optical properties of polyaniline intercalated graphite oxide nanocomposites. *Journal of Nanoscience and Nanotechnology*, **7**, 2459–2465 (2007). DOI: [10.1166/jnn.2007.429](https://doi.org/10.1166/jnn.2007.429)
- [13] Liang J., Huang Y., Zhang L., Wang Y., Ma Y., Guo T., Chen Y.: Molecular-level dispersion of graphene into poly(vinyl alcohol) and effective reinforcement of their nanocomposites. *Advanced Functional Materials*, **19**, 2297–2302 (2009). DOI: [10.1002/adfm.200801776](https://doi.org/10.1002/adfm.200801776)
- [14] Stankovich S., Dikin D. A., Dommett G. H. B., Kohlhaas K. M., Zimney E. J., Stach E. A., Piner R. D., Nguyen S. T., Ruoff R. S.: Graphene-based composite materials. *Nature*, **442**, 282–286 (2006). DOI: [10.1038/nature04969](https://doi.org/10.1038/nature04969)

- [15] Liu N., Luo F., Wu H., Liu Y., Zhang C., Chen J.: One-step ionic-liquid-assisted electrochemical synthesis of ionic-liquid-functionalized graphene sheets directly from graphite. *Advanced Functional Materials*, **18**, 1518–1525 (2008).
DOI: [10.1002/adfm.200700797](https://doi.org/10.1002/adfm.200700797)
- [16] Xu Y., Wang Y., Liang J., Huang Y., Ma Y., Wan X., Chen Y.: A hybrid material of graphene and poly (3,4-ethyldioxythiophene) with high conductivity, flexibility, and transparency. *Nano Research*, **2**, 343–348 (2009).
DOI: [10.1007/s12274-009-9032-9](https://doi.org/10.1007/s12274-009-9032-9)
- [17] Liang J., Xu Y., Huang Y., Zhang L., Wang Y., Ma Y., Li F., Guo T., Chen Y.: Infrared-triggered actuators from graphene-based nanocomposites. *The Journal of Physical Chemistry C*, **113**, 9921–9927 (2009).
DOI: [10.1021/jp901284d](https://doi.org/10.1021/jp901284d)
- [18] Kovtyukhova N. I., Ollivier P. J., Martin B. R., Mallouk T. E., Chizhik S. A., Buzaneva E. V., Gorchinskiy A. D.: Layer-by-layer assembly of ultrathin composite films from micron-sized graphite oxide sheets and polycations. *Chemistry of Materials*, **11**, 771–778 (1999).
DOI: [10.1021/cm981085u](https://doi.org/10.1021/cm981085u)
- [19] Zheng G., Wu J., Wang W., Pan C.: Characterizations of expanded graphite/polymer composites prepared by in situ polymerization. *Carbon*, **42**, 2839–2847 (2004).
DOI: [10.1016/j.carbon.2004.06.029](https://doi.org/10.1016/j.carbon.2004.06.029)
- [20] Ryan K. P., Cadek M., Nicolosi V., Blond D., Ruether M., Armstrong G., Swan H., Fonseca A., Nagy J. B., Maser W. K., Blau W. J., Coleman J. N.: Carbon nanotubes for reinforcement of plastics? A case study with poly(vinyl alcohol). *Composites Science and Technology*, **67**, 1640–1649 (2007).
DOI: [10.1016/j.compscitech.2006.07.006](https://doi.org/10.1016/j.compscitech.2006.07.006)
- [21] Tsangaris G. M., Psarras G. C., Kouloumbi N.: Electric modulus and interfacial polarization in composite polymeric systems. *Journal of Materials Science*, **33**, 2027–2037 (1998).
DOI: [10.1023/A:1004398514901](https://doi.org/10.1023/A:1004398514901)
- [22] Gatos K. G., Martínez Alcázar J. G., Psarras G. C., Thomann R., Karger-Kocsis J.: Polyurethane latex/water dispersible boehmite alumina nanocomposites: Thermal, mechanical and dielectrical properties. *Composites Science and Technology*, **67**, 157–167 (2007).
DOI: [10.1016/j.compscitech.2006.07.025](https://doi.org/10.1016/j.compscitech.2006.07.025)
- [23] Psarras G. C., Gatos K. G., Karahaliou P. K., Georga S. N., Krontiras C. A., Karger-Kocsis J.: Relaxation phenomena in rubber/layered silicate nanocomposites. *Express Polymer Letters*, **1**, 837–845 (2007).
DOI: [10.3144/expresspolymlett.2007.116](https://doi.org/10.3144/expresspolymlett.2007.116)
- [24] Kalini A., Gatos K. G., Karahaliou P. K., Georga S. N., Krontiras C. A., Psarras G. C.: Probing the dielectric response of polyurethane/alumina nanocomposites. *Journal of Polymer Science Part B: Polymer Physics*, **48**, 2346–2354 (2010).
DOI: [10.1002/polb.22120](https://doi.org/10.1002/polb.22120)
- [25] Psarras G. C.: Conductivity and dielectric characterization of polymer nanocomposites. in ‘Physical properties of polymer nanocomposites’ (eds.: Tjong S. C., Mai Y. W.) Woodhead, Cambridge, 31–69 (2010).
- [26] Mitra S., Mondal O., Saha D. R., Datta A., Banerjee S., Chakravorty D.: Magnetodielectric effect in graphene-PVA nanocomposites. *Journal of Physical Chemistry C*, **115**, 14285–14289, (2011).
DOI: [10.1021/jp203724f](https://doi.org/10.1021/jp203724f)
- [27] Psarras G. C., Soto Beobide A., Voyiatzis G. A., Karahaliou P. K., Georga S. N., Krontiras C. A., Sotiropoulos J.: Dielectric and conductivity processes in poly(ethylene terephthalate) and poly(ethylene naphthalate) homopolymers and copolymers. *Journal of Polymer Science Part B: Polymer Physics*, **44**, 3078–3092 (2006).
DOI: [10.1002/polb.20939](https://doi.org/10.1002/polb.20939)
- [28] Schönhals A.: Molecular dynamics in polymer model systems. in ‘Broadband dielectric spectroscopy’ (eds: Kremer F., Schönhals A.) Springer, Berlin, 225–293 (2003).
- [29] Tsangaris G. M., Psarras G. C., Manolakaki E.: DC and AC conductivity in polymeric particulate composites of epoxy resin and metal particles. *Advanced Composites Letters*, **8**, 25–29 (1999).
- [30] Psarras G. C.: Hopping conductivity in polymer matrix–metal particles composites. *Composites Part A: Applied Science and Manufacturing*, **37**, 1545–1553 (2006).
DOI: [10.1016/j.compositesa.2005.11.004](https://doi.org/10.1016/j.compositesa.2005.11.004)
- [31] Psarras G. C.: Charge transport properties in carbon black/polymer composites. *Journal of Polymer Science Part B: Polymer Physics*, **45**, 2535–2545 (2007).
DOI: [10.1002/polb.21278](https://doi.org/10.1002/polb.21278)
- [32] Alig I., Lellinger D., Dudkin S. M., Pötschke P.: Conductivity spectroscopy on melt processed polypropylene–multiwalled carbon nanotube composites: Recovery after shear and crystallization. *Polymer*, **48**, 1020–1029 (2007).
DOI: [10.1016/j.polymer.2006.12.035](https://doi.org/10.1016/j.polymer.2006.12.035)

Preparation of a bio-based epoxy with comparable properties to those of petroleum-based counterparts

X. Q. Liu*, W. Huang, Y. H. Jiang, J. Zhu, C. Z. Zhang

Polymers and Composites Division, Ningbo Institute of Materials Technology and Engineering, Chinese Academy of Sciences. Ningbo 315201, P.R.China

Received 12 August 2011; accepted in revised form 21 October 2011

Abstract. In this paper a bio-based epoxy with outstanding thermal and mechanical properties was synthesized using a rosin-based epoxy monomer and a rosin-based curing agent. The chemical structures of rosin based epoxy monomer and curing agent were confirmed by Nuclear Magnetic Resonance (NMR) and Fourier Transform Infrared (FT-IR) spectra. The flexural mechanical and dynamic mechanical properties as well as thermal stability of the cured epoxy were investigated. The results showed that the cured epoxy exhibited a glass transition temperature (T_g) of 164°C and its flexural strength and modulus were as high as 70 and 2200 MPa, respectively. This indicated that a wholly bio-based epoxy resin possessing high performance was successfully obtained.

Keywords: thermosetting resin, bio-based, rosin, thermal properties, mechanical properties

1. Introduction

In recent decades, more and more attention has been directed to the bio-based materials because of the diminishing petroleum oil reserves and serious environmental pollution [1]. The conversion of biomass to useful polymers or composites has considerable economical and environmental value. With the rapid development of bio-based materials, more and more natural resources, such as vegetable oil [2, 3], starch [4, 5], soy protein [6] and cellulose [7] have been used as the renewable feedstock to produce polymeric materials. Furthermore, these polymers based on renewable resources have often possessed similar properties compared with their petroleum-based counterparts. Up to now, a large quantity of bio-based polymeric materials, such as polylactic acid (PLA) [8], poly(hydroxyalkanoates) (PHA) [9], and castor oil based polyamide [10], have already been commercialized. However, compared with the achieved progress on bio-based thermoplastics, the

research on bio-based thermosetting resins, especially the thermosetting resins with high glass transition temperature (higher than 100°C) and comparable mechanical properties with petroleum-based counterparts are very limited.

To the best of our knowledge, plant oil might be the most popular renewable resource in the synthesis of bio-based thermosetting resins [3, 11–13]. But unfortunately, due to the long soft aliphatic chain in triglyceride and its low crosslink density, the resulting resin always has a low glass transition temperature (lower than 100°C) and disappointing mechanical properties. For example, Park *et al.* [3] synthesized epoxy from soybean oil and castor oil. The results showed that the glass transition temperature of the cured epoxy was lower than 50°C. Javni *et al.* [11] and Can *et al.* [12] also prepared unsaturated polyester or polyurethane from soybean oil derivatives. But their results indicated that the properties of the oil-based resin strongly depended on the

*Corresponding author, e-mail: liuxq@nimte.ac.cn
© BME-PT

incorporation of rigid petroleum chemicals [11–15]. In order to obtain the acceptable mechanical and thermal properties for practical application, the content of the rigid co-monomer was usually as high as 50% or beyond. Obviously, they were only partly bio-based materials and the petroleum based component played a critical role in determining the properties of these materials. As we know, the thermosetting resin with satisfactory performance (T_g is higher than 100°C and modulus is higher than 2000 MPa) derived from bio-based feedstock has seldom been reported [16–18].

Rosin is an important natural product. It is composed of ca. 90% acidic and ca. 10% neutral compounds. The hydrogenated phenanthrene ring structure in rosin acids is similar in rigidity to rigid petroleum chemicals. Therefore, we could make use of this bio-based feedstock to synthesize high performance polymeric materials. In our previous works, several kinds of rosin based anhydride type [19] or diimide-diacid type epoxy curing agents [20] were synthesized and their potential in improving the properties of thermosetting resins was demonstrated. In this paper, a rosin based epoxy with three functional groups was synthesized and it was cured with a rosin based curing agent. The objective of this research is to make the full use of rosin rigidity to synthesize a wholly rosin-based thermosetting resin with satisfactory properties, so as to inspire us to explore more and more renewable alternatives to petroleum based polymeric materials.

2. Experimental section

2.1. Materials

Rosin acid ($C_{20}H_{30}O_2$, purity of 75%, yellow crystals or chunks, soluble in acetone, petroleum ether, Et_2O and $EtOH$, melting point of 139–156°C) was obtained from Aladdin Reagent Co., Ltd. Shanghai. It is actually a mixture of abietic acid and other rosin neutral compounds. Sodium hydroxide, acetic acid, epichlorohydrin, maleic anhydride, *p*-toluenesulfonic acid, 2-ethyl-4-methylimidazole, tetrabutyl ammonium bromide and the common solvents were obtained from Sinopharm Chemical Reagent Co., Ltd., Shanghai, China. All the chemicals were used as received.

2.2. Characterization

NMR spectra was recorded on the Bruker (Germany) 400 MHz spectrometer. The samples were dissolved in deuterated chloroform ($CDCl_3$). 1H -NMR and ^{13}C -NMR were obtained at room temperature using Tetramethylsilane (TMS) as the internal standard. Fourier transform infrared (FT-IR) spectra were collected on a Nicolet 6700 FTIR spectrometer. The collecting wavelength was from 4000 to 400 cm^{-1} . Samples were prepared by dissolving a small amount of compound in CH_2Cl_2 , followed by smearing the solution onto a KBr crystal plate and evaporating the solvent at room temperature completely. Dynamic mechanical properties were measured by SDTA861e DMA using three-point bending method. Samples were heated from 40 to 250°C with a heating rate of 2°C/min. and frequency of 1 Hz. Thermogravimetric analysis was performed on Perkin-Elmer Diamond TG/DTA with high purity nitrogen as a purge gas at a scan rate of 10°C/min. Elemental analyses were performed by Perkin-Elmer PE2400 elemental analyzer. Flexural properties were determined by Instron model 5567 (Made in UK) with a 30 kN load cell at the crosshead speed of 2 mm/min. Unnotched izod impact testing was conducted on XJ-50Z impact testing machine and (Made in Chengde, China). For the mechanical testing, at least five specimens were tested for each sample to obtain the average value for properties.

2.3. Synthesis of maleopimaric acid (MPA)

The synthesis, collection and purification of MPA were done according to the procedure described in our former paper [19, 20]. 1H -NMR (CD_3Cl , δ ppm) 5.5 (1H), 3.1 (2H), 2.7 (1H), 2.5 (1H), 2.2 (1H), 1.78–1.24 (13H), 1.2(3H), 1.0(6H), 0.6(3H). ^{13}C -NMR (CD_3Cl , δ ppm) 185, 173, 171, 148, 125, 54, 53, 52, 49, 47, 45, 40, 38, 37, 36, 35, 33, 27, 22, 20, 20, 17, 15.76 FT-IR (cm^{-1}) 850, 930, 944, 1010, 1090, 1140, 1280, 1235, 1390, 1465, 1730, 1782, 1842, 2860, 2942, 3500–3100. Elemental analysis: Calculated %: C: 71.97, H: 8.05; Found %: C: 71.42, H: 8.11.

2.4. Synthesis of triglycidyl ester of maleopimaric acid

Into a three-necked round flask equipped with magnetic stirrer, thermometer and reflux condenser,

30 mL of distilled water and 20 g (0.05 mol) of maleopimaric acid were charged. After it was heated to 130°C, 6 g (0.15 mol) of sodium hydroxide was added gradually and the reaction was maintained at this temperature for 4 h under nitrogen atmosphere. To this mixture, 46.5 g (0.5 mol) of epichlorohydrin and 0.5 g of tetrabutyl ammonium bromide were added before the reaction was refluxed for another 6 h. It was cooled to 70°C after the addition of excess sodium hydroxide. By cooling the reaction to room temperature, the solid precipitation was removed via filtration. The filtrate was diluted by 200 mL of hexane and washed with distilled water twice. The upper hexane layer was concentrated by rotary evaporator and dried at 60°C in the vacuum oven for 12 h to get the triglycidyl ester of maleopimaric acid weighting 22 g (Yield: 75%). ¹H-NMR (CDCl₃, δ ppm) 5.4 (1H), 4.3–4.5 (3H), 3.9–4.0 (2H), 3.70–3.72 (1H), 3.11–3.32 (3H), 2.78–2.87 (6H), 2.55–2.70 (4H), 2.40–2.42 (1H), 2.18–2.3 (1H), 1.78–1.24 (13H), 1.15 (3H), 1.00–0.98 (6H), 0.59 (3H); ¹³C-NMR (CDCl₃, δ ppm) 178.2, 173.5, 172.6, 148.1, 127.4, 65.1, 56.4, 53.5, 52.4, 49.5, 47.2, 45.9, 40.6, 38.2, 37.9, 36.6, 35.6, 35.0, 32.7, 27.1, 21.9, 20.8, 20.2, 17.2, 16.9, 15.8. FT-IR (cm⁻¹) 466, 620, 721, 759, 849, 908, 1020, 1071, 1103, 1173, 1249, 1384, 1453, 1730, 2869, 2954, 3446. Elemental analysis: Calculated %: C: 67.55, H: 7.90; Found %: C: 67.23, H: 7.82.

2.5. Cured resin preparation

Maleopimaric acid and triglycidyl ester of maleopimaric acid in a 1:1 stoichiometric ratio together with catalyst 2-ethyl-4-methylimidazole (1 wt% on the basis of total weight) were dissolved in acetone

to get the uniform mixture. The solvent was removed in the vacuum oven at 60°C for 30 min. The solvent free mixture was transferred to the steel mold with the inner dimension of 64 mm × 10 mm × 5mm to prepare the specimens for mechanical and DMA test. The curing reaction was carried out at 120°C for 2 h, 150°C for 2 h and 180°C for 2 h at normal pressure. The cured samples were left still at room temperature for 12 h prior to mechanical and DMA testing.

3. Results and discussion

The reaction scheme and chemical structure for the triglycidyl ester of maleopimaric acid were shown in Figure 1. The synthesis of maleopimaric acid from rosin acid was described carefully in our former paper [19] and its triglycidyl ester was prepared by the reaction with epichlorohydrin and aqueous sodium hydroxide with tetrabutyl ammonium bromide as the phase transfer catalyst. It is easy to notice that maleopimaric acid was the intermediate product to prepare the rosin-based epoxy monomer. In our previous work, [19] maleopimaric acid was demonstrated to have great potential to replace some of conventional petroleum-based curing agents in synthesis of high performance epoxy resin. Naturally, it was also employed as a curing agent to cure its resulting triglycidyl ester and so as to prepare the wholly rosin-based epoxy resin in this research.

Figures 2a and 2b show the ¹H-NMR and ¹³C-NMR spectra for triglycidyl ester of maleopimaric acid, respectively. In Figure 2a, the peak at 5.4 ppm was assigned to the proton 1 on the unsaturated carbon. The multiple peaks appearing at 4.3–4.5, 3.9–4.0

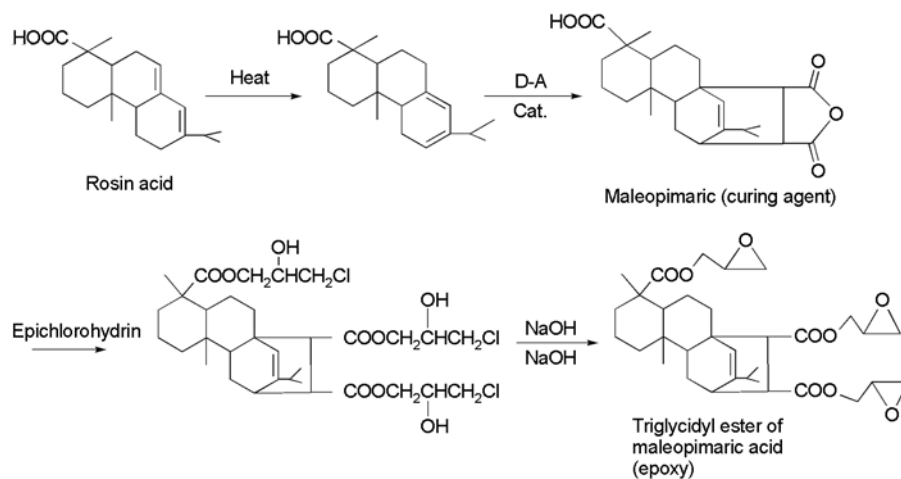


Figure 1. Synthetic route for maleopimaric acid and its triglycidyl ester

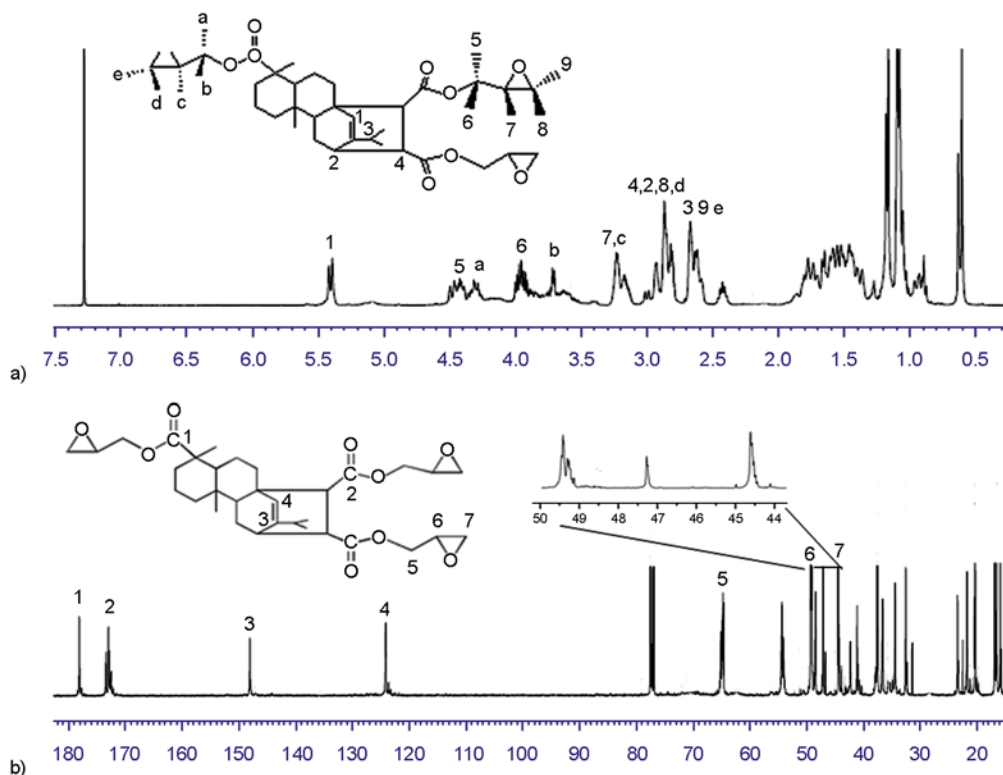


Figure 2. ^1H -NMR and ^{13}C -NMR spectra for tirglycidyl ester of maleopimaric acid

and 3.70–3.72 ppm were attributed to the proton 5, a, 6, b due to the presence of chiral carbon in the ethylene oxide ring. Other specific peaks at 3.1–3.3, 2.78–2.87 and 2.5–2.70 ppm were also identified accordingly. In Figure 2b, all the characteristic chemical shift assignments for different carbons in tirglycidyl ester of maleopimaric acid were made. Especially, from the expansion between 45 and 50 ppm, the peaks for carbon 6 and carbon 7 on the ethylene oxide ring were clearly observed.

FT-IR is useful to monitor the epoxy curing reaction. Figure 3 is the FT-IR spectra for the mixture of maleopimaric acid and tirglycidyl ester of maleopimaric acid before and after curing reaction. In the unreacted mixture, the bands at 1782 and 1842 cm^{-1} were assigned to the characteristic peak of anhydride group; the band at 1730 cm^{-1} was attributed to the carbonyl stretch ($\text{C}=\text{O}$); the peak at 908 cm^{-1} indicated the presence of oxirane rings. After curing reaction, the bands at 1782, 1842 and 908 cm^{-1} were disappeared completely, which represented the conversion of anhydride and epoxy group as well as the formation of the cured resin.

Dynamic mechanical analysis is a popular method to determine the dynamic elastic modulus of polymeric materials and observe the emergence of their

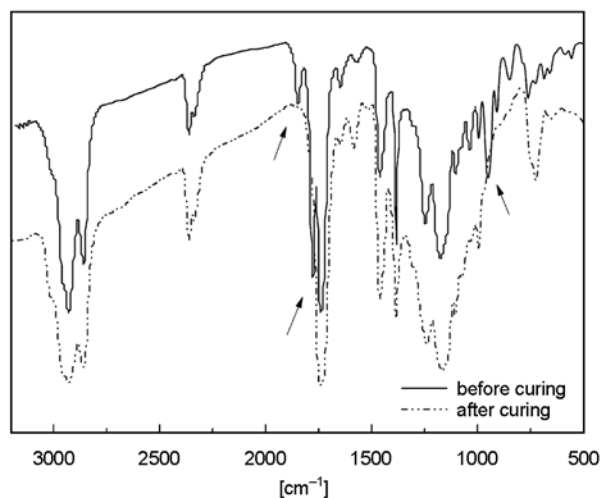


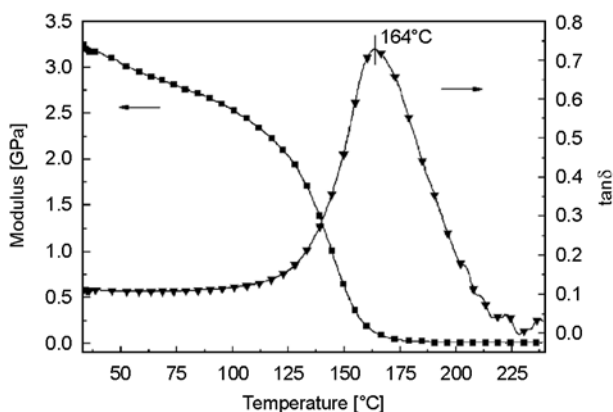
Figure 3. FT-IR spectra for the mixture of maleopimaric acid and tirglycidyl ester of maleopimaric acid before and after curing reaction

molecular mobility transition such as glass transition. Figure 4 shows the dynamic mechanical properties of tirglycidyl ester of maleopimaric acid cured with maleopimaric acid. Apparently, its glass transition temperature (T_g) and storage modulus at room temperature was as high as 164°C and 3.2 GPa, respectively. As we know, the plant oil based thermosetting epoxy, unsaturated polyester or polyurethane were widely studied [11–13, 21–23], but their

Table 1. Mechanical properties and thermal stability of cured triglycidyl ester of maleopimaric acid and petroleum-based counterparts DEGBA

Sample	Flexural modulus [MPa]	Flexural strength [MPa]	Impact strength [kJ/m ²]	Strain at break [%]	Thermal stability ^a [°C]
rosin-based epoxy	2200±30	70±1	2.1±0.2	1.9±0.3	$T_{5\%} = 328$
DGEBA	3000±200 [24]	80±3 [24]	3.2 [25]	2.6 [24]	$T_{2\%} = 319$ [26]

^atemperature of 5% or 2% thermal degradation

**Figure 4.** DMA curves for cured triglycidyl ester of maleopimaric acid

glass transition temperatures and modulus were very low (lower than 50°C). In order to increase their T_g or modulus, more than 50% petroleum-based rigid monomers must be introduced. To the best of our knowledge, this is the first wholly bio-based thermosetting resin which demonstrated outstanding dynamic mechanical properties and thermal properties

To evaluate the properties of this bio-based epoxy resin, the mechanical properties and thermal stability were also investigated. The flexural properties and impact strength were summarized in Table 1. The flexural modulus and flexural strength were about 2200 and 70 MPa, respectively, which are comparable with those of petroleum-based bisphenol A epoxy cured with different curing agents [24]. It meant that this wholly bio-based epoxy resin could be used as an engineering thermosetting resin. Although the resin shows a little bit brittleness according to the lower values of the impact strength and strain at break compared with the reported results [24, 25], it is still acceptable. The low impact strength might be due to the high crosslink density of the cured epoxy, since the epoxy monomer and curing agent both have three crosslinkable functionalities.

The thermal stability is also one of the important properties for polymeric materials and TGA is the most convenient method to determine the thermal stability and degradation behaviors of polymers. In Table 1, the TGA result for the cured triglycidyl ester of maleopimaric acid indicated that its 5% weight loss occurred at 328°C, which is also competitive with the petroleum-based bisphenol A epoxy [26]. As we know, the common cured bisphenol A epoxy usually shows their 5% weight loss temperature at about 350°C.

4. Conclusions

A novel bio-based thermosetting resin was developed using a rosin based epoxy monomer and rosin based curing agent. It demonstrated high T_g and modulus. Also its flexural properties and thermal stability were comparable to those of the conventional petroleum-based epoxy. Our results indicated the possibility to synthesize wholly bio-based thermosetting resin with high performance and inspired us to explore more and more renewable alternatives to petroleum based polymeric materials.

Acknowledgements

Financial supports provided by the Ningbo Natural Science Foundation (Grant No. 2010A610192, 2011A610127), National Natural Science Foundation of China (Grant No. NSFC51003116) and Director's Science Foundation of NIMTE were greatly acknowledged.

References

- [1] Graedel T. E., Howard-Grenville J. A.: Greening the industrial facility, perspectives, approaches and tools. Springer, New York (2005).
- [2] Jue L., Knot S., Wool R. P.: New sheet molding compound resins from soybean oil. I. Synthesis and characterization. *Polymer*, **46**, 71–80 (2005). DOI: [10.1016/j.polymer.2004.10.060](https://doi.org/10.1016/j.polymer.2004.10.060)

- [3] Park S.-J., Jin F.-L., Lee J.-R.: Synthesis and thermal properties of epoxidized vegetable oil. *Macromolecular Rapid Communications*, **25**, 724–727 (2004). DOI: [10.1002/marc.200300191](https://doi.org/10.1002/marc.200300191)
- [4] Guan J., Hanna M. A.: Extruding foams from corn starch acetate and native corn starch. *Biomacromolecules*, **5**, 2329–2339 (2004). DOI: [10.1021/bm049512m](https://doi.org/10.1021/bm049512m)
- [5] Qi Q., Wu Y., Tian M., Liang G., Zhang L., Ma J.: Modification of starch for high performance elastomer. *Polymer*, **47**, 3896–3903 (2006). DOI: [10.1016/j.polymer.2006.03.095](https://doi.org/10.1016/j.polymer.2006.03.095)
- [6] Zhang J., Mungara P., Jane J.: Mechanical and thermal properties of extruded soy protein sheets. *Polymer*, **42**, 2569–2578 (2001). DOI: [10.1016/S0032-3861\(00\)00624-8](https://doi.org/10.1016/S0032-3861(00)00624-8)
- [7] Kurimoto Y., Takeda M., Koizumi A., Yamauchi S., Doi S., Tamura Y.: Mechanical properties of polyurethane films prepared from liquefied wood with polymeric MDI. *Bioresource Technology*, **74**, 151–157 (2000). DOI: [10.1016/S0960-8524\(00\)00009-2](https://doi.org/10.1016/S0960-8524(00)00009-2)
- [8] Garlotta D.: A literature review of poly(lactic acid). *Journal of Polymers and the Environment*, **9**, 63–84 (2001). DOI: [10.1023/A:1020200822435](https://doi.org/10.1023/A:1020200822435)
- [9] Hazer B., Steinbüchel A.: Increased diversification of polyhydroxyalkanoates by modification reactions for industrial and medical applications. *Applied Microbiology and Biotechnology*, **74**, 1–12 (2007). DOI: [10.1007/s00253-006-0732-8](https://doi.org/10.1007/s00253-006-0732-8)
- [10] Corcuera M. A., Rueda L., d’Arlas F. B., Aebelaiz A., Marieta C., Mondragon I., Eceiza A.: Microstructure and properties of polyurethanes derived from castor oil. *Polymer Degradation and Stability*, **95**, 2175–2184 (2010). DOI: [10.1016/j.polymdegradstab.2010.03.001](https://doi.org/10.1016/j.polymdegradstab.2010.03.001)
- [11] Javni I., Zhang W., Petrovič Z. S.: Effect of different isocyanates on the properties of soy-based polyurethanes. *Journal of Applied Polymer Sciences*, **88**, 2912–2916 (2003). DOI: [10.1002/app.11966](https://doi.org/10.1002/app.11966)
- [12] Can E., Wool R. P., Küsefoğlu S.: Soybean and castor oil based monomers: Synthesis and copolymerization with styrene. *Journal of Applied Polymer Sciences*, **102**, 2433–2447 (2006). DOI: [10.1002/app.24548](https://doi.org/10.1002/app.24548)
- [13] Çakmaklı B., Hazer B., Tekin İ. Ö., Cömert F. B.: Synthesis and characterization of polymeric soybean oil-*g*-methyl methacrylate (and *n*-butyl methacrylate) graft copolymers: Biocompatibility and bacterial adhesion. *Biomacromolecules*, **6**, 1750–1758 (2005). DOI: [10.1021/bm050063f](https://doi.org/10.1021/bm050063f)
- [14] Alli A., Hazer B.: Poly(*N*-isopropylacrylamide) thermoresponsive cross-linked conjugates containing polymeric soybean oil and/or polypropylene glycol. *European Polymer Journal*, **44**, 1701–1713 (2008). DOI: [10.1016/j.eurpolymj.2008.04.004](https://doi.org/10.1016/j.eurpolymj.2008.04.004)
- [15] Alli A., Hazer B.: Synthesis and characterization of poly(*N*-isopropyl acryl amide)-*g*-poly(linoleic acid)/poly(linolenic acid) graft copolymers. *Journal of American Oil Chemistry Society*, **88**, 255–263 (2011). DOI: [10.1007/s11746-010-1663-1](https://doi.org/10.1007/s11746-010-1663-1)
- [16] Raquez J.-M., Deléglise M., Lacrampe M.-F., Krawczak P.: Thermosetting (bio)materials derived from renewable resources: A critical review. *Progress in Polymer Science*, **35**, 487–509 (2010). DOI: [10.1016/j.progpolymsci.2010.01.001](https://doi.org/10.1016/j.progpolymsci.2010.01.001)
- [17] Srikanth P.: Handbook of bioplastics and biocomposites engineering applications. Wiley, Salem (2011).
- [18] Grishchuk S., Karger-Kocsis J.: Hybrid thermosets from vinyl ester resin and acrylated epoxidized soybean oil (AESO). *Express Polymer Letters*, **5**, 2–11 (2011). DOI: [10.3144/expresspolymlett.2011.2](https://doi.org/10.3144/expresspolymlett.2011.2)
- [19] Liu X., Xin W., Zhang J.: Rosin-based acid anhydrides as alternatives to petrochemical curing agents. *Green Chemistry*, **11**, 1018–1025 (2009). DOI: [10.1039/B903955D](https://doi.org/10.1039/B903955D)
- [20] Liu X., Xin W., Zhang J.: Rosin-derived imide-diacids as epoxy curing agents for enhanced performance. *Bioresource Technology*, **101**, 2520–2524 (2010). DOI: [10.1016/j.biortech.2009.11.028](https://doi.org/10.1016/j.biortech.2009.11.028)
- [21] Galià M., de Espinosa L. M., Ronda J. C., Lligadas G., Cádiz V.: Vegetable oil-based thermosetting polymers. *European Journal of Lipid Science and Technology*, **111**, 87–96 (2009). DOI: [10.1002/ejlt.200900096](https://doi.org/10.1002/ejlt.200900096)
- [22] Şen S., Çaylı G.: Synthesis of bio-based polymeric nanocomposites from acrylated epoxidized soybean oil and montmorillonite clay in the presence of a bio-based intercalant. *Polymer International*, **59**, 1122–1129 (2010). DOI: [10.1002/pi.2838](https://doi.org/10.1002/pi.2838)
- [23] Keleş E., Hazer B.: Synthesis of segmented polyurethane based on polymeric soybean oil polyol and poly (ethylene glycol). *Journal of Polymers and the Environment*, **17**, 153–158 (2009). DOI: [10.1007/s10924-009-0132-0](https://doi.org/10.1007/s10924-009-0132-0)
- [24] Liu F., Wang Z., Wang Y., Zhang B.: Copolymer networks from carboxyl-containing polyaryletherketone and diglycidyl ether of bisphenol-A: Preparation and properties. *Journal of Polymer Science Part B: Polymer Physics*, **48**, 2424–2431 (2010). DOI: [10.1002/polb.22141](https://doi.org/10.1002/polb.22141)
- [25] Morell M., Ramis X., Ferrando F., Yu Y., Serra A.: New improved thermosets obtained from DGEBA and a hyperbranched poly(ester-amide). *Polymer*, **50**, 5374–5383 (2009). DOI: [10.1016/j.polymer.2009.09.024](https://doi.org/10.1016/j.polymer.2009.09.024)
- [26] Jin F.-L., Park S.-J.: Thermomechanical behavior of epoxy resins modified with epoxidized vegetable oils. *Polymer International*, **57**, 577–583 (2008). DOI: [10.1002/pi.2280](https://doi.org/10.1002/pi.2280)

Preparation and properties of poly(vinylidene fluoride) nanocomposites blended with graphene oxide coated silica hybrids

J. C. Wang, P. Chen, L. Chen, K. Wang, H. Deng, F. Chen, Q. Zhang*, Q. Fu

College of Polymer Science and Engineering, State Key Laboratory of Polymer Materials Engineering, Sichuan University, Chengdu 610065, People's Republic of China

Received 3 August 2011; accepted in revised form 27 October 2011

Abstract. Graphene oxide coated silica hybrids ($\text{SiO}_2\text{-GO}$) were fabricated through electrostatic assembly in this work, then blended with poly(vinylidene fluoride) (PVDF) by solution mixing to make PVDF nanocomposites. The interfacial interaction was investigated by scanning electron microscopy (SEM), polarized optical microscopy (POM) and Fourier transform infrared spectroscopy (FTIR). The results showed that the interfacial interaction was enhanced by adding of $\text{SiO}_2\text{-GO}$ and strong hydrogen bonds were observed. The as-made nanocomposites were investigated using standard tensile test and dynamic mechanical analysis (DMA) measurements, mechanical properties of PVDF with $\text{SiO}_2\text{-GO}$ hybrids showed limited improvement.

Keywords: polymer composites, graphene oxide, silica, interfacial interaction, hydrogen bonds

1. Introduction

Graphene is a monolayer graphite, discovered in 2004 [1]. The two-dimensional (2D) sheet carbon material has attracted much attention due to its unique properties, such as high mechanical properties [2], electronic transfer [3], thermal conductivity [4] and specific surface area [5]. Various methods have been explored to make graphene sheets, like chemical vapor deposition, epitaxial growth, mechanical or chemical exfoliations. Graphene oxide (GO) is derived from the oxidation of natural graphite flakes followed by ultrasonic treatment of the suspension. After oxidation, basal planes of GO sheets are decorated mostly with epoxide, hydroxyl, carbonyl, and carboxyl groups [6, 7]. GO is an active material, it can act as surfactant [8], covalently combined with other materials [9], etc. In recent years, graphene hybrid nanoparticles appeared [10–12],

the active GO sheets can be used to modify conventional nanoparticles which were used in polymer nanocomposites.

PVDF is a polar polymer with excellent chemical, mechanical and electrical properties [13–15]. PVDF has been widely used in many fields, such as ultra-filtration and microfiltration membranes, electrode binder in lithium ion batteries, microwave transducers and its unique applications as piezoelectric and pyroelectric materials. It is well known that nanoparticles are usually used to enhance the properties of polymer by simple blending [16–19], the interfacial interaction between polymer and nanoparticles is crucial to the enhancement. However, Jae-Wan Kim *et al.* studied the morphology, crystalline structure and mechanical properties of PVDF composites blended with silica, the composites performance poor properties. The author considered that there was

*Corresponding author, e-mail: qinzhang@scu.edu.cn

no interaction between silica and PVDF [20]. Thus, the modification of silica in order to achieve a better interfacial interaction is necessary.

In this work, graphene oxide coated silica nanoparticles ($\text{SiO}_2\text{-GO}$) were fabricated by electrostatic assembly, these nanoparticles were solution blended with PVDF, the interfacial interaction and mechanical properties were investigated.

2. Experiments

2.1. Materials

Graphite powders were purchased from Qingdao Black Dragon graphite Co., Ltd, China. Sub-micro sized silica (average size = 500 nm) was purchased from Admatechs Co., Ltd, Japan. Potassium permanganate (KMnO_4), sulfuric acid (H_2SO_4 , 98%), sodium nitrate (NaNO_3) and hydrogen peroxide (H_2O_2) were purchased from Kermel Chemical reagent plant (Chengdu, China), all reagents were used as received. 3-aminopropyltriethoxysilane (APS) was provided from commercial sources and used without purification. PVDF (FR901) was purchased from Shanghai 3F New Material Co., Ltd. China.

2.2. Preparation of graphene oxide coated silica hybrids

The surface modification of SiO_2 with APS coupling agent was carried out in liquid phase. In a typical process, SiO_2 powder (10 g) was firstly added to 150 mL ethanol, premixed and then ground by planetary ball mill with zirconia balls (400 rpm, 30 min) to get well dispersed SiO_2 suspension. After the addition of another 150 mL ethanol, 0.5 mL silane coupling agent APS was added into the suspension. The mixture was stirred, heated up to 50°C for 12 h, the obtained particles were filtered from the mixture, washed with ethanol and deionized water five times and dried under vacuum.

GO was made of natural graphite by Hummer's method [21]. The size of GO monolayer sheets were mostly 2~6 μm , the thickness was about 1.3 nm. Exfoliation of GO was achieved by sonication for 2 h in an aqueous solvent, followed by centrifugation to remove the unexfoliated GO sheets (3000 rpm, 30 min). A diluted and well dispersed GO colloid solution with a concentration of 0.4 mg/mL was employed in the succeeding process.

GO coated silica hybrids ($\text{SiO}_2\text{-GO}$) were fabricated by simple mixing positively charged $\text{SiO}_2\text{-NH}_2$

particles and negatively charged GO dispersion. As in a typical process, 400 mL $\text{SiO}_2\text{-NH}_2$ (20 mg/mL) were added into a 200 mL aqueous GO suspension (0.4 mg/mL) under mild magnetic stirring for 1 h. Stopped stirring when the aqueous solution became transparent, then GO precipitated with $\text{SiO}_2\text{-NH}_2$ at the bottom of the beaker. The sediment solid ($\text{SiO}_2\text{-GO}$ hybrids) were collected and washed with water for several times to remove the unbound GO and afterwards dried under 60°C and grounded before use.

2.3. Fabrication of PVDF/ $\text{SiO}_2\text{-GO}$ composites

Different amounts of $\text{SiO}_2\text{-GO}$ and SiO_2 were firstly added to 50 mL dimethyl acetylamide (DMAc) respectively, the solution was sonicated for 4 h and then transferred to a flask for mechanical stirring. After that, 8 g PVDF were added to the solution in batches (4 batches, 2 g every 30 min), stirred at 60°C for 12 h to get homogenous solution. Subsequently, the solution was co-precipitated with deionized water and dried in an oven at 60°C for 24 h to remove remaining solvent, the precipitate was heat compressed at 210°C . Pure PVDF was fabricated in the same way for comparison. The weight ratios of the nanoparticles in the composites were 5, 10, 15, 20% (Filler/PVDF) respectively.

2.4. Characterization

Morphological studies were carried out using a scanning electron microscope (SEM, JEOL JSM-5900LV) in order to investigate the interface between nanofillers and PVDF matrix in the composites. The SEM images were obtained on the fracture surface of samples at an accelerating voltage of 20 kV. Transmission electron microscopy (TEM) observations were carried out to examine the micro-morphology of hybrids on a Tecnai F20 S-TWIN TEM under an acceleration voltage of 200 kV.

Morphological observations on crystallites of PVDF composites were conducted on a polarized optical microscopy (POM, Leica DMLP) equipped with a hot stage (Linkam THMS 600) under crossed polarizers. All samples were first inserted between two microscope cover slips and squeezed at 210°C to obtain a slice with a thickness around 30 μm . Subsequently, the as-prepared slice was transferred to the hot stage and held at 210°C for 3 minutes to

achieve thermal equilibrium. It was followed by cooling to 40°C at 2°C/min. The POM micrographs were recorded by a digital camera.

Infrared spectra from 4000 to 650 cm^{-1} were obtained by a Nicolet 6700 Fourier Transform Infrared Spectroscopy (FTIR) instrument using ATR method, 32 accumulated cycles, 4 accuracy.

The dynamic properties of the materials were investigated using a Dynamic Mechanical Analyzer (DMA, TA Q800). The mode was Film-Tension, preload force was 0.01 N, amplitude was 10 μm , frequency was 1 Hz and heating rate was 3°C/min. Standard tensile tests were performed using a tensile testing machine (SANSI, ShenZhen, China) with a cross-head speed of 5 mm/min at room temperature (23°C). The tensile strength at yield was determined according to GB/T 1040-92 standard. The values of the tensile strength were calculated as averages over 5 specimens for each composition.

3. Results and discussion

3.1. Self-assembly of graphene oxide coated silica

The overall synthetic procedure of graphene oxide coated silica was demonstrated in Figure 1, graphene oxide was negatively charged because of its plenty of functional groups such as carboxylic acid and phenolic hydroxy groups. Raw SiO_2 particles were modified with APS, then it could form positively charged $\text{SiO}_2\text{-NH}_3^+$ particles due to the ionization of amino groups [22]. Therefore, GO sheets were easy to self assemble with $\text{SiO}_2\text{-NH}_3^+$ by electrostatic force and the $\text{SiO}_2\text{-GO}$ hybrids were obtained.

Raw SiO_2 and $\text{SiO}_2\text{-GO}$ powders were shown in Figure 2a and 2b respectively, it is well known that the colour of graphene oxide is brown, $\text{SiO}_2\text{-GO}$ was brown compared with white raw SiO_2 , indicating the existence of graphene oxide. However, was silica coated with graphene oxide? SEM photographs of raw SiO_2 and $\text{SiO}_2\text{-GO}$ at the same magnification were shown in Figure 2d and 2e respectively. Compared with the smooth surface of SiO_2 , the surface of $\text{SiO}_2\text{-GO}$ was rough and somewhat wrinkled. It was more obvious at the TEM image of $\text{SiO}_2\text{-GO}$ (Figure 2c), ultrathin graphene oxide sheets coated the SiO_2 particles. Therefore, the experimental results above all proved that the $\text{SiO}_2\text{-GO}$ hybrids have been successfully made.

3.2. Interfacial interaction between PVDF and nanofillers

In order to study the interfacial interaction between PVDF and nanofillers, SEM photographs were observed. As shown in Figure 3a and 3b were PVDF with SiO_2 at low and high magnification respectively, a large number of SiO_2 was pulled out of the PVDF matrix and left many holes on the fracture surface, the few number of SiO_2 that was left in the fracture surface showed very smooth surface, and the gaps between PVDF matrix and SiO_2 were obvious clear, these all indicated that the interfacial interaction between PVDF matrix and SiO_2 was very poor. However, compared with PVDF/ SiO_2 , there were fewer holes in the fracture surface of PVDF/ $\text{SiO}_2\text{-GO}$ (Figure 3c and 3d), PVDF was somewhat adhered to the $\text{SiO}_2\text{-GO}$ particles, the combination

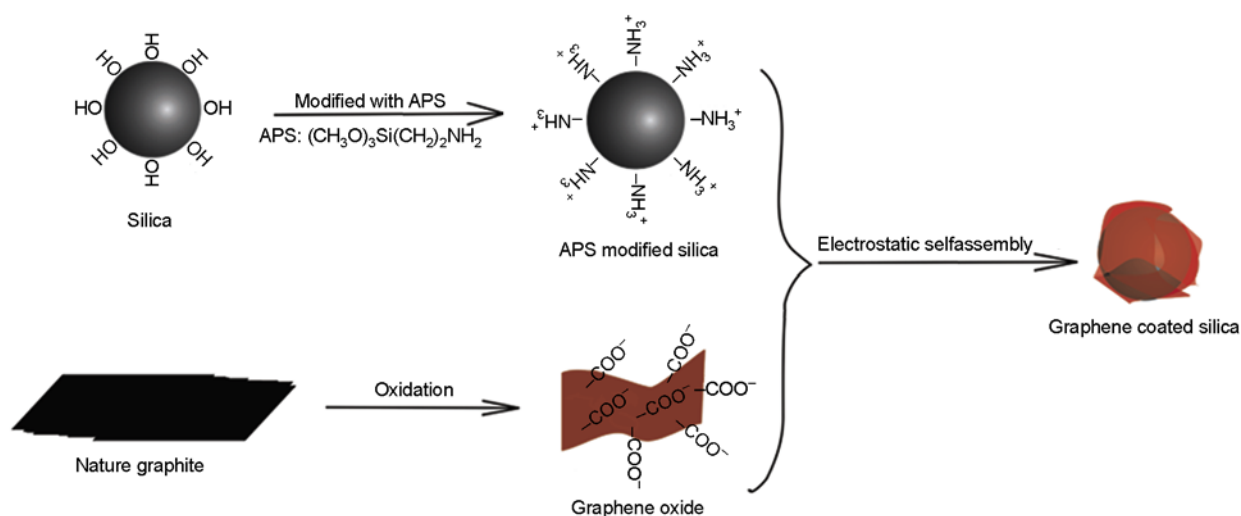


Figure 1. Illustration of the overall synthetic procedure of graphene oxide coated silica

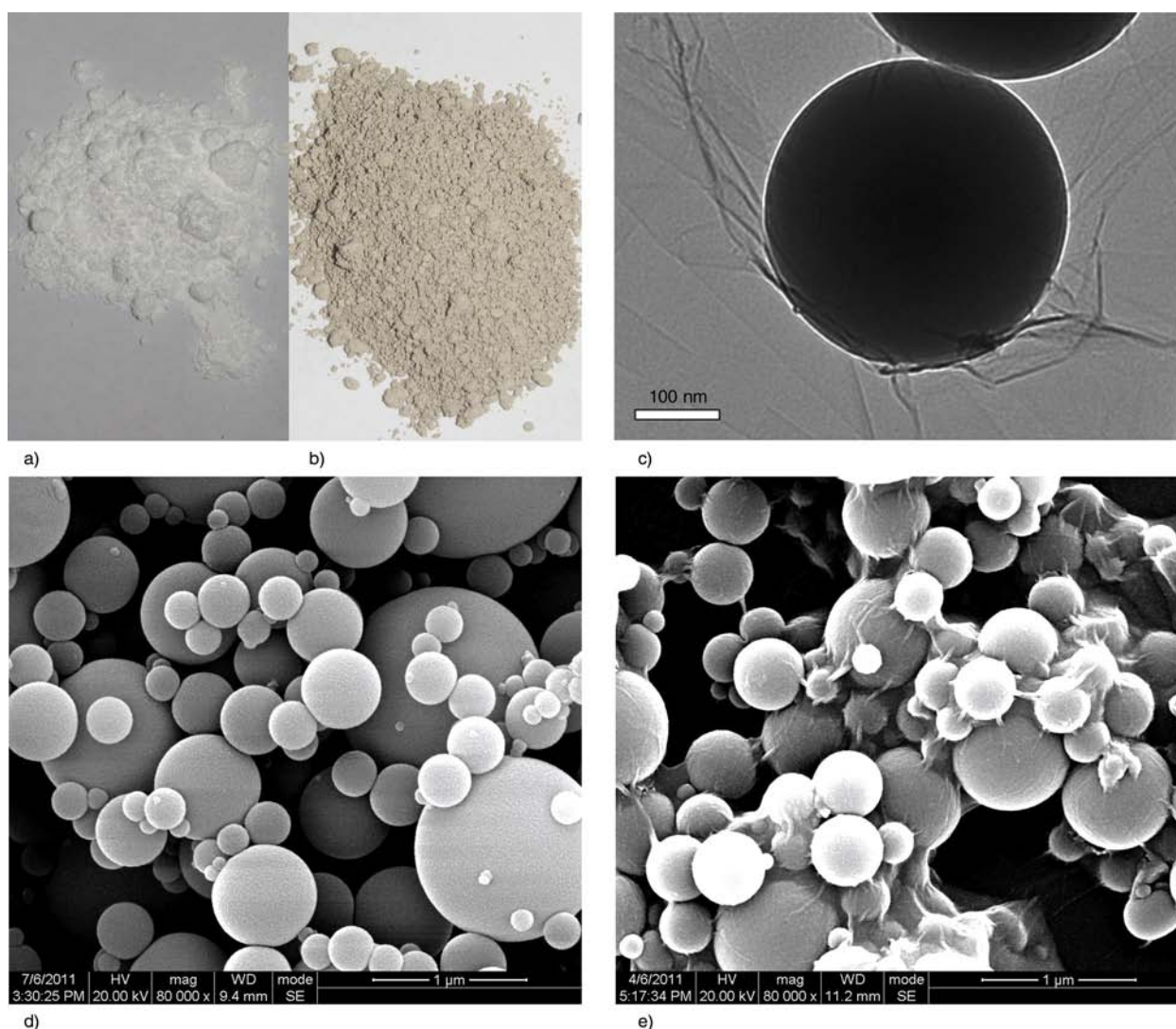


Figure 2. Digital photographs of raw SiO₂ (a) and as-made SiO₂-GO hybrid (b), Transmission electron microscopy (TEM) image of SiO₂-GO hybrids (c), scanning electron microscope (SEM) images of the raw SiO₂ (d) and created SiO₂-GO hybrid (e) at the same magnification

between matrix and SiO₂-GO was better. Therefore, after the silica was coated with graphene oxide, the interfacial interaction was enhanced in PVDF/SiO₂-GO composites.

The enhancement of interfacial interaction in PVDF/SiO₂-GO was also proved by another characterization method. It was reasonable that the plenty of functional groups like epoxide, hydroxyl, carbonyl, and carboxyl groups would have a strong interaction with the PVDF's molecular chains. The C-F bond of PVDF and hydroxyl or carboxyl groups of graphene oxides were supposed to form hydrogen bonds in the PVDF/SiO₂-GO composites, the hydrogen bonds would support the enhancement of interfacial interaction. It is well known that the characteristic peaks in infrared spectra will show

'red shift' when hydrogen bonds are formed. Therefore, FTIR investigation (Figure 4) was made to prove this idea, SiO₂ showed a strong peak at 1112.6 cm⁻¹, which could be assigned as Si-O-Si vibration, while PVDF/15 % SiO₂ showed a peak of Si-O-Si vibration at 1107.3 cm⁻¹, which implied slight red shift, because a few hydrogen bonds were formed. The peak of Si-O-Si vibration of SiO₂-GO was located at 1117.3 cm⁻¹, while that of PVDF/15% SiO₂-GO was located at 1104.7 cm⁻¹. The obvious red shift indicated that there were substantial hydrogen bonds in the PVDF/SiO₂-GO composites, which could be attributed to the plenty of functional groups of the graphene oxide. Thus, compared to the PVDF/SiO₂ composites, the substantial hydrogen bonds between PVDF and SiO₂-GO would

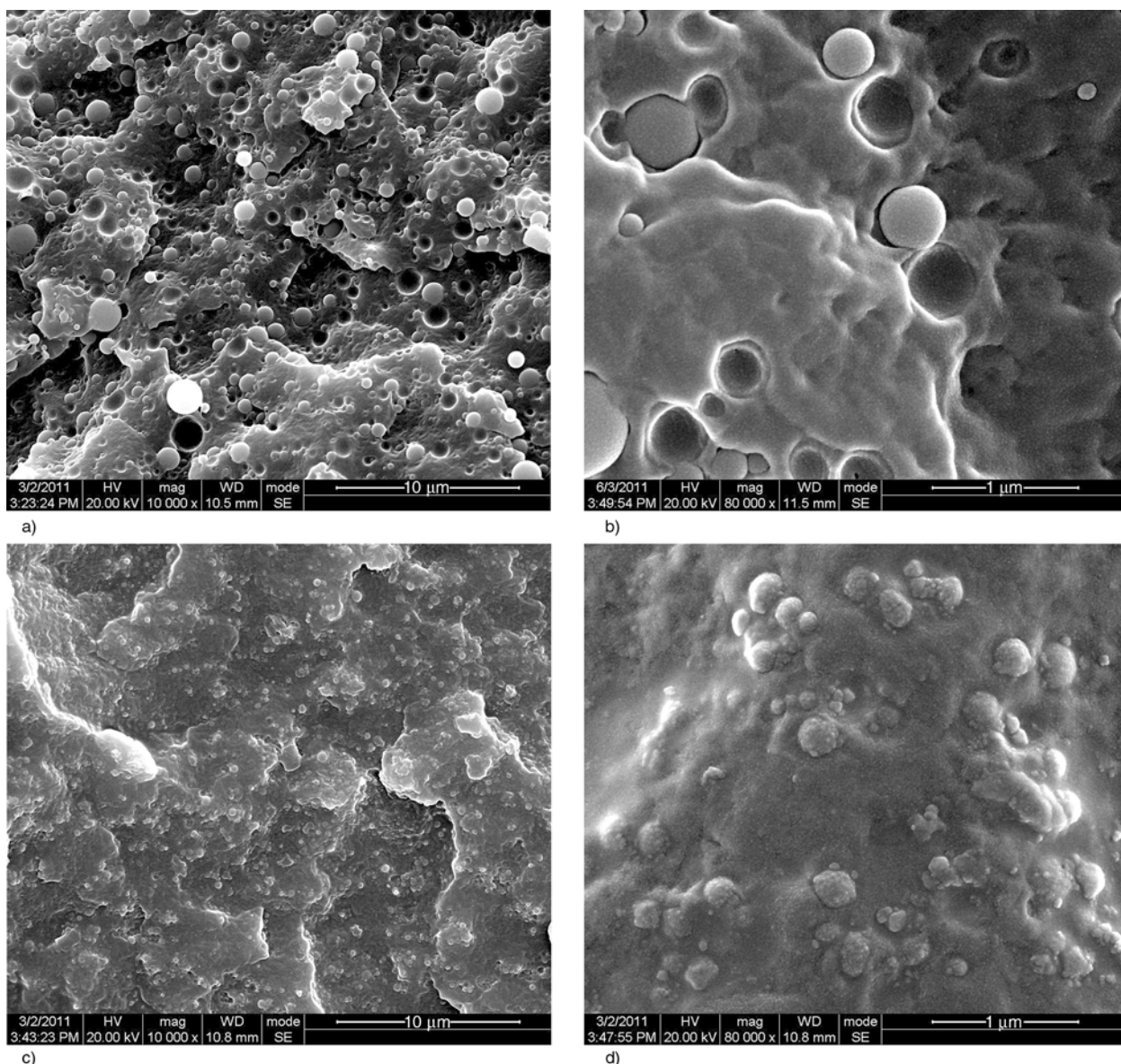


Figure 3. SEM images of PVDF with 20% SiO₂ at low magnification (a) and high magnification (b); PVDF with 20% SiO₂-GO at low magnification (c) and high magnification (d)

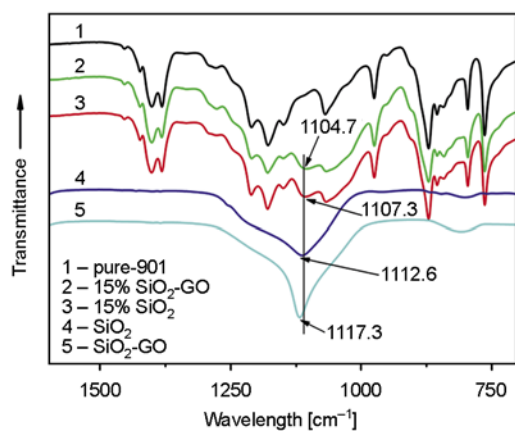


Figure 4. FTIR spectrums of PVDF nanocomposites and the fillers

improve the interfacial behaviour and may have an effect on the mechanical properties of the PVDF/SiO₂/GO composites.

A decrease of the spherulite size, results in a stronger interaction between PVDF chains and nanoparticles [23]. The morphologies of crystals were shown in Figure 5. The slice of samples were relatively thick for the low melt index of PVDF, so the serious overlap of crystal in the picture was hard to avoid. Compared with pure PVDF, the spherulite size of PVDF in PVDF/5% SiO₂ composite was larger, which indicated that the interaction between PVDF chains and SiO₂ was weak. However, the spherulite size of PVDF in PVDF/5% SiO₂-GO composite was obviously smaller than that of pure

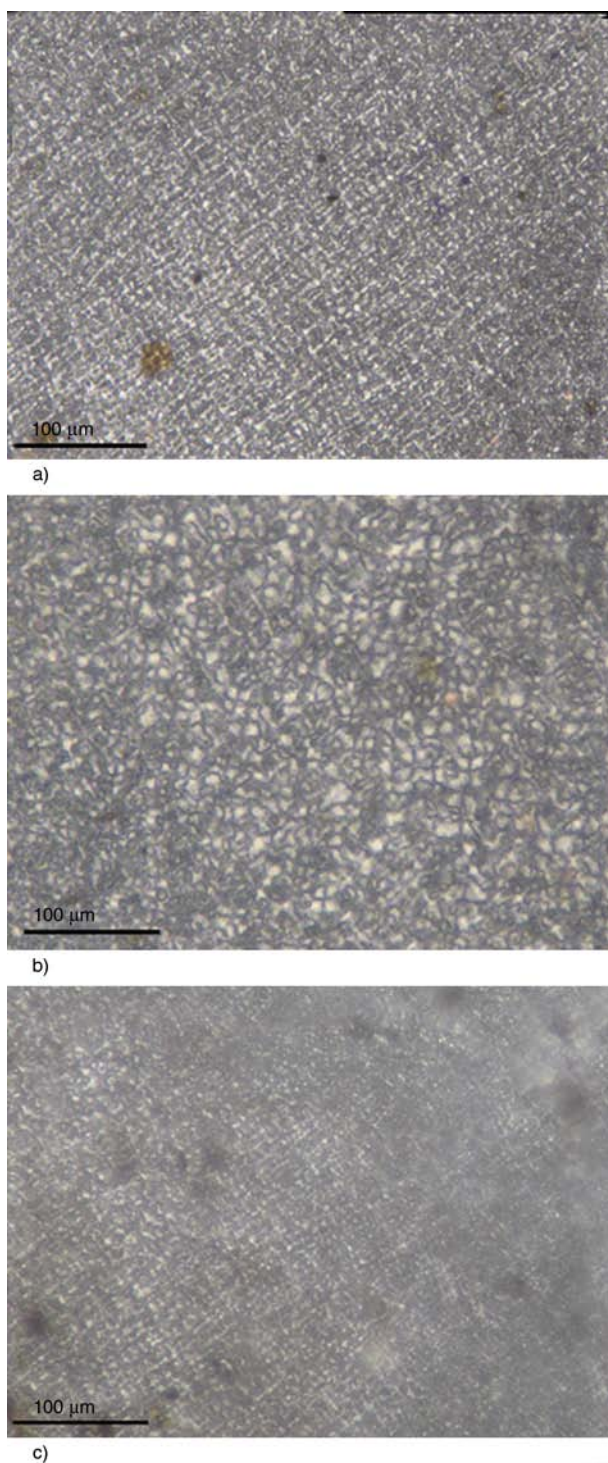


Figure 5. Crystal morphologies of PVDF (a), PVDF with 5% SiO₂ (b) and 5% SiO₂-GO (c) respectively observed by Polarized optical microscopy (POM)

PVDF, indicating a better interfacial interaction between PVDF chains and SiO₂-GO particles.

In summary, it can be concluded that the interfacial interaction between PVDF and SiO₂-GO has been largely improved compared with that between PVDF and silica. That is to say, after SiO₂ particles were

coated with graphene oxide, the interfacial interaction was greatly enhanced in PVDF/SiO₂-GO composites. It should be a potential method to improve the interfacial interaction between polymer and fillers.

3.3. Mechanical properties of PVDF nanocomposites

Since the interfacial interaction was enhanced in the PVDF/SiO₂-GO composites and graphene show high mechanical properties [2], the mechanical properties of PVDF/SiO₂-GO composites were supposed to be enhanced. Figure 6a showed tensile strengths of PVDF/SiO₂ and PVDF/SiO₂-GO composites. The tensile strength of PVDF/SiO₂-GO composites show a limited improvement compared with PVDF/SiO₂ composites with different filler contents. The tensile strength of pure PVDF was 45.6 MPa, with increasing loading of SiO₂-GO, the tensile strength of PVDF/SiO₂-GO increased. The tensile strength of PVDF containing 20% SiO₂-GO was 51.2 MPa, which was about 12% more than that of pure PVDF. While the tensile strength of PVDF/SiO₂ decreased with the increasing loading of SiO₂, it was subjected to severe decrease when the loading of SiO₂ was 20%, this may be due to the aggregation of SiO₂ in PVDF matrix and poor interfacial interaction between PVDF and SiO₂. The limited improvement of tensile strength could be ascribed to the good dispersion of SiO₂-GO and interfacial enhancement between SiO₂-GO nanoparticles and PVDF matrix. The basal planes of graphene oxide were most likely decorated with epoxide, hydroxyl, carbonyl and carboxyl groups. Thus, graphene oxide coated silica with high polarity dispersed well in polar PVDF. The good interaction between the functional groups of SiO₂-GO and PVDF molecular chains would result in better interfacial interaction.

The tensile modulus is shown in Figure 6b. Tensile modulus of PVDF/SiO₂-GO and PVDF/SiO₂ both increased with the increasing amount of fillers, this increase could be attributed to the presence of silica, because it was a common phenomenon when a polymer was blended with rigid particles. We noticed that the modulus of PVDF/SiO₂-GO was slightly lower than that of PVDF/SiO₂. In order to confirm this experimental result, we did a dynamic mechanical analysis (DMA test). Figure 7 showed that stor-

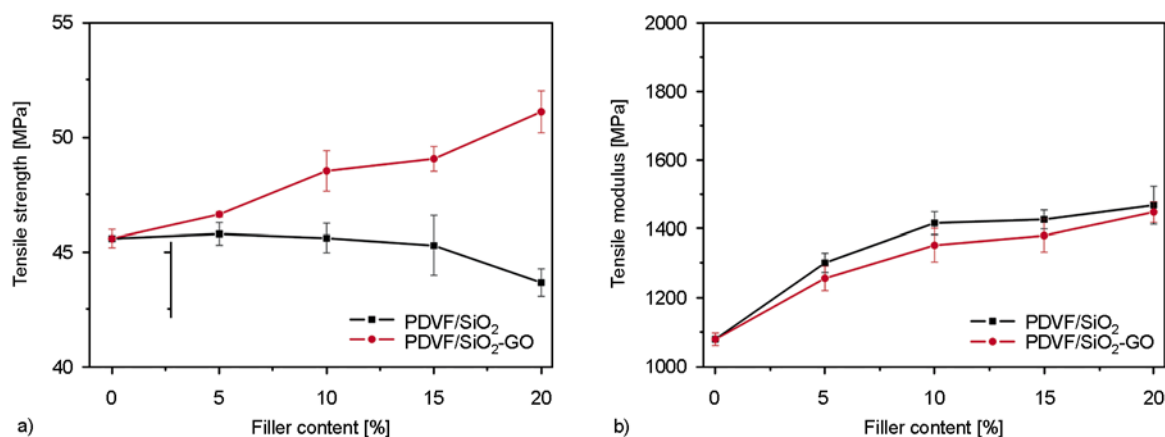


Figure 6. Tensile strength (a) and tensile modulus (b) of PVDF with SiO₂-GO and SiO₂ respectively

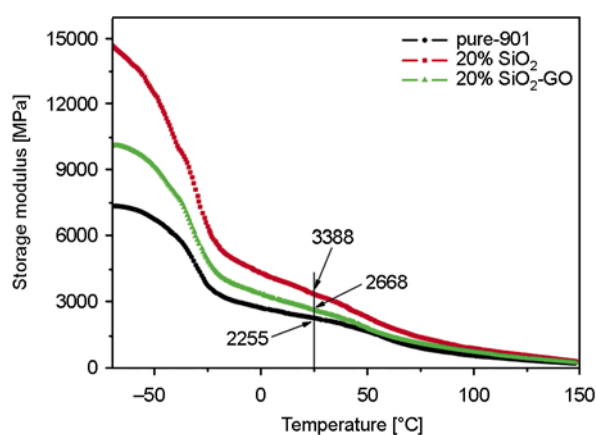


Figure 7. Storage modulus of PVDF with SiO₂-GO and SiO₂ respectively carried out by dynamic mechanical analysis (DMA) measurement

age modulus of PVDF/SiO₂ and PVDF/SiO₂-GO were obviously higher than that of pure PVDF. Even at 25°C, the storage modulus of PVDF/SiO₂ (3388 MPa) was 50% higher than that of PVDF (2255 MPa), while the storage modulus of PVDF/SiO₂-GO (2668 MPa) was only 18% higher than that of PVDF (2261 MPa). This result was similar to that of tensile tests, it confirmed that the rigid silica particle would result in an increase of modulus. However, the modulus increase of PVDF/SiO₂-GO was relatively lower than that of PVDF/SiO₂.

Why did the tensile strength of PVDF/SiO₂-GO improved only by 12% at most and the modulus was relatively lower than that of PVDF/SiO₂? There were two possible explanations: 1) The APS layer between silica and graphene oxide may cause the rigidity of SiO₂-GO to decrease, compared with the pure silica. Thus, the modulus of PVDF/SiO₂-GO was relatively lower than that of PVDF/SiO₂. 2) Recently,

researchers proposed that the graphene oxide contains many oxidative debris after oxidation of natural graphite flakes [24]. Maybe the small molecules (oxidative debris) mixed with graphene oxide could act as plasticizer, thus do harm to the improvement of strength of PVDF/SiO₂-GO and result in the relatively lower modulus of PVDF/SiO₂-GO.

4. Conclusions

Graphene oxide coated silica hybrids (SiO₂-GO) were fabricated by electrostatic assembly, and SiO₂-GO hybrids based PVDF nanocomposites were made successfully. SEM pictures showed that there were many SiO₂ particles pulled out of the fracture surface of PVDF/SiO₂, the interface between PVDF matrix and SiO₂ was clear. While for PVDF/SiO₂-GO, there were few SiO₂-GO particles pulled out of the fracture surface, SiO₂-GO particles were mostly embedded in the PVDF matrix, the interface between PVDF matrix and SiO₂-GO was unclear. This indicated that the interfacial interaction between PVDF matrix and SiO₂-GO was greatly enhanced. Using infrared spectra investigation, the vibration peak of silica in PVDF/SiO₂-GO showed an obvious 'red shift' compared with SiO₂-GO, indicating the strong hydrogen bonds forming between PVDF matrix and SiO₂-GO, which will be beneficial for the interfacial enhancement. Compared with neat PVDF, crystallite size of PVDF/SiO₂-GO decreased, while those of PVDF/SiO₂ increased. This indicated that, compared with PVDF/SiO₂, PVDF/SiO₂-GO had a better interfacial interaction. Since the interface was greatly enhanced in PVDF/SiO₂-GO composites, the corresponding mechanical properties were exam-

ined. The tensile strength of PVDF/SiO₂-GO showed limited improvement, and modulus was relatively lower, compared with PVDF/SiO₂.

Acknowledgements

We express our sincere thanks to the Program for the New-Century Excellent Talents of Ministry of Education of China (NCET-10-0580) for financial support.

References

- [1] Novoselov K. S., Geim A. K., Morozov S. V., Jiang D., Zhang Y., Dubonos S. V., Grigorieva I. V., Firsov A. A.: Electric field effect in atomically thin carbon films. *Science*, **306**, 666–669 (2004). DOI: [10.1126/science.1102896](https://doi.org/10.1126/science.1102896)
- [2] Lee C., Wei X., Kysar J. W., Hone J.: Measurement of the elastic properties and intrinsic strength of monolayer graphene. *Science*, **321**, 385–388 (2008). DOI: [10.1126/science.1157996](https://doi.org/10.1126/science.1157996)
- [3] Rao C., Sood A., Subrahmanyam K., Govindaraj A.: Graphene: The new two-dimensional nanomaterial. *Angewandte Chemie International Edition*, **48**, 7752–7777 (2009). DOI: [10.1002/anie.200901678](https://doi.org/10.1002/anie.200901678)
- [4] Balandin A. A., Ghosh S., Bao W., Calizo I., Teweldebrhan D., Miao F., Lau C. N.: Superior thermal conductivity of single-layer graphene. *Nano Letters*, **8**, 902–907 (2008). DOI: [10.1021/nl073187z](https://doi.org/10.1021/nl073187z)
- [5] Schniepp H. C., Li J-L., McAllister M. J., Sai H., Herrera-Alonso M., Adamson D. H., Prud'homme R. K., Car R., Saville D. A., Aksay I. A.: Functionalized single graphene sheets derived from splitting graphite oxide. *The Journal of Physical Chemistry B*, **110**, 8535–8539 (2006). DOI: [10.1021/jp060936f](https://doi.org/10.1021/jp060936f)
- [6] Cai W., Piner R. D., Stadermann F. J., Park S., Shaibat M. A., Ishii Y., Yang D., Velamakanni A., An S. J., Stoller M., An J., Chen D., Ruoff R. S.: Synthesis and solid-state NMR structural characterization of ¹³C-labeled graphite oxide. *Science*, **321**, 1815–1817 (2008). DOI: [10.1126/science.1162369](https://doi.org/10.1126/science.1162369)
- [7] Kim F., Cote L. J., Huang J.: Graphene oxide: Surface activity and two-dimensional assembly. *Advanced Materials*, **22**, 1954–1958 (2010). DOI: [10.1002/adma.200903932](https://doi.org/10.1002/adma.200903932)
- [8] Kim J., Cote L. J., Kim F., Yuan W., Shull K. R., Huang J.: Graphene oxide sheets at interfaces. *Journal of the American Chemical Society*, **132**, 8180–8186 (2010). DOI: [10.1021/ja102777p](https://doi.org/10.1021/ja102777p)
- [9] Fang M., Wang K., Lu H., Yang Y., Nutt S.: Covalent polymer functionalization of graphene nanosheets and mechanical properties of composites. *Journal of Materials Chemistry*, **19**, 7098–7105 (2009). DOI: [10.1039/B908220D](https://doi.org/10.1039/B908220D)
- [10] Kou L., Gao C.: Making silica nanoparticle-covered graphene oxide nanohybrids as general building blocks for large-area superhydrophilic coatings. *Nanoscale*, **3**, 519–528 (2011). DOI: [10.1039/c0nr00609b](https://doi.org/10.1039/c0nr00609b)
- [11] Li N., Liu G., Zhen C., Li F., Zhang L., Cheng H-M.: Battery performance and photocatalytic activity of mesoporous anatase TiO₂ nanospheres/graphene composites by template-free self-assembly. *Advanced Functional Materials*, **21**, 1717–1722 (2011). DOI: [10.1002/adfm.201002295](https://doi.org/10.1002/adfm.201002295)
- [12] Yang S., Feng X., Ivanovici S., Müllen K.: Fabrication of graphene-encapsulated oxide nanoparticles: Towards high-performance anode materials for lithium storage. *Angewandte Chemie International Edition*, **49**, 8408–8411 (2010). DOI: [10.1002/anie.201003485](https://doi.org/10.1002/anie.201003485)
- [13] Lovinger A.: Ferroelectric polymers. *Science*, **220**, 1115–1121 (1983). DOI: [10.1126/science.220.4602.1115](https://doi.org/10.1126/science.220.4602.1115)
- [14] Wang M., Shi J-H., Pramoda K. P., Goh S. H.: Microstructure, crystallization and dynamic mechanical behaviour of poly(vinylidene fluoride) composites containing poly(methyl methacrylate)-grafted multi-walled carbon nanotubes. *Nanotechnology*, **18**, 235701/1–235701/7 (2007). DOI: [10.1088/0957-4484/18/23/235701](https://doi.org/10.1088/0957-4484/18/23/235701)
- [15] Yee W. A., Kotaki M., Liu Y., Lu X.: Morphology, polymorphism behavior and molecular orientation of electrospun poly(vinylidene fluoride) fibers. *Polymer*, **48**, 512–521 (2007). DOI: [10.1016/j.polymer.2006.11.036](https://doi.org/10.1016/j.polymer.2006.11.036)
- [16] Casciola M., Capitani D., Donnadio A., Diosono V., Piaggio P., Pica M.: Polyvinylidene fluoride/zirconium phosphate sulfophenylphosphonate nanocomposite films: Microstructure and mechanical properties. *Journal of Materials Chemistry*, **18**, 4291–4296 (2008). DOI: [10.1039/B807948J](https://doi.org/10.1039/B807948J)
- [17] Chen D., Wang M., Zhang W-D., Liu T.: Preparation and characterization of poly(vinylidene fluoride) nanocomposites containing multiwalled carbon nanotubes. *Journal of Applied Polymer Science*, **113**, 644–650 (2009). DOI: [10.1002/app.29311](https://doi.org/10.1002/app.29311)
- [18] Shah D., Maiti P., Gunn E., Schmidt D. F., Jiang D. D., Batt C. A., Giannelis E. P.: Dramatic enhancements in toughness of polyvinylidene fluoride nanocomposites via nanoclay-directed crystal structure and morphology. *Advanced Materials*, **16**, 1173–1177 (2004). DOI: [10.1002/adma.200306355](https://doi.org/10.1002/adma.200306355)

- [19] Tran M. Q., Shaffer M. S. P., Bismarck A.: Manufacturing carbon nanotube/PVDF nanocomposite powders. *Macromolecular Materials and Engineering*, **293**, 188–193 (2008).
DOI: [10.1002/mame.200700340](https://doi.org/10.1002/mame.200700340)
- [20] Kim J-W., Cho W-J., Ha C-S.: Morphology, crystalline structure, and properties of poly(vinylidene fluoride)/silica hybrid composites. *Journal of Polymer Science Part B: Polymer Physics*, **40**, 19–30 (2002).
DOI: [10.1002/polb.10071](https://doi.org/10.1002/polb.10071)
- [21] Hummers W. S., Offeman R. E.: Preparation of graphitic oxide. *Journal of the American Chemical Society*, **80**, 1339 (1958).
DOI: [10.1021/ja01539a017](https://doi.org/10.1021/ja01539a017)
- [22] Hong J., Char K., Kim B-S.: Hollow capsules of reduced graphene oxide nanosheets assembled on a sacrificial colloidal particle. *The Journal of Physical Chemistry Letters*, **1**, 3442–3445 (2010).
DOI: [10.1021/jz101441a](https://doi.org/10.1021/jz101441a)
- [23] Ma W., Wang X., Zhang J.: Effect of MMT, SiO₂, CaCO₃, and PTFE nanoparticles on the morphology and crystallization of poly(vinylidene fluoride). *Journal of Polymer Science Part B: Polymer Physics*, **48**, 2154–2164 (2010).
DOI: [10.1002/polb.22097](https://doi.org/10.1002/polb.22097)
- [24] Rourke J. P., Pandey P. A., Moore J. J., Bates M., Kinloch I. A., Young R. J., Wilson N. R.: The real graphene oxide revealed: Stripping the oxidative debris from the graphene-like sheets. *Angewandte Chemie*, **123**, 3231–3235 (2011).
DOI: [10.1002/anie.201007520](https://doi.org/10.1002/anie.201007520)

Synthesis and thermal degradation characterization of novel poly(phosphazene-aryl amides)

Z. P. Zhao, Q. Guo*, X. Li, J. L. Sun, Z. J. Nie

School of Materials Science and Engineering, Shanghai University, Shanghai 201800, China

Received 18 August 2011; accepted in revised form 1 November 2011

Abstract. New fully aromatic poly(phosphazene-aryl amides) were prepared by polycondensation reaction of our synthesized aromatic diamine: 1,1,3,5-tetraphenoxy-4,6-bis(4-aminophenoxy)oligocyclotriphosphazene (monomer **1**) with terephthaloyl dichloride. Their chemical structure and composition were characterized by elemental analysis, ^1H and ^{31}P NMR (Nuclear Magnetic Resonance), and FT-IR (Fourier transform infrared) spectroscopy, whereas their thermal degradation properties were determined by DSC (Differential Scanning Calorimetry) and TGA (Thermal Gravimetric Analysis) techniques. The solid residues of all samples were analysed by FT-IR and SEM (Scanning Electron Microscopy). Compared to conventional PPTA (poly(p-phenylene terephthamide)), PPAA (poly(phosphazene-aryl amide)) shows excellent thermal stability and solubility in polar protic solvents. All poly(phosphazene-aryl amides) show two thermal degradation in the temperature range 150–600°C. The monomer **1**, due to its structure, shows the first maximum rate of thermal decomposition temperature around 150–350°C, which may be due to the decomposition of the P–O–C bond. Morphology of the solid residues by Scanning Electron Microscope exhibit that the granular of the solid residues gradual disappearance with the increase of monomer **1** content. The surface layer of PPAA solid residues has been gummy, for the syneresis of P–O–P took place.

Keywords: polymer composites, phosphazene, polyamide, thermal degradation

1. Introduction

Polyamides are considered to be high-performance organic materials due to their outstanding thermal and mechanical properties [1–3]. Their properties arise from their aromatic structure and amide linkages. However, the poor solubility, high softening and melting temperatures caused by high crystallinity and high stiffness of polymer backbone hamper the processing of aromatic polyamides. What's more, the properties can be easily tailored through changing their molecular chain structure [4–6]. The strategies which have been employed for solubility increase in aromatic polyamides are lateral substitution and the distortion of the rigid character introducing non-planar, kinked or flexible parts in the main chain. Research efforts are there-

fore underway to take advantage of their properties, enhance their machinability, solubility and incorporate new chemical functionalities in the polyamide backbone or lateral structure, so that their applicability is expanded and remains on the forefront of scientific research [7–9].

Vapor phase lubrication has been proposed as a scheme for lubrication of high efficiency engines operating at temperature outside the range in which any fluid lubricants can be used [10–16]. These applications include gas-turbines which operate with bearing temperatures in excess of 500°C. The most commonly used vapor phase lubricants for these applications are the aryl phosphates and in particular tricresyl phosphate [17].

*Corresponding author, e-mail: guoq@shu.edu.cn

© BME-PT

In our research, we decide to synthesize a new aromatic phosphazene diamine monomer **1** and use it for the synthesis of new fully aromatic poly(phosphazene-aryl amides), in order to investigate their thermal behavior. These data will be fundamental for the following syntheses of known and commercial polyamides containing different mol% of monomer **1**. Also its will be used as the addition-type monomers selected on the basis of the tri-bopolymerization concept in Vapor phase lubrication study. Thus, in the present work we report the synthesis and characterization either of the monomer **1** and their fully aromatic polyamides. Their physical chemistry properties including intrinsic viscosity, solubility behavior, crystallization behavior, thermal properties and degradation behavior are studied.

2. Experimental

2.1. Materials

Hexachlorocyclotriphosphazene (HCCP, self-made) was purified by recrystallization from dry n-heptane and subsequent sublimation twice [18]. 4, 4-diaminodiphenyl ether (ODA) was used as received from Sinopharm Chemical Regents Co. Ltd (99%, Shanghai, China). Phenol was recrystallized from pentane. Tetrahydrofuran (THF) was dried over and distilled from sodium/benzophenone. Triethylamine (TEA) was distilled onto molecular sieves. N-methyl-2-pyrrolidinone (NMP) was dried over phosphorous pentoxide and distilled under reduced pressure. Terephthaloyl chloride (TPC) was purified by recrystallization form anhydrous hexane. p-Phenylenediamine (PPD) was purified by vacuum distillation. Lithium chloride (LiCl) was dried for 8 h at 170 under vacuum. All chemicals and solvents were provided commercially by Sinopharm Chemical Regents Co. Ltd (China) and used without further purification unless otherwise noted. All glassware was dried in an oven under vacuum before use.

2.2. Synthesis of 1,1,3,5-tetraphenoxy-4,6-bis(4-aminophenoxy)oligocyclotriphosphazene (monomer **1**)

The preparation of monomer **1** involved two steps: In the first step, NaH (9.6 g, 0.40 mol) was dissolved in 20 ml THF under stirring and nitrogen atmosphere. To this, a solution of THF (50 ml) dis-

solving phenol (37.65 g, 0.40 mol) was added dropwise. The temperature of reaction mixture was maintained at room temperature for 2 hours and then added this solution dropwise to a solution of HCCP (34.8 g, 0.10 mol) in 100 ml of THF at room temperature for 24 hours. Then, after THF removed by rotary evaporation, the reaction mixture was to be purified by ethanol and deionized water three times. Finally, the product **I** (bis-chlorinetetraphenoxycyclotriphosphazene) was dried under vacuum at 60 C for 12 h. In the second step, a solution of the product **I** (45.25 g, 0.050 mol) in 100 ml of THF was added dropwise to a solution of ODA (20 g, 0.10 mol) and TEA (10.05 g, 0.10 mol) in 100 ml of THF at room temperature. After completion of the addition in 2 h, the mixture was stirred and refluxed at 40°C for 12 h. Then, the reaction mixture was cooled to room temperature. THF was removed by distillation under reduced pressure. The residue was washed with methanol and deionized water three times, and then dried over anhydrous magnesium sulfate. Finally, the product **II** (monomer **1**) was dried under vacuum at 60°C.

FTIR [cm^{-1}]: 3325 ($\nu_{\text{N-H}}$), 1580 (ν_{Ph}), 1160 ($\nu_{\text{C-O-C}}$), 1230 ($\nu_{\text{P=N}}$), 940 ($\nu_{\text{P-O-Ph}}$), 875 ($\nu_{\text{P-N}}$). ^1H NMR (DMSO; δ , ppm): 7.65–7.96 (d, C_6H_4 in ODA), 6.88–7.21 (t, C_6H_5 in phenoxy), 5.91 (s, NH_2), 3.04 (s, NH). ^{31}P NMR (DMSO; δ , ppm): 7.96 (PPh(ODA)), 5.64 (PPh₂).

2.3. Synthesis of

poly(phosphazene-aryl amides)

In a typical experiment, polyamide PPAA, which derived from monomer **1** and TPC, was prepared as follows: A two-necked flask equipped with a dropping funnel and gas inlet tube was charged with a solution of monomer **1** (9.21 g, 0.01 mol) and pyridine (1.55 g) in 20 ml of NMP, to which TPC (2.04 g, 0.01 mol) was added with stirring under N_2 . The mixture was firstly stirred at 0°C for 0.5 h, then at room temperature for 7 h to yield a viscous polyamide solution. Then the solution was trickled into excess ethanol with stirring to afford a precipitate. The precipitate was filtered, washed with hot ethanol for three times, purified by Soxhlet extractor (Acetone as solvent) for 12 h, then washed three times with deionized water and dried at 120°C under vacuum for 6 h to give polyamide PPAA (yield: 88.2%). Other polyamides, PPTA (yield: 93.4%),

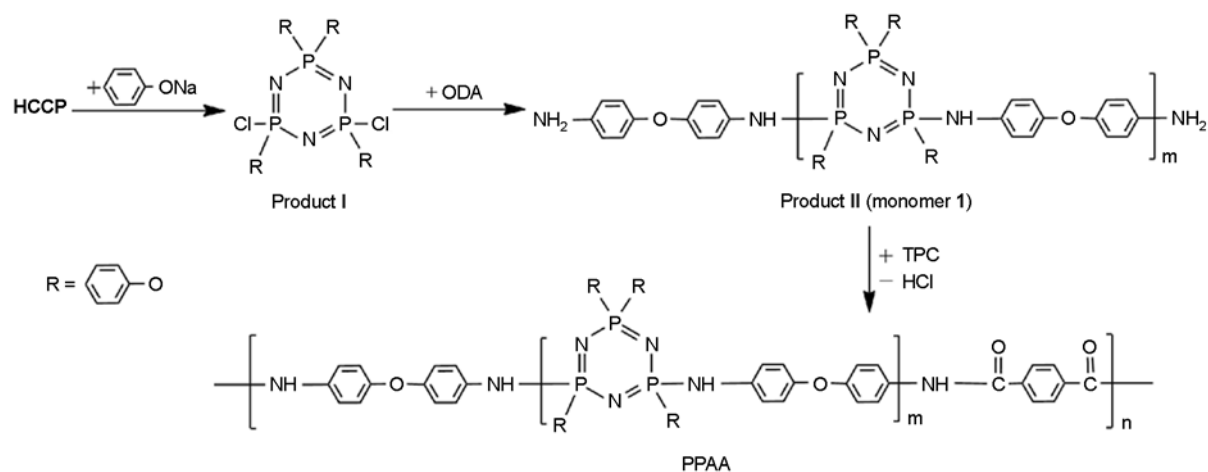


Figure 1. Synthesis of monomer 1 and poly(phosphazene-aryl amides)

Table 1. The chemical compositions of polyamides

Polymer code	PPD [molar percent]	Monomer 1 [molar percent]	TPC [molar percent]
PPTA	100	0	100
PA-7030	70	30	100
PA-5050	50	50	100
PA-3070	30	70	100
PPAA	0	100	100

PA-7030 (yield: 89.2%), PA-5050 (yield: 91.6%), PA-3070 (yield: 88.7%), were synthesized by similar procedure. The chemical compositions of the polyamides are listed in Table 1. All composites described were synthesized by similar methods as Figure 1.

2.4. Measurements

FT-IR spectra of all samples were recorded using polymer granule on a Perkin-Elmer Wellesley MA spectrophotometer. The (^1H and ^{31}P) NMR spectra were recorded on a Varian DRX 400 NMR spectrometer (Varian NMR Instruments) with the operating frequency at 400 MHz using CDCl_3 or DMSO as a solvent, using TMS as inner reference and H_3PO_4 (85%) as external reference. Elemental analysis was carried out using a Heraeus CHN-O rapid elemental analyzer (United States) with acetanilide as a standard. The intrinsic viscosities of polyamides were measured at a concentration of 0.5 g/dl in concentrated sulfuric acid, at 30 ± 0.2 . The numbers were counted by measured value from suspended level Ubbelohde viscometer. Gel permeation chromatographic analysis (GPC) was carried out on a PL GPC 50 plus evaporative mass detector instrument

(United States). Dimethylformamide (DMF) was used as mobile phase after calibration with polystyrene standards of known molecular weights. Thermogravimetric analysis (TGA) was performed on a TGA 7 instrument (PerkinElmer) thermal analysis system. Sample weight taken was 2–4 mg. DSC analysis was carried out on a Perkin-Elmer Pyris 2 DSC analyzer (PerkinElmer), at a heating rate of $10^\circ\text{C}/\text{min}$ in nitrogen atmosphere. Sample weight taken was 15–20 mg. Wide-angle X-ray scattering measurements were performed on a Bruker AXS-D8 Avance X-ray diffractometer (Germany) with a copper target (40 kV, 15 mA). The microstructures of solid residues were recorded using a Cambridge S250MK3 scanning electron microscope (U.K.). The solid residue of the samples degraded to various extents was also prepared using the TGA instrument under nitrogen atmosphere. The materials were heated from room temperature to 600°C with a heating rate of $20^\circ\text{C}/\text{min}$, and then rapidly cooling the residue to room temperature.

3. Results and discussion

3.1. Synthesis and characterization of monomer 1 and poly(phosphazene-aryl amides)

The main objective of this study is to produce novel polyamide with high residual rate (upon 50% at 600°C), improved solubility and processability without too much sacrificing of their thermal and mechanical properties. The polyamide yields a high char residue at 600°C and contains plenty of phosphorus element which can be used as surface chemical promoter to achieve good lubricity effect. Cyclic phos-

phazenes are found with both planar and puckered phosphorus-nitrogen rings. The length of a phosphorus-nitrogen single bond in cyclophosphazene is in the range of 1.47–1.62 Å, and this due to an appreciable contraction. The shortest skeletal bonds are associated with highly electronegative substituents. σ and σ - π bonds are observed in the neutral system. These heterocycles have polar groups, imparting an additional dipole moment to the molecule, and hence they can interact with each other and alter the properties of the polymers containing these groups. So in order to examine the presence of cyclophosphazene groups in the polyamides backbone, aromatic diamine containing phosphazene groups and poly(phosphazene-aryl amides) were synthesized. Benzene rings were also introduced in the chain in order to render high thermal stability and other properties. The monomer **1**, which is a new phosphazene aromatic diamine, was synthesized according to Figure 1 through a two-step route by nucleophilic substitution reaction. The nucleophile aromatic substitution for chlorine reaction is a moderate synthesis reaction. On the basis of the results found in the synthesis of the amide model compounds above described, the novel poly(phosphazene-aryl amides) were prepared by solution polycondensation reaction. This synthetic route though it might lead to low molecular weight materials, represents a clean and bland pathway which allows for the control of the chemistry involved.

The chemical structures of the polyphosphazene-containing oligomer synthesized in the study were characterized by elemental analysis, ^1H NMR, ^{31}P NMR and FT-IR spectroscopy. The calculated elemental contents of monomer **1** in terms of the formula ($\text{C}_{48}\text{H}_{42}\text{N}_7\text{O}_6\text{P}_3$) were C 63.65; H 4.64; N 10.83; O 10.61; P 10.27; and the analyzed data show that C, H, N, O and P are 63.41, 4.82, 10.69, 10.57 and 10.33, respectively. It is found that elemental analysis of the synthesized monomer **1** is in good agreement with the calculated values. The ^{31}P NMR spectrum of monomer **1** recorded at room temperature in DMSO, shows two intense peaks ($\delta = 5.64$ ppm, for the phenol groups linked to the phosphorus atoms; $\delta = 7.96$ ppm, for the phenylamino groups linked to the phosphorus atoms). This experimental evidence denotes that the Chlorine was completely replaced by two groups. Furthermore, in the ^1H NMR spectrum of monomer **1**,

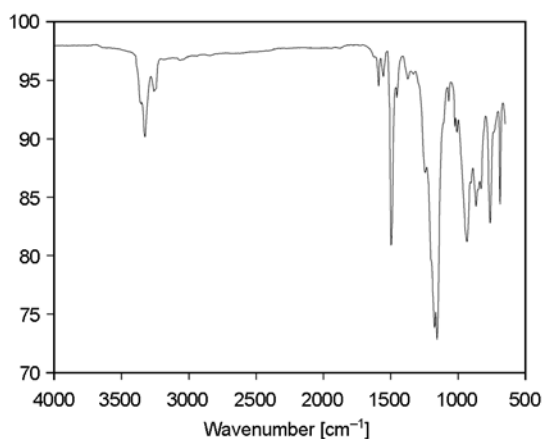


Figure 2. FT-IR spectrum of monomer **1**

the chemical shifts corresponding to the phenol ring are found at $\delta = 6.89$ ppm and $\delta = 7.21$ ppm; $\delta = 3.04$ ppm and $\delta = 2.97$ ppm, as the two doublets prove the presence of the phenylamino groups.

In order to obtain a more complete and reliable chemical characterization, the synthesized monomer **1**, was also investigated by FT-IR technique. The spectrum is shown in Figure 2. The monomer shows a strong absorption band at 1230 cm^{-1} due to the P=N stretch, while the absorption band at 875 cm^{-1} due to the P–N stretch. The broad band at 1490 and 1580 cm^{-1} corresponds to the benzene ring in AOPP. It also shows strong absorption peaks at 1050 cm^{-1} , at 940 and 3320 cm^{-1} due to the C–O–C stretch, P–O–Ar stretch and N–H stretching, respectively.

The FT-IR spectra of the poly(phosphazene-aryl amides) shown in Figure 3 present the characteristic absorption bands due to eh stretching of the –NH–amide groups along the chain in the range 3000 – 3500 cm^{-1} , while the stretching of the polyphosp-

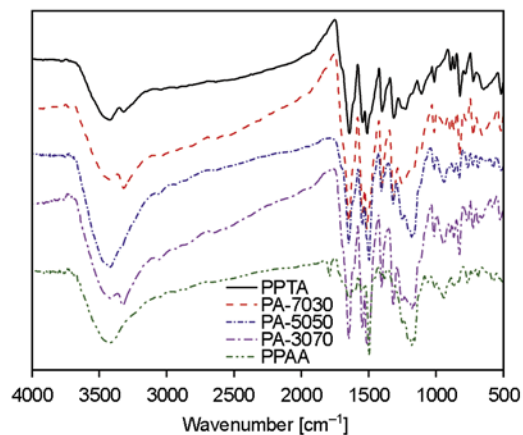


Figure 3. FT-IR spectrum of the poly(phosphazene-aryl amides)

hazene groups give a wide band at 1200 cm^{-1} . Characteristic bands due to the aromatic polyamides were observed, for example, at 1655 cm^{-1} [amide I (C=O stretching mode)] and 1530 cm^{-1} [amide II (coupling of C–N stretching and N–H in-plane bending modes)]. Very similar FT-IR spectra were achieved for fully aromatic polyphosphazene polyamides (Table 1).

In conclusions, the inspection reveals that the novel poly(phosphazene-aryl amides) synthesized and discussed in the present work can be well characterized and distinguished applying these powerful methods.

3.2. Solubility and Intrinsic viscosity of the poly(phosphazene-aryl amide)

The solubility of the fully aromatic poly(phosphazene-aryl amide) was tested in various solvents at 1 wt% concentration and the results are summarized in Table 2.

The new polyamide (PPAA) was readily soluble in highly polar solvents such as DMF, DMAc, DMSO and NMP at room temperature or upon heating. The high-solubility nature of PPAA can be explained by the presence of polypolyphosphazene groups. Because of these voluminous groups, the packing of the polymer chains in tight structures through hydrogen bonding between amide groups is prevented and, consequently, the solvent molecules can easily diffuse into the polymer chain. The increased solubility of these polyamides is mainly due to their amorphous character. And the solubility of the materials is similar to those of conventional maramids. All the X-ray diffraction diagrams of polyamides gave predominately amorphous patterns (Figure 4). The stereo structure of PPAA is shown in Figure 4.

In order to estimate the molecular weights of the polyamide products, their intrinsic viscosities (η_{inh}) were measured using an Ubbelohde viscometer

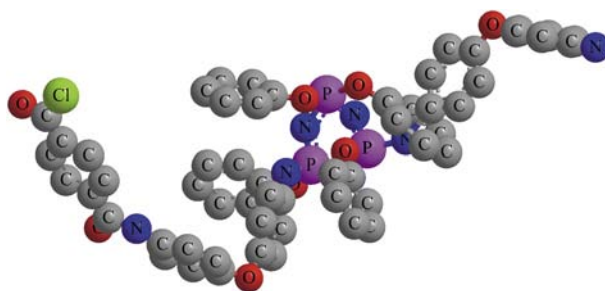


Figure 4. Model of a macromolecule fragment incorporating 1 repeating units of PPAA

Table 3. Inherent viscosity (η_{inh}) and GPC value of polyamides

Polymer code	$\eta_{\text{inh}}^1 \cdot [\text{dl} \cdot \text{g}^{-1}]$	$M_w^2 \cdot [\text{g} \cdot \text{mol}^{-1}]$	PD
PPTA	3.16	–	–
PA-7030	2.31	–	–
PA-5050	1.62	–	–
PA -3070	0.98	–	–
PPAA	0.75	38 300	1.78

¹Inherent viscosity measured at a concentration of 0.5 g/dl in concentrated sulfuric acid, at $30 \pm 0.2^\circ\text{C}$.

²Measured by GPC in DMF; polystyrene was used as standard.

with concentrated sulfuric acid at $30 \pm 0.2^\circ\text{C}$. Meanwhile, the weight-average molecular weights (M_w) and polydispersities PD ($= M_w/M_n$) of the polyamide was estimated by GPC measurements in DMF. The values are all listed in Table 3. The testing data indicate that the polymers have quite a narrow molecular weight distribution and a low quantity of oligomers.

3.3. Crystallinity of our synthesized poly(phosphazene-aryl amides)

In order to study the crystalline or amorphous nature of the polyamides, WAXD measurements at room temperature were performed. Typical wide-angle X-ray diffractograms of the powder polyamides are illustrated in Figure 5. The powder samples were pulps which obtained after precipitation from solution (synthesis), without through spinning and fiber processing processes. From the curves we can see

Table 2. Solubility behaviour¹ of the polyamides in various solvents²

Polymer code	CHCl_3	THF	DMF	DMAc	NMP	DMSO	H_2SO_4
PPTA	–	–	–	–	–	–	+
PA-7030	–	–	–	–	–	–	+
PA-5050	–	–	–	–	–	±	+
PA -3070	–	–	±	±	±	±	+
PPAA	–	–	±	±	+	+	+

¹Solubility: (+) soluble at room temperature; (±) soluble with warming or swollen; (–) insoluble.

²THF: tetrahydrofuran; DMF: *N,N*-dimethyl formamide; DMAc: *N,N*-dimethyl acetamide; NMP: *N*-methyl pyrrolidone; DMSO: dimethyl sulfoxide.

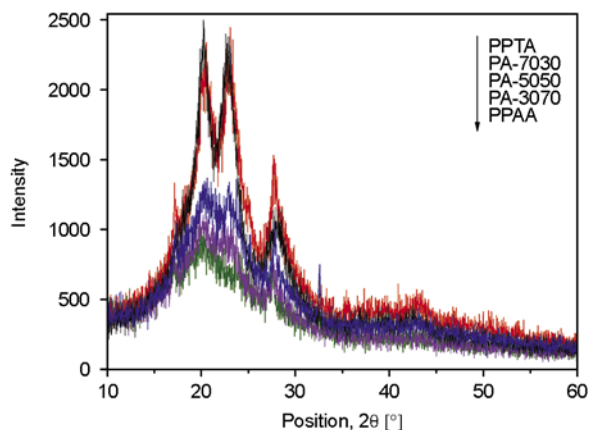


Figure 5. XRD patterns of the polyamides

that there are two dispersion peaks at $2\theta = 20.5$ and 23.5° for PPTA, which indicates PPTA has low crystallinity. But, there are no sharp peaks in the PPAA. It proves that PPAA is amorphous. This can be attributable to the introduction of polyphosphazene groups, which weakens the regular structure of molecular chains, reduces the rigidity and therefore disrupts the crystallization capacity of the polyamides. Thus, the amorphous structure of this polyamide also reflected in its excellent solubility as can be observed in Table 2.

3.4. Thermal properties of the polyamides

The thermal properties and stability of all poly (phosphazene-aryl amides) were studied by DSC and TGA techniques, respectively, and the data are reported in Table 4. As can be observed, in Table 2 the poly(phosphazene-aryl amides) are amorphous samples with a glass transition (T_g) of 85°C . For the compounds PA-7030, PA-5050 and PA-3070 we expect a high T_g values similar to PPTA, which have a T_g values higher than 120°C . And the T_g values decreased with decreasing rigidity and symme-

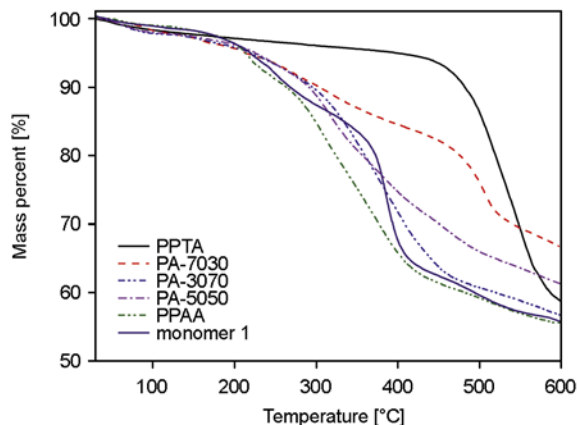


Figure 6. TGA curves for the polyamides

try of the polymer backbone, which is due to the increase of monomer 1 content.

The thermal stabilities of the poly(phosphazene-aryl amides) were evaluated by TGA at $20^\circ\text{C}/\text{min}$ up to 600°C under nitrogen. Figure 6 shows a typical temperature dependence profile of the polyamides weight loss. The PPTA sample presents a maximum rate of the thermal decomposition temperature at 512°C , yielding a char residue of 58.68% at 600°C , while a char residue of 55.58% at 600°C was observed in the thermal decomposition of the PPAA, of 66.55% for the PA-7030, of 61.27% for the PA-5050, and of 56.56% for the PA-3070. The two decomposition steps for PPAA occur at 180.7°C and 271.5°C , respectively. The weight loss of PPTA at around 100 – 150°C is due to the evaporation of absorbed moisture. The PPAA loss 7% of the sample in the temperature range 150 – 250°C , and another 35.42% in the range 250 – 600°C . PPTA sample loss 35.32% of the sample in temperature range 455 – 600°C . Comparing the curves in Figure 5, it emerges that the first decomposition step of the monomer 1 occurs around 150 – 350°C . This is attributed to the less stable of the P–O–C bone linkage, as reported for other polymeric systems containing similar polyphosphazene groups [19, 20]. It also determines the lower thermal stability of the fully aromatic polyphosphazene polyamides with respect to their no-polyphosphazene samples.

A pleasant surprise from the curves, we can confirm that PA-3070 and PA-5050 show higher char yields than PPTA. It can be readily attributed to the inherent thermal-stability properties of the polyphosphazene cores. With the presence of a small amount of polyphosphazene diamine, cross-linking and gela-

Table 4. Data results for the polyamides

Code	T_0 [°C] ¹	T_{10} [°C] ²	Char yield [%] ³	T_g [°C] ⁴
PPTA	455.3	482.8	58.68	341
PA-7030	237.8	308.6	66.55	195
PA-5050	198.6	298.7	61.27	157
PA-3070	193.1	291.0	56.56	146
PPAA	180.7	263.4	55.58	85

¹Initial decomposition temperature recorded by TGA at a heating rate of $20^\circ\text{C}/\text{min}$ in N_2 .

²Temperature at which 10% weight loss is observed.

³Anaerobic residual weight at 600°C .

⁴Glass transition temperature measured on DSC at a heating rate of $10^\circ\text{C}/\text{min}$ in N_2 .

tion occurs in the decomposition. As the network structure and gelation can inhibit the production of small molecules, the higher char yield is an effect of achieving synergy between the individual units.

3.5. Thermal degradation properties

The TGA results indicated that polyphosphazenes play an important role in increasing the thermal stability of poly(phosphazene-aryl amides) at elevated temperatures. However, its stability at lower temperatures decreases. To further investigate their influence, the residues of the polyamides samples obtained from the TGA measurements, from room temperature to 600°C with a heating rate of 20°C/min in air, were analyzed by FT-IR and SEM. Figure 7 illustrates the FT-IR spectra of the pyrolysis residues. In the FT-IR spectra of poly(phosphazene-aryl amides) samples, the absorption peak at 940 cm⁻¹ due to P–O–C bond and the absorption peak at 1500 cm⁻¹ due to N–H bending and C–N stretching disappear. The characteristic absorption peaks for P=N at about 1230 cm⁻¹, P–N at 875 cm⁻¹ and for ether group at 1180 also disappear. However, a few new peaks appear at 1056 cm⁻¹, which might be ascribed to the generation of P–O–P. Similar to the mechanism which has been reported [20, 21]. The obtained structure could act as an acid catalyst, accelerating the cleavage of side groups and the breaking of ether groups in poly(phosphazene-aryl amides). Then, the polyamides react to form more stable structures. The appearance of P–O–P group is considered as crosslinking to different species, resulting in the formation of complex phosphorus structures. This is why the thermal degradation of the poly(phosphazene-aryl amides) is much slower than PPTA at above 500°C. The morphology of the solid residues was observed by Scanning Electron Microscope (Figure 8). The surface of monomer **1** (Figure 8f) residues exhibits a porous texture reverse to the lump of PPTA (Figure 8a). Comparing with the pictures (Figure 8), we can see that the granular of the solid residues gradual disappearance with the increase of monomer **1** content. The surface layer of PPAA solid residues has been grumous, for the syneresis of P–O–P took place. It proves that the cyclotriphosphazene moieties produce phosphoric acid or metaphosphoric acid during pyrolysis which acts in the condensed phase promoting char formation on the surface.

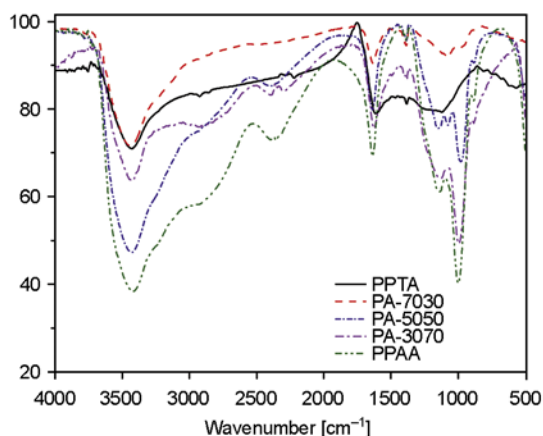


Figure 7. FT-IR curves for the solid residues of poly(phosphazene-aryl amides) after pyrolysis

3.6. LOI values of poly(phosphazene-aryl amides)

Char yield can be applied as decisive factor for estimating limiting oxygen index (LOI) of the polymers based on Van Krevelen and Hoftyzer equation [22] (Equation (1)):

$$\text{LOI} = 17.5 + 0.4\text{CR} \quad (1)$$

where CR – Char yield (the data are reported in Table 2). Thus, the LOI values are speculated from TGA data, not experimental burning data.

The values of LOI are plotted in Figure 9. The average values of LOI for the two polyamides are represented by the dotted lines connecting the points for the two pure components (PPTA and PPAA). The poly(phosphazene-aryl amides) had LOI values calculated derived from their char yield was high than 39. On the basis of LOI values, such macromolecules can be classified as self-extinguishing polymers.

4. Conclusions

New kinds of poly(phosphazene-aryl amides) were prepared by polycondensation in solution of the our synthesized monomer **1** with terephthaloyl dichloride. The monomer **1** was characterized by elemental analysis, ¹H NMR, ³¹P NMR and FT-IR techniques to verify its chemical structure. The results confirm this successful synthesis. The investigation on thermal properties shows that the thermal stability of our synthesized fully aromatic polyphosphazene polyamides are strong determined by the presence of the polyphosphazene groups in the

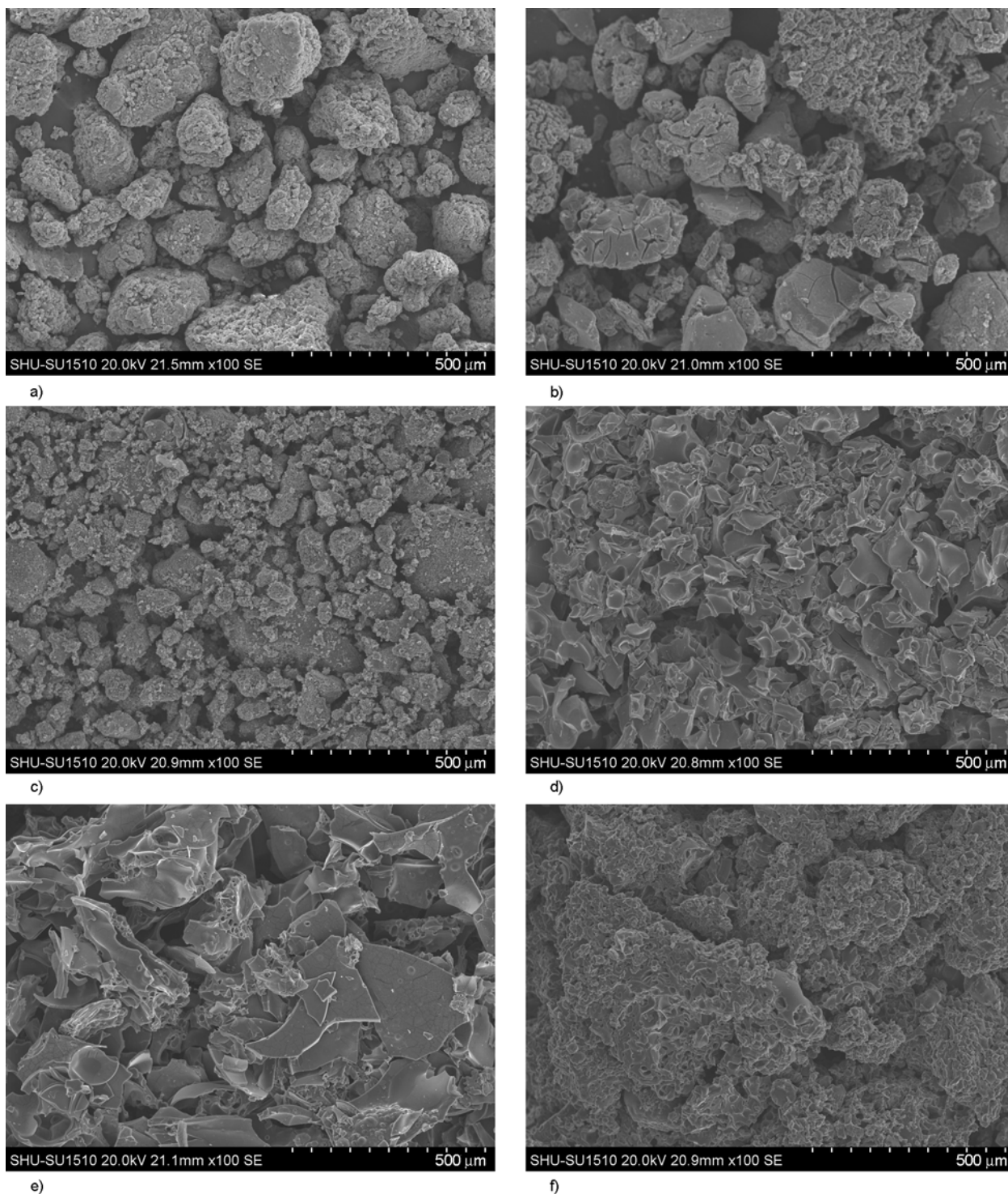


Figure 8. Morphology of the solid residues of the composites after pyrolysis: (a) PPTA, (b) PA-7030, (c) PA-5050, (d) PA-3070, (e) PPAA, (f) monomer **1**

polymer chains. They thermally degradation in two steps, and this behavior may be due to the decomposition of the P–O–C bone and aromatic bones. The surface of monomer **1** solid residues exhibits a porous texture with the scanning electron micro-

scope. During pyrolysis, polyphosphazene not only acted in the condensed phase to promote char formation at the surface but also promoted gelation to restrain pyrolysis indirectly.

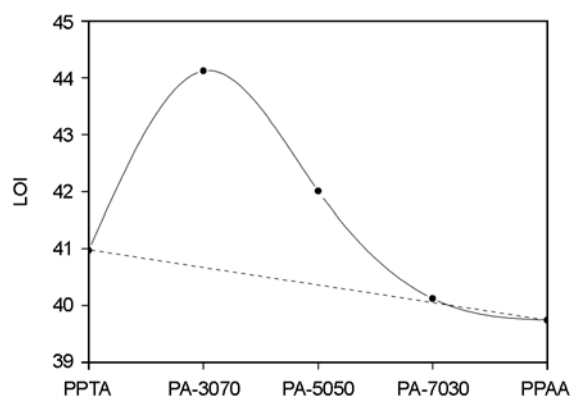


Figure 9. LOI values of poly(phosphazene-aryl amides)

Acknowledgements

We are thankful to the National Natural Science Foundation of China (Fund No. 50975167) and Shanghai Leading Academic Discipline Project (Project Number: S30107) for the continuing support to this research.

References

- [1] García J. M., García F. C., Serna F., de la Peña J. L.: High-performance aromatic polyamides. *Progress in Polymer Science*, **35**, 623–686 (2010). DOI: [10.1016/j.progpolymsci.2009.09.002](https://doi.org/10.1016/j.progpolymsci.2009.09.002)
- [2] Quadrini F., Squeo E. A., Tagliaferri V.: Machining of glass fiber reinforced polyamide. *Express Polymer Letters*, **1**, 810–816 (2007). DOI: [10.3144/expresspolymlett.2007.112](https://doi.org/10.3144/expresspolymlett.2007.112)
- [3] Yagci H., Mathias L. J.: Synthesis and characterization of aromatic polyamides and polyimides from trimethyl- and di-*t*-butylhydroquinone-based ether-linked diamines. *Polymer*, **39**, 3779–3786 (1998). DOI: [10.1016/S0032-3861\(97\)10378-0](https://doi.org/10.1016/S0032-3861(97)10378-0)
- [4] Meléndez A., de la Campa J. G., de Abajo J.: Polyisophthalamides with phenoxy pendant groups. *Polymer*, **29**, 1142–1145 (1988). DOI: [10.1016/0032-3861\(88\)90030-4](https://doi.org/10.1016/0032-3861(88)90030-4)
- [5] Sava I., Iosip M-D., Bruma M., Hamciuc C., Robison J., Okrasa L., Pakula T.: Aromatic polyamides with pendent acetoxybenzamide groups and thin films made therefrom. *European Polymer Journal*, **39**, 725–738 (2003). DOI: [10.1016/S0014-3057\(02\)00295-1](https://doi.org/10.1016/S0014-3057(02)00295-1)
- [6] Tamami B., Yeganeh H.: Synthesis and properties of novel aromatic polyamides based on 4-aryl-2,6-bis(4-chlorocarbonylphenyl) pyridines. *European Polymer Journal*, **38**, 933–940 (2002). DOI: [10.1016/S0014-3057\(01\)00264-6](https://doi.org/10.1016/S0014-3057(01)00264-6)
- [7] Wang W-Z., Zhang Y-H.: Environment-friendly synthesis of long chain semiaromatic polyamides. *Express Polymer Letters*, **3**, 470–476 (2009). DOI: [10.3144/expresspolymlett.2009.58](https://doi.org/10.3144/expresspolymlett.2009.58)
- [8] Rao Y., Waddon A. J., Farris R. J.: Structure–property relation in poly(*p*-phenylene terephthalamide) (PPTA) fibers. *Polymer*, **42**, 5937–5940 (2001). DOI: [10.1016/S0032-3861\(00\)00905-8](https://doi.org/10.1016/S0032-3861(00)00905-8)
- [9] Yagci H., Mathias L. J.: Synthesis and characterization of aromatic polyamides and polyimides from trimethyl- and di-*t*-butylhydroquinone-based ether-linked diamines. *Polymer*, **39**, 3779–3786 (1998). DOI: [10.1016/S0032-3861\(97\)10378-0](https://doi.org/10.1016/S0032-3861(97)10378-0)
- [10] Klaus E. E., Li H., Chen C. I., Duda J. L.: Wear as measured with a four-ball wear tester using fully flooded and vapor phase with condensation lubrication methods. *Wear*, **162**, 944–949 (1993). DOI: [10.1016/0043-1648\(93\)90099-8](https://doi.org/10.1016/0043-1648(93)90099-8)
- [11] Argibay N., Keith J. H., Krick B. A., Hahn D. W., Bourne G. R., Sawyer W. G.: High-temperature vapor phase lubrication using carbonaceous gases. *Tribology Letters*, **40**, 3–9 (2010). DOI: [10.1007/s11249-009-9514-7](https://doi.org/10.1007/s11249-009-9514-7)
- [12] Sung D., Gellman A. J.: The surface chemistry of alkyl and arylphosphate vapor phase lubricants on Fe foil. *Tribology International*, **35**, 579–590 (2002). DOI: [10.1016/S0301-679X\(02\)00045-2](https://doi.org/10.1016/S0301-679X(02)00045-2)
- [13] Abdelmaksoud M., Bender J. W., Krim J.: Nanotribology of a vapor-phase lubricant: A quartz crystal microbalance study of tricresylphosphate (TCP) uptake on iron and chromium. *Tribology Letters*, **13**, 179–186 (2002).
- [14] Jin Y. S., Zhou C. H.: The effectiveness of high temperature lubrication by in situ formation of graphite/MoS₂ films. *Wear*, **205**, 77–87 (1997). DOI: [10.1016/S0043-1648\(96\)07308-5](https://doi.org/10.1016/S0043-1648(96)07308-5)
- [15] Stirniman M. J., Falcone S. J.: The ideality of polydisperse perfluoropolyether lubricants with application to physical vapor deposition. *Tribology Letters*, **8**, 171–177 (2000). DOI: [10.1023/A:1019135218167](https://doi.org/10.1023/A:1019135218167)
- [16] Smith C. J., Furey M. J., Kajdas C.: An exploratory study of vapor-phase lubrication of ceramics by monomers. *Wear*, **181–182**, 581–593 (1995). DOI: [10.1016/0043-1648\(95\)90174-4](https://doi.org/10.1016/0043-1648(95)90174-4)
- [17] Liu W., Klaus E. E., Duda J. L.: Wear behaviour of steel-on-Si₃N₄ and Si₃N₄-on-Si₃N₄ systems with vapor phase lubrication of oleic acid and TCP. *Wear*, **214**, 207–211 (1998). DOI: [10.1016/S0043-1648\(97\)00253-6](https://doi.org/10.1016/S0043-1648(97)00253-6)
- [18] Brandt K., Jekel A. P., Meetama A., Van De Grampel J. C.: Syntheses and structures of precursors in the polycondensation of hexachlorocyclotriphosphazene and hydroquinone. *Inorganica Chimica Acta*, **157**, 251–258 (1989). DOI: [10.1016/S0020-1693\(00\)80549-6](https://doi.org/10.1016/S0020-1693(00)80549-6)
- [19] El Gouri M., El Bachiri A., Hegazi S. E., Rafik M., El Harfi A.: Thermal degradation of a reactive flame retardant based on cyclotriphosphazene and its blend with DGEBA epoxy resin. *Polymer Degradation and Stability*, **94**, 2101–2106 (2009). DOI: [10.1016/j.polymdegradstab.2009.08.009](https://doi.org/10.1016/j.polymdegradstab.2009.08.009)

- [20] Maynard S. J., Sharp T. R., Haw J. F.: Thermal degradation chemistry of poly(diphenoxyphosphazene). *Macromolecules*, **24**, 2794–2799 (1991).
DOI: [10.1021/ma00010a024](https://doi.org/10.1021/ma00010a024)
- [21] Liu R., Wang X.: Synthesis, characterization, thermal properties and flame retardancy of a novel nonflammable phosphazene-based epoxy resin. *Polymer Degradation and Stability*, **94**, 617–624 (2009).
DOI: [10.1016/j.polymdegradstab.2009.01.008](https://doi.org/10.1016/j.polymdegradstab.2009.01.008)
- [22] Van Krevelen D. W., Hoftyzer R. J.: *Properties of polymer*. Elsevier, New York (1976).

Effects of crystalline morphologies on the mechanical properties of carbon fiber reinforcing polymerized cyclic butylene terephthalate composites

T. Yu², C. M. Wu^{1*}, C. Y. Chang¹, C. Y. Wang¹, S. P. Rwei²

¹Department of Fiber and Composite Materials, Feng Chia University, 100, Wenhwa Rd., Taichung, Taiwan 40724, Republic of China

²Department of Molecular Science and Engineering, National Taipei University of Technology, No. 1, Section 3, Chung-Hsiao East Road, Taipei, Taiwan 10608, Republic of China

Received 17 August 2011; accepted in revised form 9 November 2011

Abstract. Carbon/polymerized cyclic butylene terephthalate (pCBT) composites were prepared through a modified film stacking technique. Three crystalline morphologies of carbon/pCBT composites were obtained at different crystallization temperatures. Tensile, flexural, short beam shear and impact tests were conducted. The low crystallinity carbon/pCBT samples were crystallized at 185°C with spherulitic structure which leads to form the large area spherulite/transcrystalline boundary regions. Consequently, the crack initiated and propagated along with ‘weak’ spherulite/transcrystalline boundary regions, which were resulted low mechanical properties. Carbon/pCBT sample crystallized at 210°C with high crystallinity and highly disordered spherulitic crystallites without spherulite/transcrystalline boundary lines or boundary crystals exhibits the highest mechanical properties.

Keywords: mechanical properties, processing technologies, polymer composites, cyclic butylenes terephthalate, spherulite boundary

1. Introduction

Low viscosity cyclic butylene terephthalate (CBT) oligomer is a very promising material for a new generation of thermoplastic and composite applications. CBT easily polymerizes in 3–5 min at 190°C to linear high molecular weight poly (butylene terephthalate) (pCBT) in the presence of tin or titanium catalysts [1, 2]. Recent interest in CBT has not only prompted recycling in an attempt to manage the growing polymer waste problem, but also stimulated the research and development of thermoplastic composites.

CBT possesses important characteristics that are advantageous when processing thermoplastic composites: a water-like, low viscosity; the ability to

rapidly polymerize into pCBT which is transformed from cyclic oligomer into linear, high-molecular weight, engineering thermoplastic; and a polymerization process that is free from low-molecular weight byproducts [3]. Because of the low viscosity characteristic, production techniques typically associated with thermoset composites, such as resin transfer molding (RTM), can be used with minor adaptations to process thermoplastic composites.

CBT polymerization can be performed above and below the melting temperature of the resulting pCBT (~225°C). The outcome of pCBT is practically the same: number average molecular weight varies between 30 and 40 kg/mol, and the polydispersity index remains at approximately 2. The remaining

*Corresponding author, e-mail: cmwu@fcu.edu.tw

oligomer content in the pCBT sample is equivalent to the equilibrium oligomer content in PBT, which is known to be 3–5%. Mohd Ishak *et al.* [4] studied the rheological properties of pCBT and find a drastic reduction of time to complete polymerization when the polymerization temperature is above 200°C. Researchers published differential scanning calorimetry (DSC) studies on the polymerization of CBT as well as studies about the crystallization and melting behavior of the resulting pCBT [4–9]. Tripathy *et al.* [10] studied the polymerization of CBT using different catalysts and discovered that the selected catalyst strongly influences the polymer conversion and the time required for polymerization. A fast catalyst such as stannoxane can complete CBT polymerization within 2–3 min at 190°C, whereas a slow catalyst system like tetrakis-(2-ethylhexyl) titanate required more than 15 min [10]. Different type of catalysts have also significant influence on the molecular weight and therefore on the mechanical properties of the resulted polymer. Investigators regard the polymerization of CBT to be an athermal process because it is an entropically driven, ring-expansion polymerization [6]. Hakmé *et al.* [11] studied the polymerization and crystallization kinetics of CBT through dielectric sensing. They found that the simultaneous polymerization and crystallization (type I) occurred at below 200°C; polymerization followed by crystallization (type II) at above 200°C; and only polymerization (type III) occurred at above 220°C. That is, the crystallization behavior of pCBT was not only affected by the crystallization condition, but also influenced by the polymerization condition. The crystal structure of pCBT is considered to be that same as that of PBT [12]. In contrast to the PBT, however, the lamellae in the pCBT samples are nicely defined, thicker, and well oriented. Additionally, the transition from crystalline to amorphous is more pronounced in the pCBT samples, which might be an indication of a reduction in tie molecules [13]. Our previous study [14, 15] on the isothermal crystallization of pCBT polymerized at 230°C catalogues four morphologic features: usual negative spherulites; unusual spherulites; mixed type birefringence spherulites coexisting with boundary crystals; and highly disordered spherulitic crystals corresponding to the crystallization temperatures. Thus, it can be seen visually that the processing

condition like temperature strongly affects the crystal morphology, and perhaps even the final properties of the polymer and its composites.

As for the application of CBT for continuous fiber-reinforced composites, there are some published works on this subject. Parton and Verpoest *et al.* [3, 12] studied unidirectional glass fiber reinforced pCBT composites using resin transfer molding (RTM) technique. They found that the polymerized CBT was much more brittle than normal PBT due to large and perfect crystals growth, when pCBT has been processed under isothermal RTM processing conditions (polymerization category of type I) [12, 16]. The matrix brittleness weakens the matrix and lowers the transverse strength of the unidirectional composite.

In order to solve this problem, researchers have tried various techniques such as copolymerized CBT with ϵ -caprolactone [17], polycaprolactone (PCL) [15, 18] or polyvinylbutyral [19] blended with organosilicate [8], silica [20] or carbon nanotubes [21–23]. Baets *et al.* [18, 24] reported that the copolymerization of pCBT/PCL hindered the crystallization of pCBT. The pCBT/PCL copolymer creates a much tougher material, whether it is unfilled or a glass fiber reinforced composite.

Mohd Ishak *et al.* [16] prepared woven glass fabric reinforced pCBT composites using a compression mold technique. The results showed that low viscosity CBT facilitates the penetration of the resin through the fabric and also exhibits strong interfacial properties. Mäder *et al.* [25] investigated the interphase between glass fibers and pCBT resins and found that the interfacial bond strength of glass/pCBT composites varied depending on the sizing formulation and properties. A non-isothermal method prepared basalt fiber reinforced pCBT composites was reported [26] and the results found that a fast cooling process led to less perfect crystals in the pCBT matrix and toughened the pCBT composites.

So far glass [3, 16, 18, 24–26], basalt [27] and carbon [28–30] fibers have been used as reinforcement in pCBT composites and evaluated its reinforcing effects by many researcher. However, effects of crystalline morphology on the mechanical properties of the carbon/pCBT composites have not been yet examined. Therefore, we are interested in investigating the effect of the processing conditions on

the crystalline morphology and mechanical properties of the resulting composites. Tensile, flexural, short beam shear and impact testing were employed to evaluate the carbon fiber/pCBT composites.

2. Experimental

2.1. Materials

In this study, CBT pellets (Grade: 160) purchased from Cyclics (Schenectady, NY; USA www.cyclics.com) were used. CBT was produced with an average molecular weight $M_w = (220)_n$ ($n = 2\sim 7$) for the purpose of engineering plastic and composite applications. The CBT polymerizes within the presence of a butyl tin chloride dihydroxide catalyst (Fascat 4101 by Arkema) which is already added to the CBT resin by the manufacture. CBT was dried overnight in an 85°C vacuum oven and kept in a desiccator until further use. 3K carbon fiber (HTA40, Toho Tenax America, USA) in a twill weave was used as a reinforcement.

2.2. Sample preparation

This study used a modified film stacking technique [31] to produce high quality impregnated and void free carbon/pCBT composites. First, the CBT matrix was pressed in a compression mold into a 300 μm thick film with 5 MPa of pressure at 150°C for 1 min. Carbon/pCBT prepreg with an average thickness of 300~350 μm was prepared using the following procedure: A layer of carbon fabric was placed on a CBT thin film and pressed at 150°C under 8 MPa of pressure for 3 min, and then quenched to room temperature. In order to simplify the crystallization process of pCBT, polymerization category of type III samples were polymerized at 230°C for 30 min. to allow complete polymerization without crystallization. The carbon/pCBT composites were prepared by stacking eight layers of prepreg and pressed them at 230°C for 30 min under 12 MPa of pressure to allow for complete polymerization. This was followed by quenching until the desired crystallization temperatures ($T_c = 185, 195, \text{ and } 210^\circ\text{C}$) were reached. Based on crystallization kinetics studies [14], the time for complete crystallization is 20 min for $T_c = 185^\circ\text{C}$, 40 min for $T_c = 195^\circ\text{C}$, and 120 min for $T_c = 210^\circ\text{C}$. The composite samples were then slowly cooled to room temperature and removed from the mold. The fiber volume fractions of the carbon/pCBT composites were determined

by burning test method according to ASTM D3171. The void fractions of the carbon/pCBT composites were determined according to ASTM D2734. The resulted fiber volume fraction and void fraction were 51.4 ± 0.7 and $0.4\pm 0.2\%$, respectively.

2.3. Experimental methods

2.3.1. Molecular weight and polydispersity index

Gel permeation chromatography (GPC) was used to determine the molecular weight, polydispersity index (PDI) and the conversion of the pCBT matrix. The GPC was performed on a modular system comprising a Waters 501 HPLC pump, a Waters 410 refractive index detector and a Waters column (Styragel® HR 4 THF). The mobile phase was unstabilized CHCl_3 at a flow rate of 1 mL/min at 30°C. In order to relate retention time to molecular weight, a universal calibration was made using narrow distribution polystyrene standards (Millipore Co., Massachusetts, USA). For sample preparation, approximately 4 mg of matrix was dissolved in a mixture of chloroform/hexafluoro-2-propanol (HFIP) (85/15 $\text{CHCl}_3/\text{HFIP}$). Samples containing carbon fibers were filtered before injection.

2.3.2. Mechanical tests

In this study, a universal testing machine (AG-100kNX, Shimadzu, Japan) was used to perform the tensile, flexural and short beam shear (SBS) tests at room temperature. Tensile tests were performed on the carbon/pCBT composites in accordance with the ASTM-D3039. Three-point bending and short beam shear (SBS) tests were carried out according to the ASTM D790 and D2344, respectively, to estimate the flexural and apparent interlaminar shear strength (ILSS). Tensile specimens cut from the prepared carbon/pCBT composite samples were $250 \times 25 \times 2 \text{ mm}^3$ in normal dimension and were clamped over an area of $50 \times 25 \text{ mm}^2$ at each end leaving a gauge length of 150 mm. Aluminum tabs were glued onto the ends of specimen to aid gripping areas. The grip pressure was hydraulically controlled. The testing cross-head speeds were 5 mm/min for the tensile test. The axial displacement was measured by the machine according to the movement of the crosshead. Three-point bending test was conducted to evaluate the flexural properties of the carbon/pCBT composites. Specimens in 138 mm long and 25.4 mm wide by 3.6 mm thick

were cut from the carbon/pCBT composite plates. A span length of 115 mm assured a span-to-depth ratio of 32, and a crosshead speed of 3.4 mm/min was adopted. A $22.8 \times 6 \times 3.6 \text{ mm}^3$ SBS specimen was placed on two cylindrical supports, each 2 mm in diameter, and bent in the middle by a cylindrical head 6 mm in diameter. The crosshead had a rate of 1 mm/min and there was a span-to-thickness ratio of 4.

The Izod impact test was performed at room temperature according to ASTM D256 on a pendulum impact tester (CPI, Atlas electric devices, USA) at impact energy of 2.54 J. The impact velocity used was 3.4 m/sec. The dimensions for the Izod impact specimen were $63.5 \times 12.7 \times 3.6 \text{ mm}^3$, and were provided with a $2.7 \pm .2 \text{ mm}$ deep notch. The notches in the samples were opened by using a notch opener (QC-640, Comotech testing machines, Taiwan), and were all with a notch tip radius of 0.25 mm. All the mechanical properties reported represent the average value of five readings at least. To investigate the effects of reinforcement on the carbon/pCBT composite failure modes, the failure and cross-sectional area of the damaged samples were examined using an optical microscope and SEM.

2.3.3. Morphology observation of the carbon/pCBT composites

The morphology of carbon/pCBT composites was examined under a polarized light microscope (PLM) equipped with a Linkam THMS 600 hot stage (Linkam, Epsom, UK). A quartz plate was used to determine the sign of the pCBT spherulite's birefringence. In this way, the first and third quarters of the sight were yellow and the second and fourth were blue when the forms were negative, while a reversed arrangement of the quarters was observed for positive forms. A small piece of CBT enclosed by high tenacity carbon fibers was pressed between two microscope slides and then inserted into the hot stage. Nitrogen was used as the purge gas in the hot stage during all measurements and thermal treatments. Each sample was heated to 230°C at a rate of $130^\circ\text{C}/\text{min}$, held for 30 min to allow for complete polymerization, and then cooled to the desired T_c at a rate of $60^\circ\text{C}/\text{min}$, where $T_c = 185, 195$ and 210°C .

2.3.4. Degree of crystallinity

The crystallinity of pCBT matrix were examined by DSC (TA-Du Pont DSC Q10 series) calibrated with indium at heating rate of $50^\circ\text{C}/\text{min}$. In order to suppress the reorganization and to avoid the superheating of high crystallinity specimens, which may influence the determination of crystallinity, higher heating rate of $50^\circ\text{C}/\text{min}$ was used. Experiments were run with samples ranging from 3~5 mg under nitrogen to prevent moisture and oxidative degradation. The crystallized matrix was heated from RT to 280°C at the rate of $50^\circ\text{C}/\text{min}$. The heat of fusion was determined from the areas under the melting peak. Correction was made to account the presence of the carbon fibers. The fiber mass fraction of the composite samples was accurately determined by thermogravimetric analysis after DSC analysis and the measured melting enthalpy was renormalized to the actual amount of pCBT presence in the sample. The degree of crystallinity (X_c) of the pCBT samples was calculated from Equation (1):

$$X_c = \frac{\Delta H}{(1 - M_f)H_f} \quad (1)$$

where M_f mass fraction of reinforcement, H_f heat of fusion of the fully perfect crystal of PBT with a value of 142 J/g [14, 15], ΔH absolute value of the heat of crystallization or fusion, measured as the area underneath the peaks.

3. Results and discussion

3.1. Results of the GPC measurements and crystallinity of the carbon/pCBT composites

Molecular weight is having an effect on processing, crystallization and mechanical properties of the crystalline polymer. Crystalline polymers have an additional strengthening mechanism resulting from their crystalline structure and as the chains become long, molecular entanglements and intermolecular forces become so great that the chains no longer slip over each other. However, segregation of low molecular weight oligomer at the spherulitic boundaries causes the weak boundary regions between spherulites. It is also having a detrimental effect on the mechanical properties of material [32]. Table 1

Table 1. Results of the GPC measurements and crystallinity on the carbon/pCBT composites at different T_c

T_c	185°C	195°C	210°C
M_w [kg/mol]	110	103	111
M_n [kg/mol]	42	45	51
M_w/M_n [PDI]	2.61	2.27	2.19
Conversion [%]	99.5	99.5	99.9
Crystallinity [%]	34	38	45

shows molecular weights, polydispersity index and the conversion of the pCBT matrixes measured by GPC. The number average molecular weight (M_n) for pCBT samples at $T_c = 210^\circ\text{C}$ was 51 kg/mol, whereas that for pCBT samples at $T_c = 185$ and 195°C ranged from 42~45 kg/mol. The percentages of conversion for all the pCBT samples were very high with value above 99.5%. As the crystallization temperature increases, the PDI decreased from 2.61 at 185°C to 2.19 at 210°C along with an increase in molecular weight. The results suggested that a low molecular weight tail was observed in the GPC traces and became obviously for the pCBT samples at lower T_c .

Figure 1 shows the DSC melting curves of carbon/pCBT composites prepared at different T_c . Double melting peaks appeared for carbon/pCBT samples at $T_c = 185$ and 195°C respectively. The crystallinity of the carbon/pCBT composites at different T_c were calculated and summarized in Table 1. All of the

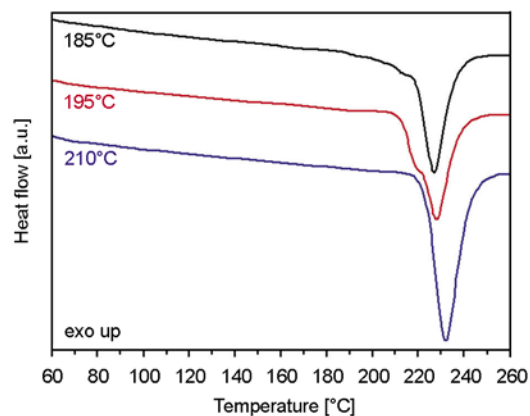


Figure 1. DSC melting thermograms of carbon/pCBT composites at different T_c

composites' crystallinity increased with rise in T_c . The carbon/pCBT sample that crystallized at 210°C exhibits the highest crystallinity: 45%, whereas samples at $T_c = 185$ and 195°C were 34 and 38% respectively.

3.2. The morphology of the carbon/pCBT composites

Figure 2 shows PLM images of the pCBT's crystalline morphologies during and complete crystallization at different T_c . The samples prepared at $T_c = 185$ and 195°C revealed unusual and mixed birefringence spherulite morphologies during crystallization. The spherulite size was larger in the sam-

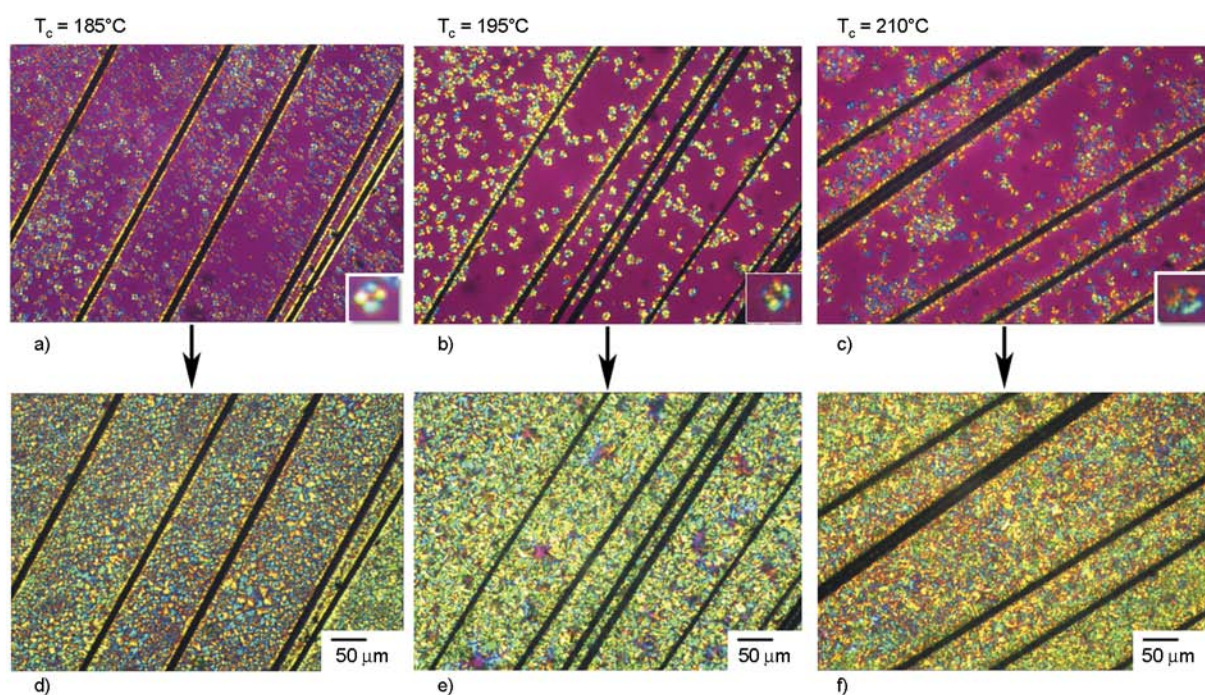


Figure 2. Crystalline morphologies of the carbon/pCBT composites during crystallization at different T_c : (a) 185°C , (b) 195°C , (c) 210°C and complete crystallization at different T_c : (d) 185°C , (e) 195°C , (f) 210°C

ple prepared at $T_c = 195^\circ\text{C}$ than that of $T_c = 185^\circ\text{C}$. Interestingly, boundary crystals and spherulitic boundary lines were found in the samples prepared at $T_c = 185$ and 195°C . The boundary crystals are attributed to the crystallization of low molecular weight pCBT molecules. The boundary region becomes a weak point of the material due to the segregation of low molecular weight oligomer at the spherulitic boundaries. The spherulitic boundary line became unclear gradually as the crystallization temperature increased. Worthy of notice is that the spherulitic boundary lines and the boundary crystals vanished in the samples prepared at $T_c = 210^\circ\text{C}$. As for the samples at $T_c = 210^\circ\text{C}$, the spherulite morphology was lost and highly disordered spherulitic crystallites were observed. In general, there is no work yet found to achieve less segregation boundary defects in highly crystalline material with large number of spherulites. The implication is that the potential strength of the highly crystalline material is large but the problem is to obtain good boundary cohesion. However, pCBT sample prepared at $T_c = 210^\circ\text{C}$ provides an opportunity to produce a polymer with high crystallinity, and less segregation boundary defects. It is believed that pCBT sample with high crystallinity and less boundary defects can provide good mechanical properties [25] and will be discussed later.

In all three conditions, the transcrystalline phenomenon was clearly observed (Figure 2). In contrast to samples from $T_c = 185$ and 195°C , a well-defined transcrystalline structure was revealed when the pCBT crystallized at 210°C . This is the first time that a well-defined transcrystalline structure was clearly observed in a pCBT polymer under quiescent crystallization conditions. Owing to the mutual interaction between the fiber and pCBT matrix, it can be assumed that the interfacial properties are excellent. Transcrystallization of pCBT can be attributed to heterogeneous nucleation induced by carbon fiber. However, as shown in Figure 2, spherulites abounded in the pCBT matrix and not affected by the crystallization temperature. This finding implies that the nucleation rate of pCBT resin shall be quite high and cause the difficulty on determining spherulitic growth rate and kinetics analysis [14]. It is noteworthy that all transcrystalline morphology might occur in the carbon/pCBT composites due to higher fiber volume fraction. The transcrystalline boundary

region (boundary crystal and boundary line) still can be formed in between the two growing transcrystals. Hence, the concept of weak boundaries is meaningful to explain the mechanical response of carbon/pCBT composites.

3.3. Effects of T_c on the mechanical properties of carbon/pCBT composites

Figure 3 shows the typical tensile stress-strain curves of the carbon/pCBT composites at different T_c . All the three samples demonstrate a severely vibrating curve before the final catastrophic fracture. The major failure modes, as shown in Figure 4, are long-range delamination (Figure 4a), and multifilament bundle shear breakage (Figure 4b). Due to the twill weave, stress concentrated on the fiber bundles around the interlace points and lead to their shear breakage. When the bundles split or experienced breakage, the released fracture energy dissipated through large amounts of long-range delamination, resulting in stress vibrations. Figure 5 displays the SEM micrographs of carbon/pCBT sample corroborates the good interfacial bonding between the constituent materials. All the carbon fiber bundles were coated with pCBT resins. Thus, the long-range delamination was due to cohesive failure of the pCBT matrix. Fine voids were developed at specimen's defects such as spherulite/transcrystalline boundaries and grown into the specimen. Failure along the spherulite/transcrystalline boundaries was promoted by decohesion between the spherulites due to the missing inter-spherulitic tie chains. Weak sites in the boundaries for pCBT composite sample at $T_c = 185^\circ\text{C}$ was caused by segregation phenom-

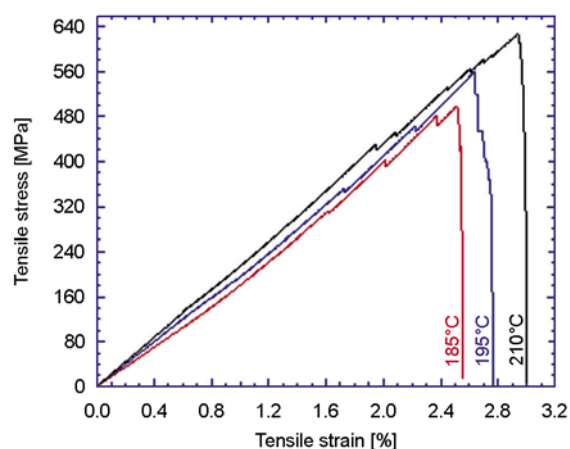


Figure 3. Typical tensile stress-strain curves of the carbon/pCBT composites at different T_c



Figure 4. Typical tensile failure modes for the carbon/pCBT composites. (a) lateral view: delamination failure, (b) front view: shear breakage of bundle filaments.

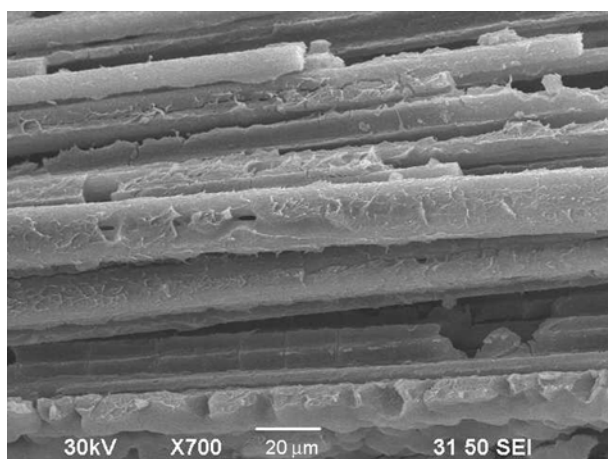


Figure 5. SEM image showing good interfacial fiber/matrix bonding and resulted in the cohesive failure for the carbon/pCBT composites

ena and enrichment of low molecular weight species (large PDI) being ejected from the crystallizing front.

Table 2 summarizes the tensile properties of carbon/pCBT composites with different T_c . All of the composites' tensile properties increased with a rise in T_c . The carbon/pCBT sample that crystallized at 210°C exhibited the highest tensile modulus: 22.2 GPa and greatest strength: 595 MPa, 14 and 17% greater, respectively, than those of the composite sample at $T_c = 185^\circ\text{C}$. It is worthy to notice that the spherulite morphology of the $T_c = 210^\circ\text{C}$ sample exhibited highly disordered crystallites with-

Table 2. Mechanical properties of the carbon/pCBT composites at different T_c

T_c	185°C	195°C	210°C
Tensile modulus [GPa]	19.4±1.8	20.5±1.4	22.2±1.3
Tensile strength [MPa]	510±13	546±29	595±32
Tensile elongation [%]	2.35±0.38	2.55±0.15	2.86±0.21
Flexural modulus [GPa]	43.6±2.4	42.4±1.0	45.1±3.3
Flexural strength [MPa]	403±8	407±9	508±13
Impact energy [J/m]	779±4	774±8	809±8
ILSS [MPa]	54.1±1.2	55.2±1.0	59.7±0.4

out clear spherulitic boundaries or boundary crystals. This matrix behaved like a homogeneous material without phase separation. Morphology that contained clear boundaries and boundary crystals (defects) had a negative effect that caused a decrease in tensile performance.

Figure 6 shows the typical flexural stress-strain curves of the carbon/pCBT composites at different T_c . Flexural properties such as flexural modulus and strength were summarized in Table 2. Similarly to the tensile results; all the curves exhibited a severe vibration at flexural strain larger than 1%. This stress vibration is relative to the fiber bundle breakage and short-range delamination. Failure modes: compressive, tensile failures and shear delamination, are seen in Figure 7a. The failure on the tension surface involved fiber bundle breakage, cracks and short range delamination (Figure 7b). The compression surface failure included local buckling

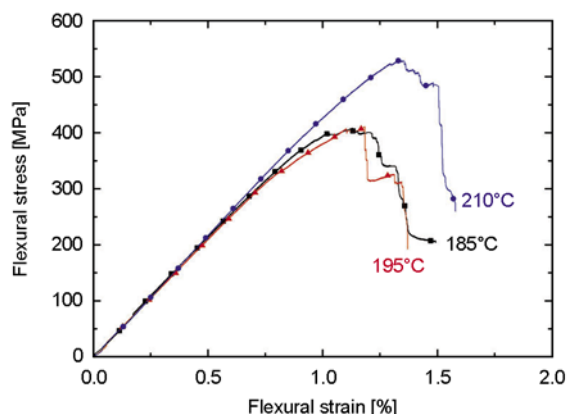


Figure 6. Typical flexural stress-strain curves of the carbon/pCBT composites at different T_c

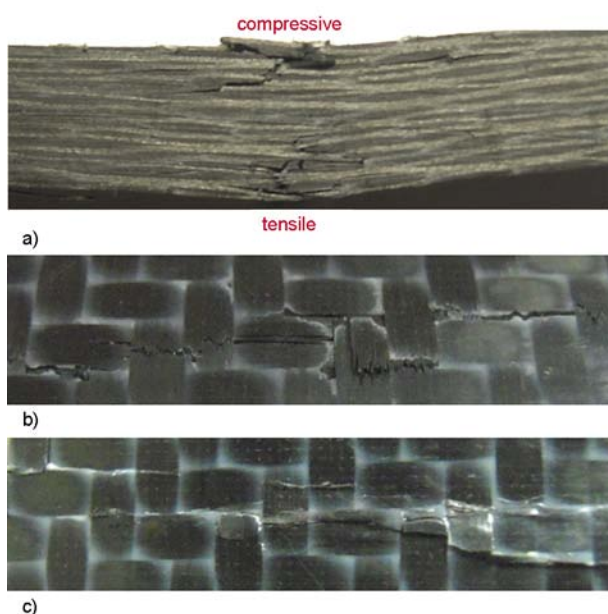


Figure 7. Typical flexural failure for the carbon/pCBT composites, (a) lateral view, (b) tensile surface, (c) compression surface

which manifested as fiber micro-buckling and ply-level buckling (Figure 7c). The ply-level buckling caused short range delamination of the outer ply. All of the samples, however, did not collapse directly under flexural loading. This demonstrates that the reinforcement of the carbon fabric prevents crack propagation.

Also similar to the tensile results, the composite sample at $T_c = 210^\circ\text{C}$ exhibited the highest flexural modulus: 45.1 GPa (as shown in Table 2), which is attributed to a higher degree of crystallinity (44%). The flexural strength of the composite sample at $T_c = 210^\circ\text{C}$ was 508 MPa, whereas samples at $T_c = 185$ and 195°C were 403~407 MPa, with 26% enhancement. These results demonstrate that crystalline mor-

phology strongly influenced the mechanical properties of the carbon/pCBT composites. Sample morphology without spherulitic boundaries prevents the crack initiation and growth. In addition, pCBT samples with high crystallinity promote the resistance of crack propagation. Hence, composite samples at $T_c = 210^\circ\text{C}$ containing highly disordered crystallites without spherulitic boundaries or boundary crystals displayed the best tensile and flexural property results.

The notched Izod impact properties of the composites are shown in Table 2. The impact energy for composite samples at $T_c = 210^\circ\text{C}$ was 809 J/m, whereas for samples at $T_c = 185$ and 195°C ranged from 774~779 MPa and had 5% enhancement. The failure modes for impacted carbon/pCBT composites had tensile and compressive failure, but did not break apart (Figure 8a). This impact failure reveals the preventive ability of the reinforcing woven fabric against cracking. When the impactor encountered the carbon/pCBT specimen, fiber bundle pull-out and breakage occurred around the notched side of the composite, while compressive force built up on the other side and caused crush of fibers and matrixes (Figure 8b). Figure 8c shows typical impact failure included fiber bundle crush and kink fracture, short range delamination in the compressive side of pCBT composites. A close view of the impacted carbon/pCBT composite in the tensile side, shown in Figure 9, reveals that all the pull-out fiber bundles were coated with pCBT resin. These results demonstrate that there is strong interfacial bonding between the carbon fiber and pCBT. The cohesive failure that occurred in the pCBT matrix was attributed to the brittleness of the pCBT resin. The ILSS is a non-fiber dominated property that is influenced by both the matrix and interfacial properties. When the composite sample was subjected to loading, cracks normal to the loading direction formed either at the matrix/fiber interface or in the matrix. A low ILSS is therefore an indication of poor fiber/matrix interfacial properties or matrix brittleness.

There were no visible failures found during the ILSS testing of the pCBT composite samples. Failures may be preceded by less obvious, local damage, such as transply cracking. Figure 10 shows the typical load-displacement curves of the carbon/pCBT composites at different T_c . The interlaminar

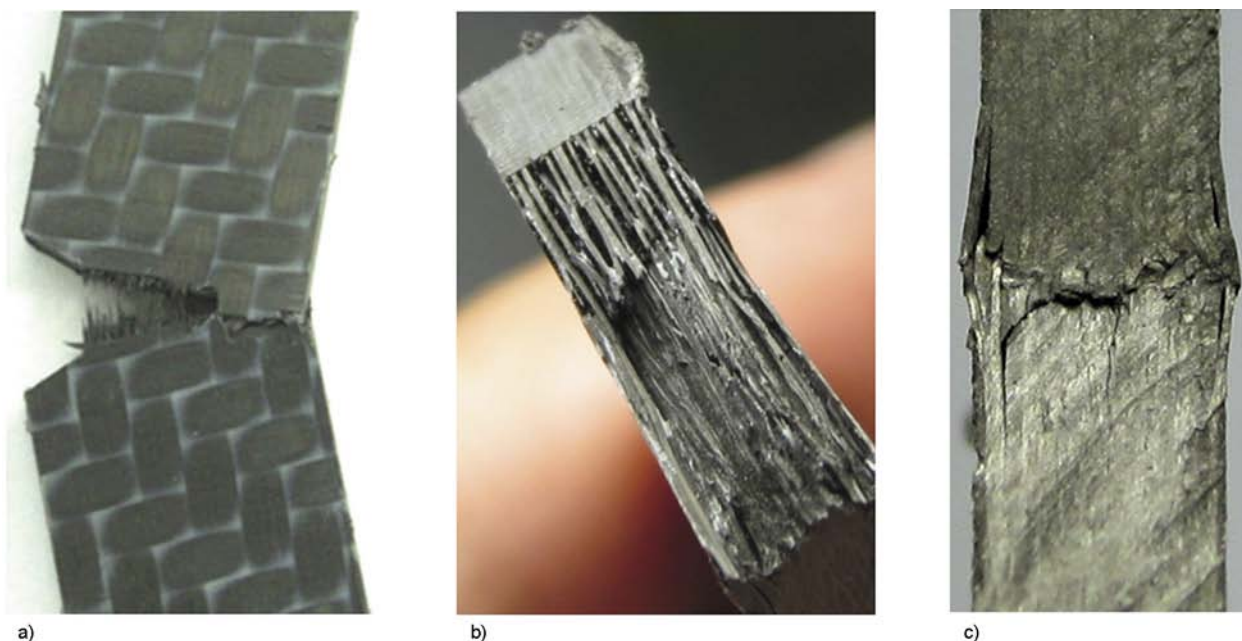


Figure 8. Typical impact failure modes for the carbon/pCBT composites: (a) lateral view, (b) top view, (c) compressive side

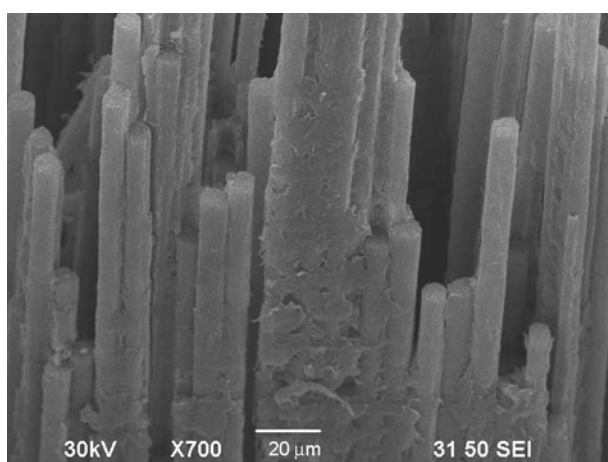


Figure 9. SEM images for the impact failure carbon/pCBT composites at tensile side showing cohesive failure at the fiber/matrix interphase

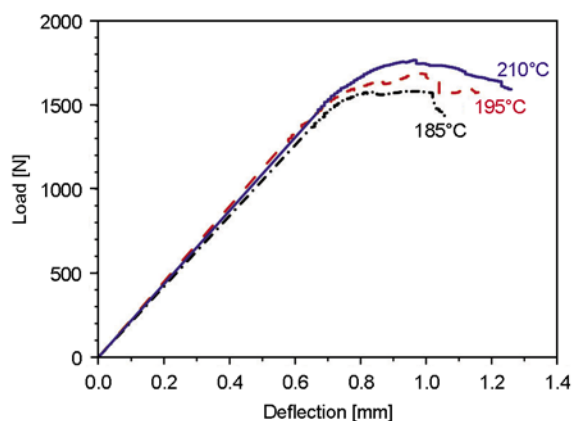


Figure 10. Typical load-displacement curves of short beam shear test for the carbon/pCBT composites at different T_c

shear strength (ILSS) for carbon/pCBT composites was determined from the load-displacement curves and listed in Table 2. As shown in Table 2, for the sample of $T_c = 210^\circ\text{C}$ displayed the highest ILSS: 59.7 MPa, which was much higher than those obtained from the glass/pCBT composites (34.3 MPa) [16]. Remember that the transcrystalline morphology and cohesive failure were found in all the carbon/pCBT composite samples. Slight variation in the ILSS (54~59 MPa) revealed the effects of transcrystalline and crystallinity on the interfacial adhesion.

4. Conclusions

In this study, carbon/pCBT composites were prepared by a modified film stacking technique. Results demonstrated that their mechanical properties were strongly affected by crystalline morphologies and crystallinity. A well-defined transcrystallinity can be clearly seen in carbon/pCBT composites in quiescent crystallization conditions. The low crystallinity of the carbon/pCBT composites sample crystallized at 185°C with spherulitic structure led to large area spherulite/transcrystalline boundary region. Consequently, the crack tended to initiate and propagate along the ‘weak’ spherulite/

transcrystalline boundaries, resulting in a low value of mechanical properties. The carbon/pCBT composite sample prepared at $T_c = 210^\circ\text{C}$ and displaying highly disordered spherulitic crystallites without spherulite/transcrystalline boundary lines or boundary crystals exhibited the best mechanical properties.

Acknowledgements

Part of this work is financially supported from the National Science Council of Taiwan, ROC, under contract number NSC 98-2221-E-035-001.

References

- [1] Brunelle D. J.: Cyclic oligomer chemistry. *Journal of Polymer Science Part A: Polymer Chemistry*, **46**, 1151–1164 (2008).
DOI: [10.1002/pola.22526](https://doi.org/10.1002/pola.22526)
- [2] Brunelle D. J., Bradt J. E., Serth-Guzzo J., Takekoshi T., Evans T. L., Pearce E. J., Wilson P. R.: Semicrystalline polymers via ring-opening polymerization: Preparation and polymerization of alkylene phthalate cyclic oligomers. *Macromolecules*, **31**, 4782–4790 (1998).
DOI: [10.1021/ma971491j](https://doi.org/10.1021/ma971491j)
- [3] Parton H., Verpoest I.: In situ polymerization of thermoplastic composites based on cyclic oligomers. *Polymer Composites*, **26**, 60–65 (2005).
DOI: [10.1002/pc.20074](https://doi.org/10.1002/pc.20074)
- [4] Mohd Ishak Z. A., Gatos K. G., Karger-Kocsis J.: On the in-situ polymerization of cyclic butylene terephthalate oligomers: DSC and rheological studies. *Polymer Engineering and Science*, **46**, 743–750 (2006).
DOI: [10.1002/pen.20486](https://doi.org/10.1002/pen.20486)
- [5] Mohd Ishak Z. A., Shang P. P., Karger-Kocsis J.: A modulated DSC study on the in situ polymerization of cyclic butylene terephthalate oligomers. *Journal of Thermal Analysis and Calorimetry*, **84**, 637–641 (2006).
DOI: [10.1007/s10973-005-7059-z](https://doi.org/10.1007/s10973-005-7059-z)
- [6] Harsch M., Karger-Kocsis J., Apostolov A. A.: Crystallization-induced shrinkage, crystalline, and thermo-mechanical properties of in situ polymerized cyclic butylene terephthalate. *Journal of Applied Polymer Science*, **108**, 1455–1461 (2008).
DOI: [10.1002/app.27798](https://doi.org/10.1002/app.27798)
- [7] Lehmann B., Karger-Kocsis J.: Isothermal and non-isothermal crystallisation kinetics of pCBT and PBT: Polymers as studied by DSC. *Journal of Thermal Analysis and Calorimetry*, **95**, 221–227 (2009).
DOI: [10.1007/s10973-007-8939-1](https://doi.org/10.1007/s10973-007-8939-1)
- [8] Karger-Kocsis J., Shang P. P., Mohd Ishak Z. A., Rösch M.: Melting and crystallization of in-situ polymerized cyclic butylene terephthalates with and without organoclay: A modulated DSC study. *Express Polymer Letters*, **1**, 60–68 (2007).
DOI: [10.3144/expresspolymlett.2007.12](https://doi.org/10.3144/expresspolymlett.2007.12)
- [9] Lanciano G., Greco A., Maffezzoli A., Mascia L.: Effects of thermal history in the ring opening polymerization of CBT and its mixtures with montmorillonite on the crystallization of the resulting poly(butylene terephthalate). *Thermochimica Acta*, **493**, 61–67 (2009).
DOI: [10.1016/j.tca.2009.04.004](https://doi.org/10.1016/j.tca.2009.04.004)
- [10] Tripathy A. R., Elmoumni A., Winter H. H., MacKnight W. J.: Effects of catalyst and polymerization temperature on the in-situ polymerization of cyclic poly(butylene terephthalate) oligomers for composite applications. *Macromolecules*, **38**, 709–715 (2005).
DOI: [10.1021/ma0483874](https://doi.org/10.1021/ma0483874)
- [11] Hakmé C., Stevenson I., Maazouz A., Cassagnau P., Boiteux G., Seytre G.: In situ monitoring of cyclic butylene terephthalate polymerization by dielectric sensing. *Journal of Non-Crystalline Solids*, **353**, 4362–4365 (2007).
DOI: [10.1016/j.jnoncrysol.2007.04.051](https://doi.org/10.1016/j.jnoncrysol.2007.04.051)
- [12] Parton H., Baets J., Lipnik P., Goderis B., Devaux J., Verpoest I.: Properties of poly(butylene terephthalate) polymerized from cyclic oligomers and its composites. *Polymer*, **46**, 9871–9880 (2005).
DOI: [10.1016/j.polymer.2005.07.082](https://doi.org/10.1016/j.polymer.2005.07.082)
- [13] Parton H.: Characterization of the in-situ polymerization production process for continuous fiber reinforced thermoplastics. PhD thesis, Department of Metallurgy and Materials Science Katholieke Universiteit Leuven, Belgium (2006).
- [14] Wu C-M., Jiang C-W.: Crystallization and morphology of polymerized cyclic butylene terephthalate. *Journal of Polymer Science Part B: Polymer Physics*, **48**, 1124–1134 (2010).
DOI: [10.1002/polb.21998](https://doi.org/10.1002/polb.21998)
- [15] Wu C-M., Huang C-W.: Melting and crystallization behavior of copolymer from cyclic butylene terephthalate and polycaprolactone. *Polymer Engineering and Science*, **51**, 1004–1013 (2011).
DOI: [10.1002/pen.21910](https://doi.org/10.1002/pen.21910)
- [16] Mohd Ishak Z. A., Leong Y. W., Steeg M., Karger-Kocsis J.: Mechanical properties of woven glass fabric reinforced in situ polymerized poly(butylene terephthalate) composites. *Composites Science and Technology*, **67**, 390–398 (2007).
DOI: [10.1016/j.compscitech.2006.09.012](https://doi.org/10.1016/j.compscitech.2006.09.012)
- [17] Tripathy A. R., MacKnight W. J., Kukureka S. N.: In-situ copolymerization of cyclic poly(butylene terephthalate) oligomers and ϵ -caprolactone. *Macromolecules*, **37**, 6793–6800 (2004).
DOI: [10.1021/ma0400517](https://doi.org/10.1021/ma0400517)
- [18] Baets J., Dutoit M., Devaux J., Verpoest I.: Toughening of glass fiber reinforced composites with a cyclic butylene terephthalate matrix by addition of polycaprolactone. *Composites Part A: Applied Science and Manufacturing*, **39**, 13–18 (2008).
DOI: [10.1016/j.compositesa.2007.09.013](https://doi.org/10.1016/j.compositesa.2007.09.013)

- [19] Tripathy A. R., Chen W., Kukureka S. N., MacKnight W. J.: Novel poly(butylene terephthalate)/poly(vinyl butyral) blends prepared by in situ polymerization of cyclic poly(butylene terephthalate) oligomers. *Polymer*, **44**, 1835–1842 (2003).
DOI: [10.1016/S0032-3861\(03\)00029-6](https://doi.org/10.1016/S0032-3861(03)00029-6)
- [20] Jiang Z., Siengchin S., Zhou L.-M., Steeg M., Karger-Kocsis J., Man H. C.: Poly (butylene terephthalate)/silica nanocomposites prepared from cyclic butylene terephthalate. *Composites Part A: Applied Science and Manufacturing*, **40**, 273–278 (2009).
DOI: [10.1016/j.compositesa.2008.12.003](https://doi.org/10.1016/j.compositesa.2008.12.003)
- [21] Baets J., Godara A., Devaux J., Verpoest I.: Toughening of polymerized cyclic butylene terephthalate with carbon nanotubes for use in composites. *Composites Part A: Applied Science and Manufacturing*, **39**, 1756–1761 (2008).
DOI: [10.1016/j.compositesa.2008.08.004](https://doi.org/10.1016/j.compositesa.2008.08.004)
- [22] Wu F., Yang G.: Synthesis and properties of poly(butylene terephthalate)/multiwalled carbon nanotube nanocomposites prepared by *in situ* polymerization and *in situ* compatibilization. *Journal of Applied Polymer Science*, **118**, 2929–2938 (2010).
DOI: [10.1002/app.32625](https://doi.org/10.1002/app.32625)
- [23] Romhány G., Vígh J., Thomann R., Karger-Kocsis J., Sajó I. E.: pCBT/MWCNT nanocomposites prepared by in situ polymerization of CBT after solid-phase high-energy ball milling of CBT with MWCNT. *Macromolecular Materials and Engineering*, **296**, 544–550 (2011).
DOI: [10.1002/mame.201000381](https://doi.org/10.1002/mame.201000381)
- [24] Baets J., Godara A., Devaux J., Verpoest I.: Toughening of isothermally polymerized cyclic butylene terephthalate for use in composites. *Polymer Degradation and Stability*, **95**, 346–352 (2010).
DOI: [10.1016/j.polymdegradstab.2009.11.005](https://doi.org/10.1016/j.polymdegradstab.2009.11.005)
- [25] Mäder E., Gao S.-L., Plonka R., Wang J.: Investigation on adhesion, interphases, and failure behaviour of cyclic butylene terephthalate (CBT[®])/glass fiber composites. *Composites Science and Technology*, **67**, 3140–3150 (2007).
DOI: [10.1016/j.compscitech.2007.04.014](https://doi.org/10.1016/j.compscitech.2007.04.014)
- [26] Shahzad M. A., Steeg M., Mitschang P.: Development and characterization of glass fiber reinforced in-situ polymerized thermoplastic matrix composite material. in 'SAMPE 2010, Seattle Canada' p15 (2010).
- [27] Baets J., Devaux J., Verpoest I.: Toughening of basalt fiber-reinforced composites with a cyclic butylene terephthalate matrix by a nonisothermal production method. *Advances in Polymer Technology*, **29**, 70–79 (2010).
DOI: [10.1002/adv.20176](https://doi.org/10.1002/adv.20176)
- [28] Balogh G., Czigany T.: Effect of low UD carbon fibre content on mechanical properties of *in situ* polymerised cyclic butylene terephthalate. *Plastics, Rubber and Composites*, **40**, 121–124 (2011).
DOI: [10.1179/1743289811X12988633927871](https://doi.org/10.1179/1743289811X12988633927871)
- [29] Aurrekoetxea J., Zurbitu J., Ortiz de Mendibil I., Agirregomezkorta A., Sánchez-Soto M., Sarrionandia M.: Effect of superelastic shape memory alloy wires on the impact behavior of carbon fiber reinforced in situ polymerized poly(butylene terephthalate) composites. *Materials Letters*, **65**, 863–865 (2011).
DOI: [10.1016/j.matlet.2010.12.020](https://doi.org/10.1016/j.matlet.2010.12.020)
- [30] López-Arraiza A., Amenabar I., Agirregomezkorta A., Agirregomezkorta, Aurrekoetxea J.: Experimental analysis of drilling damage in carbon-fiber reinforced thermoplastic laminates manufactured by resin transfer moulding. *Journal of Composite Materials*, in press (2011).
DOI: [10.1177/0021998311414218](https://doi.org/10.1177/0021998311414218)
- [31] Chen J. C., Wu C. M., Pu F. C., Chiu C. H.: Fabrication and mechanical properties of self-reinforced poly(ethylene terephthalate) composites. *Express Polymer Letters*, **5**, 228–237 (2011).
DOI: [10.3144/expresspolymlett.2011.22](https://doi.org/10.3144/expresspolymlett.2011.22)
- [32] Karger-Kocsis J.: Microstructural aspects of fracture in polypropylene and in its filled, chopped fiber and fiber mat reinforced composites. in 'Polypropylene: Structure, blends and composites, Vol. I Structure and Morphology' (ed.: Karger-Kocsis J.) Chapman and Hall, London, 142–201 (1995).

Exploring a novel multifunctional agent to improve the dispersion of short aramid fiber in polymer matrix

G. S. Shibulal, K. Naskar*

Rubber Technology Centre, Indian Institute of Technology, Kharagpur-721302, West Bengal, India

Received 28 september 2011; accepted in revised form 19 November 2011

Abstract. Composites based on resorcinol formaldehyde latex (RFL) coated aramid short fiber and a polyolefin based thermoplastic elastomer, namely ethylene octene copolymer (EOC) were prepared by melt mixing technique. The effects of both fiber loading and its length on the mechanical and thermal characteristics of the composite under natural and sheared conditions were investigated. Both the low strain modulus and Young's modulus were increased as a function of fiber loading and length. However, thermal stability of the composite was found to enhance with increase in fiber loading and was independent of fiber length. Due to poor interfacial interaction between the fiber and the matrix and the formation of fiber aggregation especially with 6 mm fiber at high loading, the elongation and toughness of the composite were found to decrease drastically. In order to solve this problem, a maleic anhydride adducted polybutadiene (MA-g-PB) was applied on the aramid fiber. The improvements in tensile strength, elongation at break, toughness to stiffness balance and a good quality of fiber dispersion especially with 6 mm short fiber were achieved. These results indicate the potential use of maleic anhydride adducted PB as a multifunctional interface modifying coupling agent for the aramid short fiber reinforced polymers to enhance the mechanical properties as well as fiber dispersion. FTIR analyses of the treated fiber and SEM analyses of the tensile fractured surfaces of the composite strongly support and explain these results.

Keywords: reinforcements, thermoplastic elastomer, short fiber, multifunctional agent, mechanical properties

1. Introduction

Polyolefin based thermoplastic elastomers (TPE) have received considerable attention due to their chemical inertness, low density and low cost compared to other thermoplastic elastomers (TPEs). Ethylene octene copolymer (EOC) is a new class of polyolefin based metallocene catalyzed thermoplastic elastomers, which have recently gained much attention because of their random comonomer distribution, narrow molecular weight distribution and a controlled level of long chain branching [1, 2]. Moreover these are available in pellet form that helps in easy handling, faster mixing and compounding. Compared to the well known conventional polyolefin elastomer EPDM, EOC exhibits faster mixing and better dispersion when blending

with thermoplastics like PP, PE etc. The structure and properties of a random ethylene octene copolymer strongly depends on the composition of ethylene and 1-octene as well as the condition of crystallization. The crystallinity decreases with increasing concentration of the comonomer 1-octene. The yield stress and the modulus at higher strain decrease as the comonomer content of EOC increases, which is due to the decreasing crystallinity. The low crystalline ethylene 1-octene copolymers behave like TPE by exhibiting a stress-strain curve similar to TPE. The use of this polymer has been tested very successfully as an impact modifier for PP by many researchers [3–5]. Recently our research group studied the use of EOC as an alternative for the traditional EPDM/PP blend and developed a new class

*Corresponding author, e-mail: knaskar@rtc.iitkgp.ernet.in
© BME-PT

of EOC/PP based thermoplastic vulcanizates (TPVs) by the dynamic vulcanization process with peroxide assisted co-agents [6–7]. EOC and functionalized EOC find application as an impact modifier to other polar and brittle thermoplastics also. Chapleau *et al.* reported the impact modification of polyethylene terephthalate (PET) with an Engage grade of EOC by chemical compatibilization of the two with the addition of glycidyl methacrylate (GMA) grafted polyolefins [8]. Aróstegui and Nazábal [9] developed a super tough polybutylene terephthalate (PBT) by melt blending with 20% EOC and different levels of difunctional epoxy resin in a twin screw extruder followed by injection molding. The impact modification of polyacetal (POM) with EOC by dynamic vulcanization with dicumyl peroxide was reported by Uthaman *et al.* [10]. Guerrica *et al.* developed an EOC toughened polymethylene terephthalate (PMT) compatibilised with partially maleated EOC [11]. Yu *et al.* [12] prepared a super tough Nylon 6 by using maleated EOC as a toughener. Though EOC enhances the low temperature impact resistance for both the commodity thermoplastics like polypropylene and engineering thermoplastics like PET, Nylon, POM etc, the sole use of this TPE is limited for load bearing and high temperature engineering applications because of its poor mechanical properties especially low strain modulus, poor dimensional stability and low thermal stability. Reinforcing the EOC with proper reinforcing agent, which can enhance both strength and thermal stability is one of the ways to overcome this problem. The reinforcement of thermoplastic elastomers with short fibers have gained much attention in the recent times, since it can reinforce the matrix and can give good strength and stiffness comparatively with a low volume fraction of fibers [13]. Moreover, the TPE-short fiber composites can be recycled easily. Among the short fibers available, aramid is one of the good candidates in the short fiber arena. These kinds of fibers have a unique combination of strength, stiffness and high temperature stability. However, it shows lesser mechanical bonding (adhesion) with the polymer matrix. The application of chemical treatment like N-alkylation, RFL dipping, plasma treatment and polymer grafting to improve surface roughness and to bring various functional groups on the fiber surface is highly required for these kinds of fibers to improve the

adhesion with the elastomeric matrix. Generally, for polar fibers like Rayon, Nylon etc. sufficient rubber adhesion is achieved by treating and curing the fiber with resorcinol formaldehyde latex (RFL) dip prior to its incorporation in the rubber matrix. The resorcinol formaldehyde (RF) component promotes adhesion to the cord via polar or covalent interaction, while the dried latex (L) co-vulcanizes with the rubber matrix ensuring adhesion to that matrix. For aramid fibers, simple treatment with RFL leads to rubber composite exhibiting low fiber to matrix adhesion with failure often occurring at the fiber-RFL dip interface. This is due to the physical structure of the aramid, which being highly crystalline provides an uninviting surface to the components making up the RFL. Excellent aramid to rubber adhesion can be achieved by first activating the aramid with low molecular weight and highly reactive epoxies prior to RFL treatment. These kinds of treatment on the fiber surfaces impart some roughness on the fiber surface, which allows more micro-mechanical interlocking between the polymer and the fiber leading to higher bond strength even though other interactions may be weak [14–16]. The use of a reactive compatibilizer like maleic anhydride grafted polymer with a non polar part having a structure similar to the polymer matrix is also used to bring fiber-matrix interaction in aramid fiber reinforced composites [17]. Many researchers have reported various studies carried out with different kinds of aramid short fibers on a variety of thermoplastic elastomers. Arroyo and Bell [18] reported the morphology/behavior and recyclability of the Twaron[®] fiber reinforced PP/EPDM TPE. Kutty and coworkers [19, 20] extensively studied various aspects of Kevlar[®] short fiber reinforced polyurethane based thermoplastic elastomer systems. Recently Akbarian *et al.* [21] reported dynamic mechanical and rheological behavior of a Twaron fiber reinforced ester based thermoplastic polyurethane. However, only very few literatures are available regarding the reinforcement studies of EOC with short fibers [22, 23]. There seems to be no previous studies made on the reinforcement aspects of ethylene-octene copolymers with any kind of aramid short fiber in general and short RFL coated Technora aramid fiber in particular. Very recently the authors [24] have reported on the mechanical, morphological and rheological behavior of EOC

with RFL dipped Technora aramid short fiber having a fixed aspect ratio and the effectiveness of MA-g-PB as a compatibilising agent between the fiber and the EOC matrix. The present paper focuses on the mechanical and thermomechanical properties of EOC reinforced with aramid fiber having different aspect ratios at different loading levels with special reference to fiber orientations and the effect of a low molecular weight maleic anhydride grafted 1,2 polybutadiene (MA-g-PB) as an interface modifier to maintain toughness to stiffness balance at higher fiber loading.

2. Experimental

2.1. Materials

Ethylene octene copolymer (trade name EXACT[®] 5061 (specific gravity of 0.868 g/cc at 23°C; comonomer (octene) content of 13%; melting temperature (T_m) of 52.8°C, melt flow index (MFI) of 0.5 at 190°C/2.16 kg was procured from Exxon Mobil Chemical Company, USA. Aramid short fiber (trade name Technora[®]) with a chemical name copoly-(paraphenylene/3, 4'-oxydiphenylene terephthalamide) was obtained from Teijin Aramid BV, The Netherlands. The detail specifications of the fiber are given in Table 1. Maleic anhydride adducted 1,2 polybutadiene (trade name Ricon[®] 131 MA5) having a number average molecular weight (M_n) of 5300, a specific gravity of 0.9 g/cc and maleic anhydride content of 5% was obtained from Sartomer Company, USA.

Table 1. Technical specifications of technora[®] (RFL coated aramid short fiber)

Parameter / Properties	Value
Colour	Gold
Specific gravity	1.39
Equilibrium moisture regain [%]	2
Average fiber length [mm]	1/3/6
Diameter [μm]	10–12
Average aspect ratio [L/D ratio]	91/275/550
Young's modulus [GPa]	20–21
Tensile strength [MPa]	3000–3500
Elongation at break [%]	5–7

2.2. Preparation of composites

Formulations used for the preparation of the composites are given in Table 2. The short fiber loading was varied from 1 to 10 phr. All the composites were prepared by melt mixing of the components in

Table 2. Formulations of the mixes in phr (parts per hundred rubber)

Sample designation	Short fiber length [mm]	Short fiber loadings [phr]	MA-g-PB [phr]
1RAF ₃	1	3	–
1RAF ₅	1	5	–
1RAF ₁₀	1	10	–
3RAF ₃	3	3	–
3RAF ₅	3	5	–
3RAF ₁₀	3	10	–
6RAF ₃	6	3	–
6RAF ₅	6	5	–
6RAF ₁₀	6	10	–
6RAF ₁₀ C ₃	6	10	3
6RAF ₂₀ C ₃	6	20	3

*RAF indicates RFL coated aramid fiber, left side Arabic number indicate fiber length in mm and the subscript number indicates its concentration in phr, C stands for the interface modifying coupling agent and the subscript number indicates its concentration in phr.

a Haake Rheomix 600 OS internal mixer having a chamber volume of 85 cm³ at a temperature of 80°C with a rotor speed of 80 rpm for 10 minutes. In order to achieve better dispersion, half portion of the polymer was first melted for one minute and to this half portion of fiber was added and the mixing was continued for another one minute. The sequence is again repeated for 2 to 3 min with the remaining portion of polymer and the mixing was continued up to 10 min after adding remaining portion of the fiber at 3rd min at a constant rotor speed of 80 rpm. The modifier (MA-g-PB) was incorporated by first warming the modifier at 70–80°C and then added dropwise to the short fiber taken in a flask/beaker and stirring with a magnetic stirrer at 100°C for 10 minute at low speed. The compatibilizer/fiber mix is then added into the mixing chamber containing the molten polymer at the 2nd min in one stretch and continued the mixing up to 10 min at the same rpm. After the mixing is over, the composite was discharged and passed through a two roll mill once to get a flat sheet. The sheet was then pressed in a compression molding press (Moore Press, Birmingham, UK) at 100°C for 3 min at a pressure of 7 MPa and then cooled down to room temperature under the same pressure by circulating cold water to get randomly oriented fiber composites (composites in unsheared condition). Composites with a high degree of fiber orientation (composites in sheared condition) were prepared by extrusion of the fiber/matrix

Table 3. Processing conditions followed for the extrusion of the composite

Processing conditions	Zone-1	Zone-2	Zone-3	Zone-4	Zone-5	Zone-6	Die exit
Temperature [°C]	70	75	80	90	100	100	100
Screw [rpm]	80	----->					

blend through a circular die using a twin screw extruder fitted with Haake Rheomix 600 OS. The processing conditions followed for this extrusion are presented in Table 3. Extrudate were cut, stacked side by side and compression molded using the same conditions mentioned above.

2.3. Characterization of the composites

Mechanical properties

The dumb-bell shaped specimens of the composites in parallel and perpendicular directions with respect to the mill direction used for testing were die cut from the compression molded sheet and the testing was done after 24 hours of maturation at room temperature. Tensile properties were measured according to ASTM D 412-98A using a universal testing machine Hounsfield H10KS (UK) at a constant cross-head speed of 500 mm/min. All the values were averages of three measurements.

Spectroscopic characterization

Fourier transform infrared (FTIR) spectra were recorded in the range of 400–4500 cm^{-1} using a Perkin-Elmer FTIR Spectrometer (model Spectrum RX-I) with a resolution of 4 cm^{-1} . Films of approximately 0.1 mm thickness were obtained by compression molding 1–2 gram sample using a laboratory press (temperature: 100°C and pressure 7 MPa).

Dynamic Mechanical Thermal Analyses (DMTA)

Dynamic mechanical thermal properties of the composites were measured using a dynamic mechanical thermal analyser (DMTA 2980 V1.7B, TA instruments, USA) in dual cantilever mode. The temperature sweep study was made from –80 to +80°C at a heating rate of 3°C/minute and a frequency of 1 Hz. The storage modulus and loss tangent were recorded for all the samples under identical conditions.

Thermal Degradation Studies (TGA)

Thermal stability of the composites were measured by thermogravimetric analyses (TGA) using Q50 V6.1 series, TA instruments (New Castle, Delaware), from ambient temperature to 600°C at a pro-

grammed heating rate of 10°C/min under nitrogen atmosphere. A sample weight of 8–10 mg was taken for all the investigation. The weight loss against temperature was recorded.

Morphological Analysis- Tensile fractured samples of the composites were analysed using a JEOL (JSM 5800, Japan) scanning electron microscope (SEM). The samples were sputter coated with gold prior to the analyses.

3. Results and discussion

3.1. Effect of short fiber loading on the mixing characteristics and mechanical properties

The mixing torque-time relationship of the EOC/short fiber composite as a function of short fiber loading and length is shown in Figure 1 and Table 4. The characteristics of these torque curves show high initial torque with irregular broad peaks from 0 to 4 minutes, is due to the sequential feeding of the matrix material in the pellet form followed by the

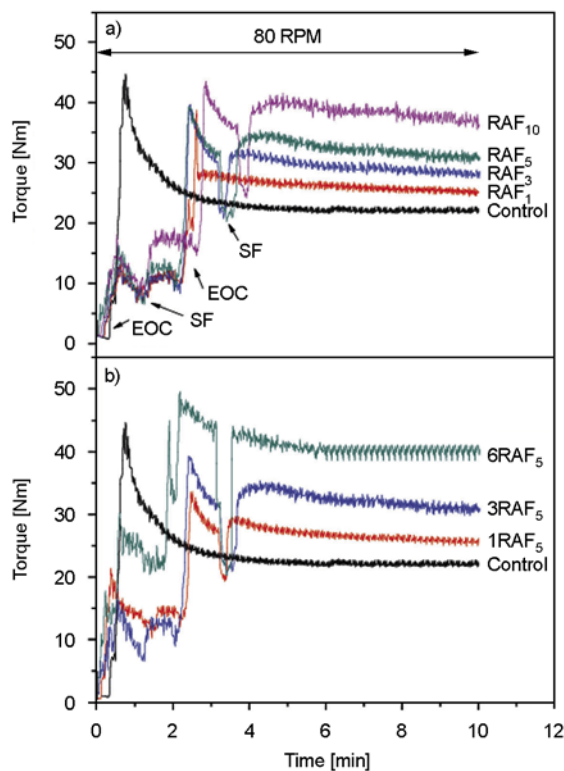


Figure 1. Mixing torque-time relationship of EOC/short fiber composites (a) as a function of short fiber loading (b) as a function of short fiber length

Table 4. Mixing characteristics of EOC/SF composites in Haake rheomix

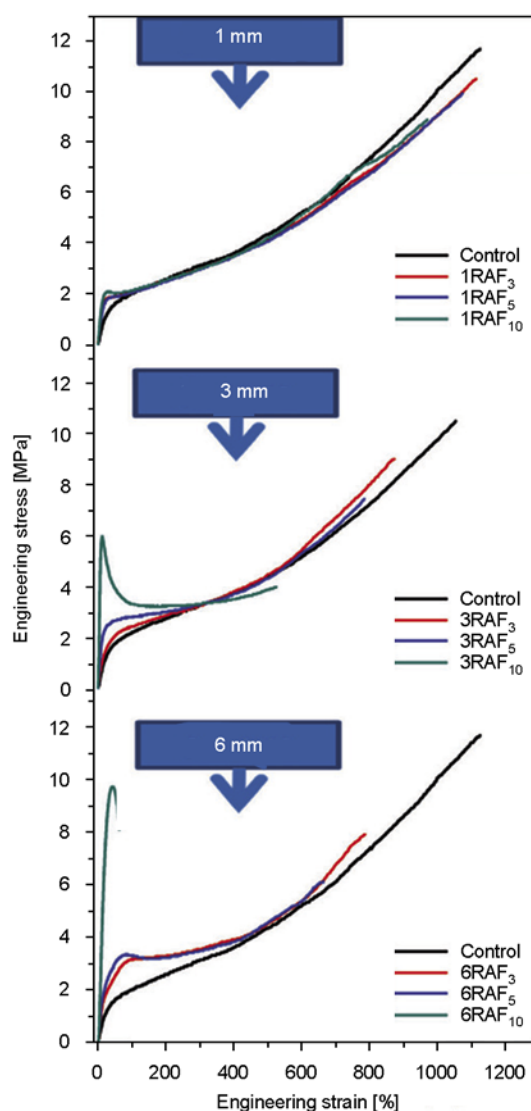
Mix code	Torque at 10 th minute [Nm]	Delta torque [Nm]	Melt temperature at dumping [°C]
Control	21.8	–	122.3
3RAF ₃	28.6	6.8	130.5
3RAF ₅	30.5	8.7	133.0
3RAF ₁₀	36.3	14.5	142.7
1RAF ₅	25.5	3.7	126.3
6RAF ₅	40.9	19.1	142.2

incorporation of dry fiber. As per the mixing sequence, the ram has to be open at the end of 1st, 2nd and 3rd minutes of mixing. Since the torque sensing is a continuous process throughout the mixing cycle, it shows a lower torque at these points. The mixing torque starts to stabilize immediately and shows a plateau region of nearly constant mixing torque after all the mixing sequence is over. The stabilized torque value of the polymer/fiber composite and the melt temperature were found to increase with increase in both short fiber loading and length. The torque is seen to increase progressively to approximately 67% of pure EOC when 10 phr of 3 mm short fiber is added to the matrix melt. At a constant loading of 5 phr, for 1, 3 and 6 mm short fibers the percentage rise of torque with respect to the pure EOC were 17, 40 and 88% respectively. This effect may be explained with the change in melt viscosity of the polymer fiber composite as a result of fiber addition. Fibers, when added into polymer melt tend to perturb the normal flow of the pure EOC melt by hindering the mobility of chain segments in flow [25]. This results in a fiber filled system with a higher melt viscosity than the pure polymer. Increasing the fiber content and aspect ratio (here aspect ratio varies only because of increased fiber length) further restrict polymer flow which leads to an increased viscosity of the EOC/short fiber suspension. Since viscosity is directly related to torque (at constant temperature and rotor speed), it requires higher torque for compounding. The increase in the melt temperature with increase in short fiber loading and length can be thought of frictioning between the fiber and the polymer and between fibers during the shear mixing.

3.1. Mechanical properties of the composites

(a) Effect of short fiber length and loading

Fiber length, more precisely the aspect ratio of the fiber (ratio between the length and diameter of the fiber) and its concentration are some of the most important parameters controlling the mechanical properties of the composites. Fiber length influences the extent of load transfer from matrix to fiber. The minimum fiber length at which the extent of load transfer is maximum is called the critical fiber length. If the fiber length is less than the critical fiber length, the stress transfer from the matrix to the fiber will not be effective as a result the reinforcement will be insufficient. On the other hand, if the fiber length is greater than the critical fiber length, the shear stress transfer across the interface

**Figure 2.** Stress-strain curves of EOC/short fiber composite as a function of fiber loading and length

from matrix to the fiber will build up sufficient tensile stress in the fiber to its tensile strength leading to fiber fracture. Furthermore, the high length fibers may undergo entanglement with each other causing aggregate lumps of fibers which act as stress concentrated points, as a result the stressed composite leads to a low strain failure or brittle failure [26–28]. The stress-strain behavior and the corresponding tensile properties such as tensile strength, elongation at break, Young’s modulus, low strain modulus (10%) and high strain modulus (100%) as a function of short fiber length and loading are displayed in Figure 2 and Table 5 respectively. Pristine EOC shows a stress-strain curve with a strain hardening effect [29, 30]. Addition of 1mm short fiber, even at a loading of 10 phr does not make any impact of the inherent strength and modulus of the short fiber on EOC matrix. In other words, incorporation of 1mm short fiber does not alter the original deformation behavior of the neat EOC to a greater extent. This means that Technora is not effectively reinforcing the EOC matrix at a fiber length of 1mm even at a concentration of 10 phr. This may be due to the insufficient stress transfer from matrix to fiber because of the low aspect ratio of the fiber (average aspect ratio of 1 mm short fiber is only 96) and the inability to make a pronounced micromechanical interlocking between the fiber and the matrix [31]. With the addition of 3 mm short fiber

having an average aspect ratio of 275, impart a significant improvement in low strain modulus at a fiber loading of 10 phr. The deformation behavior of 10 phr 3 mm fiber loaded composite shows different characteristics regions such as a well pronounced linear elastic region; a yielding followed by a drop in stress, a short plastic deformation region followed by an increase in stress and finally fracture. This is a synonymous stress strain behavior of a semi crystalline polymer. This can be attributed that as the aspect ratio of the fiber increases, there is a possibility of more mechanical interlocking between the fiber and the polymer. As a result of this higher force is required to cause an initial deformation which is responsible for the high stress value in the low strain region. The moment at which the disentanglement occurs between the polymer and the short fiber beyond the yield point it experiences a sudden drop in the stress. The orientations of the short fibers in the direction of force at higher deformation are responsible for the further increase in the stress. In other words, 3 mm short fiber even at a loading of 10 phr allows the inherent onset of strain hardening behavior of the virgin EOC matrix at high deformation (greater than 300%). Incorporation of 6mm short fiber with an average aspect ratio of 550 also exhibit more or less similar kind of deformation behavior as in the case of 3 mm fiber loaded composite up to a fiber loading of 5 phr.

Table 5. The mechanical properties of the RFL coated short fiber/EOC composites as a function of fiber length and loading in natural condition (witout any fiber orientation)

Sample ID with mill direction		TS [MPa]	Elongation [%]	M 10% [MPa]	M 100% [MPa]	Young’s modulus [MPa]	Hardness [Shore A]
Control		10.9±0.6	1132±65	0.55±0.06	2.1±0.08	4.7±0.3	77±0
1RAF ₃	L	10.1±0.5	1020±65	0.67±0.04	2.2±0.05	5.7±0.9	81±1
	T	9.9±0.7	1040±58	0.69±0.03	2.1±0.03	5.9±0.8	
1RAF ₅	L	9.6±0.7	1083±21	1.10±0.08	2.1±0.06	9.0±0.9	84±1
	T	9.4±0.6	1062±31	1.21±0.10	2.2±0.05	8.9±0.8	
1RAF ₁₀	L	9.0±0.9	1056±75	1.40±0.07	2.3±0.14	11.1±1.3	89±2
	T	8.9±0.8	1040±60	1.30±0.04	2.4±0.09	10.8±1.4	
3RAF ₃	L	8.9±0.3	860±32	0.83±0.20	2.5±0.08	8.2±0.06	83±1
	T	9.0±0.3	863±27	0.86±0.04	2.5±0.09	11.7±1.0	
3RAF ₅	L	8.1±0.7	810±24	1.67±0.16	2.7±0.08	17.2±2.6	86±1
	T	8.5±0.6	792±47	1.42±0.91	2.7±0.08	21.2±1.5	
3RAF ₁₀	L	5.8±0.8	595±97	5.10±0.46	3.6±0.14	53.0±3.7	92±2
	T	5.9±0.9	615±87	4.70±0.80	3.5±0.21	48.4±4.2	
6RAF ₃	L	7.8±0.6	745±49	0.91±0.04	2.8±0.09	11.2±3.0	83±1
	T	7.5±0.5	730±38	0.93±0.07	3.0±0.07	13.4±2.5	
6RAF ₅	L	6.9±0.9	662±43	1.20±0.10	3.3±0.07	19.0±3.5	88±2
	T	7.1±0.9	640±61	1.40±0.16	3.2±0.07	22.6±2.7	
6RAF ₁₀	L	9.8±0.9	57±21	5.60±0.82	–	67.0±5.1	94±2
	T	5.2±0.7	120±28	5.80±1.20	4.2±0.92	56.0±4.5	

However, at 10 phr fiber loading, it shows a steep rise in the stress at a low strain level (20%). This steep rise in stress at low strain level at 10 phr of fiber loading compared to 1 and 3 mm fiber loaded composites can be attributed to the fact that more efficient stress transfer is taking place in the case of 6 mm short fiber filled composite. However, the fiber aggregates developed in the composites due to the improper fiber dispersion of the 6mm fiber act as a point of weakness which leads to a brittle kind of failure by the application of strain.

(b) Effect of fiber orientations

The performance of any short fiber reinforced polymer composite is depend upon the extent of fiber orientations. The efficiency of stress transfer is higher if the fibers are oriented parallel to the direction of application of force [32]. The tensile properties of a 10 phr loaded composites in longitudinal (L) and transverse (T) directions as a function of fiber length is shown in Table 6. The orientation effect of low fiber loaded composites are not considered here because, at low fiber loading, though they are oriented in the flow direction when they are allowed to pass through a 2 mm extrudate die as shown in Figure 3, the fibers can easily move around and lose their orientations during mold flow in the molding operations. Since the movement of fiber is restricted at high fiber loading during com-

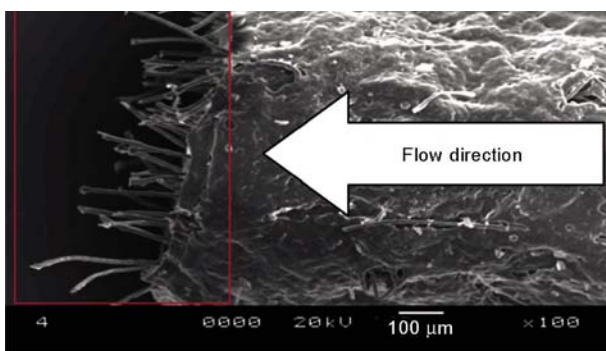


Figure 3. SEM Photomicrograph of the cross sectional view of the extrudate of a 5 phr 3 mm short fiber filled composite

pression molding, the percentage orientation will be more in high fiber loaded composite. The optical micrograph of a 3 mm 5 phr and 10 phr loaded composites are shown in Figure 4a–d gives qualitative information of fiber orientation of the composite in their natural and sheared condition respectively. The mechanical properties displayed in Table 6, it is clear that 1mm fiber does not make much impact on the properties due to poor orientation where as 3 and 6 mm fiber loaded composite, the properties such as tensile strength, low strain modulus and Young’s modulus were always higher in longitudinal direction than the composites with transverse fiber orientations.

(c) Effect of MA-g-PB

The behavior and performance of a short fiber/polymer composite cannot be explained only in terms of the specific properties of its components such as the fiber and the matrix. The interface that exists between the fiber and the matrix is also a main component of the composite. A strong interfacial adhesion between fiber and matrix is a precondition for transfer load from matrix to fiber. An extremely weak fiber/matrix interface may result in complete fiber interfacial debonding and pullout, producing a significant loss in composite strength with no or minimal improvement in composite toughness [33–35]. From the analyses of the mechanical properties of EOC/Short fiber composites, it is understood that the tensile strength and break elongation of the composite decreases as a function of fiber loading. This may be due to the inability to form a good interface between the fiber and the EOC matrix due to a huge polarity mismatch between the two. A drastic decrease in the break elongation and a brittle kind of failure at a very low strain in the case of a 10 phr 6 mm fiber loaded composite may be due to the aggregate formation because of the fiber entanglement at higher fiber loading. In order to find a solution for both the poor interfacial adhesion between the EOC and the fiber and the poor fiber

Table 6. Mechanical properties of 10 phr short fiber loaded composites in sheared condition (after orientations)

Sample ID	1RAF ₁₀		3RAF ₁₀		6RAF ₁₀	
	L	T	L	T	L	T
TS [MPa]	9.2±0.9	8.6±0.4	8.5±0.3	7.1±0.4	10.2±0.6	6.8±0.4
EB [%]	1075±31	1150±26	705±23	811±24	82±18	101±22
M 10% [MPa]	1.4±0.06	1.0±0.03	7.9±0.5	4.5±0.4	8.9±0.03	4.4±0.06
M 100% [MPa]	2.5±0.16	2.1±0.09	3.8±0.14	3.1±0.24	–	3.8±0.09
E modulus [MPa]	13±2.3	10±1.8	64±6.0	43±8.3	84±6.0	48±8.3

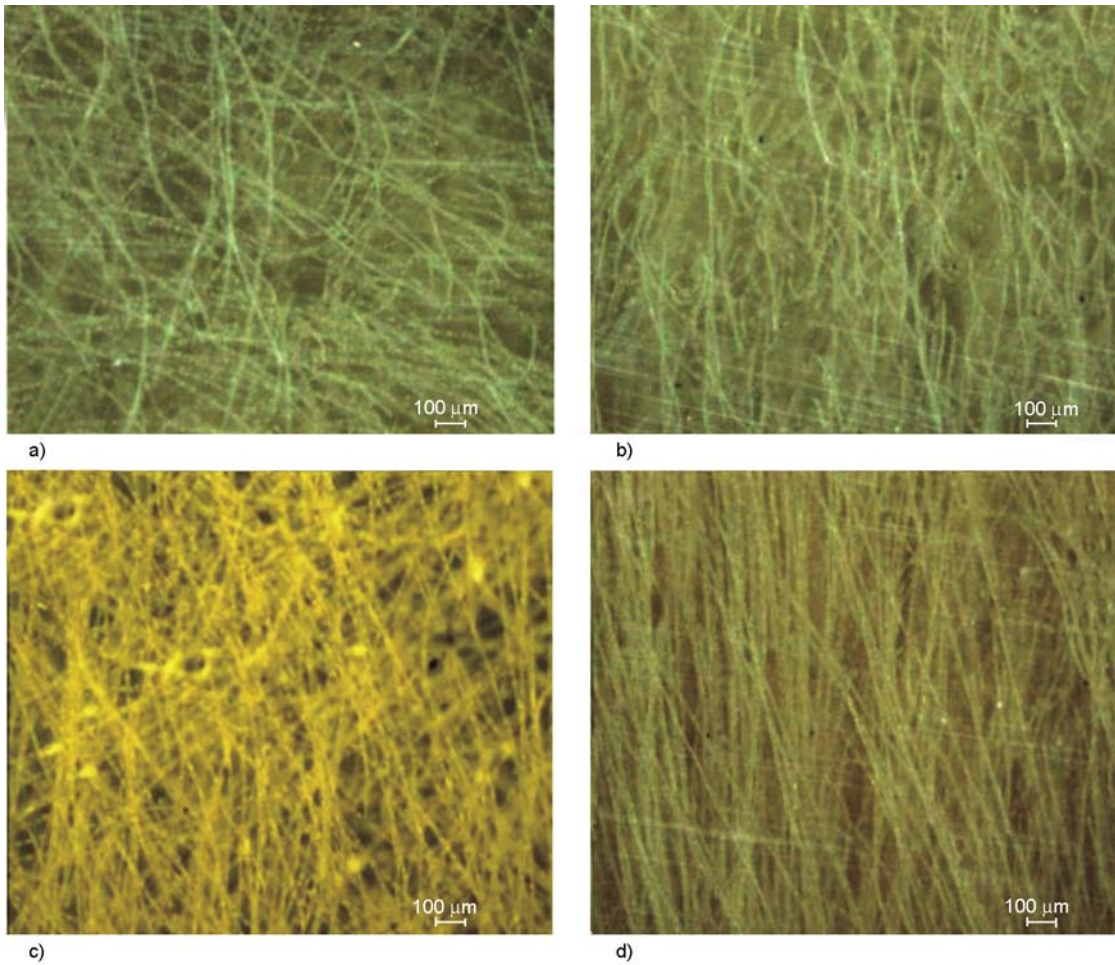


Figure 4. Optical micrographs of 3 mm 5 phr and 10 phr loaded molded composites (a) and (c) before orientations and (b) and (d) after orientation. The scale bar shown here is 100 μm.

dispersion of 6 mm fiber at higher loading, we used MA-g-PB as a multifunctional dispersing agent. Lai *et al.* have explored the use of this as a compatibilizing agent to enhance interface interaction in nylon-6/ABS blends [36, 37]. From our earlier communication, we have done an optimization of the level of MA-g-PB based on the mechanical properties as 3 phr. The tensile stress vs strain plot of 10 phr 6 mm short fiber loaded composite before and after the addition of a 3 phr MA-g-PB is shown in Figure 5. From the figure it is clear that addition of MA-g-PB increases the area under the stress-strain curve by concomitantly increasing the ultimate tensile strength and the percentage break elongation without affecting Young’s modulus. This observation suggests the potential use of MA-g-PB as an impact modifier to dissipate greater amount of energy before failure in the case of high length (6 mm) and high fiber loaded composite. It has also been observed that incorporation of MA-g-PB

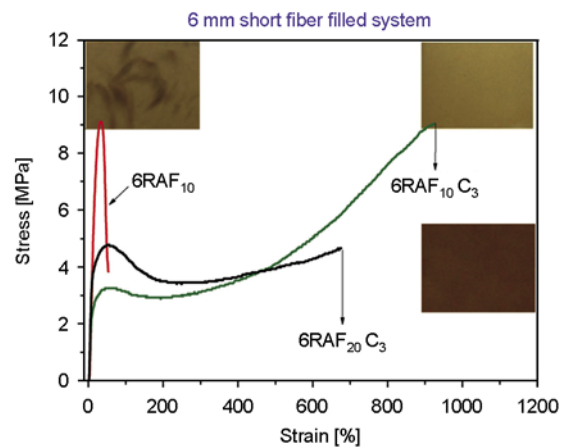


Figure 5. Stress-strain curves of 10 phr 6mm short fiber loaded composite (6RAF₁₀), 6 mm 10 phr short fiber loaded composite with 3 phr MA-g-PB (6RAF₁₀C₃) and 6 mm 20 phr short fiber loaded composite with 3 phr MA-g-PB (6RAF₂₀C₃)

tremendously improves the quality of fiber dispersion in the matrix as evidenced from the molded composite (shown as insets in Figure 5) which was

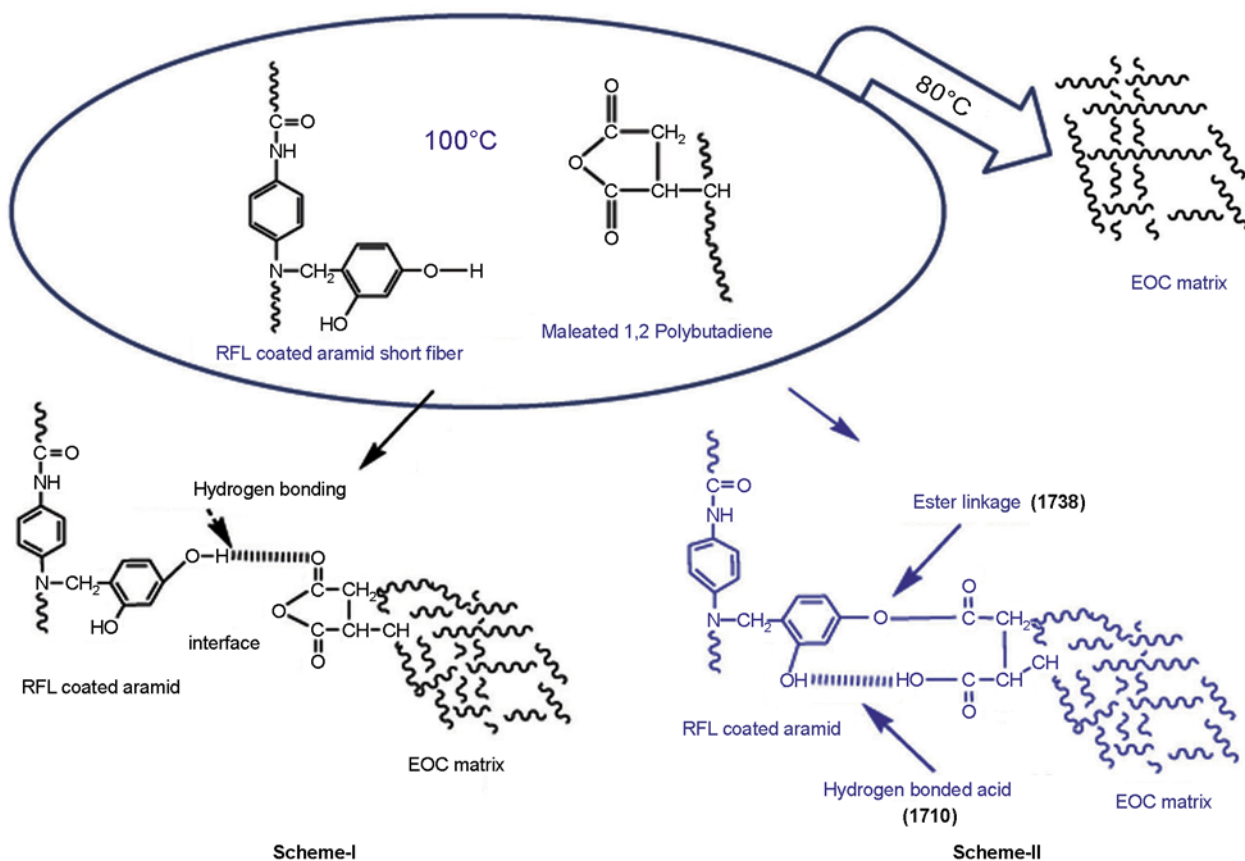


Figure 6. Plausible interaction mechanisms between MA-g-PB with RFL coated aramid fiber and the EOC matrix. Scheme I: Formation of H-bonding and Scheme II: Formation of ester linkages.

totally free from any kind of fiber aggregation to act as a stress concentrated points or failure points. A high quality of fiber dispersion could be easily achieved even in the case of a 20 phr 6 mm fiber loaded composite. This uniform fiber dispersion could be one of the reasons for the improved tensile strength and elongation. Since the intake of 6 mm fiber loading gets enhanced with MA-g-PB without any dispersion problem, the toughness to stiffness balance of the composite can also be maintained with higher fiber loading, which is evident from the stress-strain behavior of 20 phr fiber loaded composite with only 3 phr MA-g-PB shown in Figure 5. The enhancement in tensile strength coupled with elongation and a uniform fiber dispersion of the composites clearly indicate that the use of MA-g-PB promotes the interfacial interaction. Figure 6 scheme I demonstrates one of the plausible expected interaction mechanism between the RFL coated aramid fiber and maleic anhydride adducted 1, 2 polybutadiene. It is believed that the butadiene segment (non polar) of MA-g-PB forms a compati-

ble blend with the bulk EOC and the polar anhydride via the formation of H-bonds with the hydroxyl groups on the coated fibers and therefore forms a bridge at the interface between the two. This interface interaction enhances the stress transfer from the matrix to the fibers leading to higher tensile strength.

3.2. Fourier transform infrared spectroscopy (FTIR)

FTIR spectroscopy was used to explore the detailed chemical modification involved between RFL coated aramid fiber and MA-g-PB. Figure 7 shows the FTIR spectrum of (a) MA-g-PB, (b) RFL coated fiber and (c) MA-g-PB treated RFL coated fiber. The inset picture indicates an enlarged view between the frequency ranges of 1500 to 2000 cm^{-1} . The characteristics bands correspond to the symmetrical (1775 cm^{-1}) and asymmetrical (1825 cm^{-1}) stretching frequencies generated from the $-\text{CO}-$ group of the anhydride part of MA-g-PB as shown in Figure 7a. These peaks were found disappearing with the formation of new peaks at 1710 and 1737 cm^{-1}

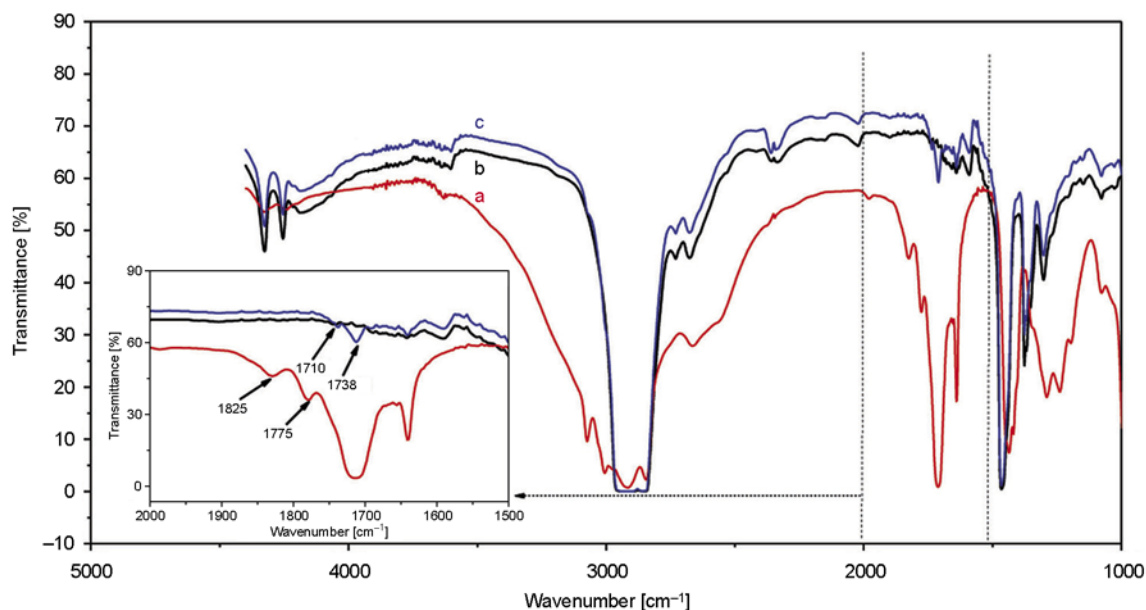


Figure 7. FTIR spectra of (a) pure MA-g-PB (b) RFL coated aramid short fiber (c) RFL coated aramid short fiber treated with MA-g-PB

when it was treated with RFL coated aramid fiber at 100°C . The peaks at 1710 cm^{-1} indicate the hydrogen bonded acids and the peaks at 1737 cm^{-1} indicates the ester carbonyl groups [38]. Based on this FTIR result a new reaction mechanism is proposed as shown in scheme II of Figure 6. It is believed that when MA-g-PB is treated with RFL coated aramid fiber at 100°C , the anhydride group of which gets converted into an ester by reacting with the hydroxyl group from the RFL coated fiber. A similar kind of interaction mechanism was reported by Liu and Dai [39] between jute fiber and MA-g-PP emulsion. According to the expected mechanism shown in scheme I, if there is any H-bonding which exists between the functionalized fiber and the MA-g-PB; the $-\text{CO}-$ stretching frequencies of the anhydride group should have been shifted to a lower frequency side by a maximum of 5 to 10 cm^{-1} . The non-occurrence of such a possibility may be due to the pronounced reaction as shown in scheme II and the difficulty in detect and distinguish the same due to very low concentration of MA-g-PB being used [40].

3.3. SEM analyses

In order to have a clear understanding of the effect of MA-g-PB on fiber dispersion in the matrix and its interface modifying effect for the improvement in tensile properties, the morphological analyses of the tensile fractured surface of a 6 mm 10 phr loaded

composite with and without MA-g-PB were performed under different magnifications. Figure 8a shows the distribution of fibers in the matrix without any MA-g-PB and Figure 8b shows the same with 3 phr of MA-g-PB. It is evident from the Figure 8a that the fibers were bunched together and agglomerate in the composite. An enlarged view of a portion of Figure 8a clearly indicates that some fibers get fibrillated at the fiber end to form tiny hair like fibers during shear mixing, which act as a twine to bind other fibers together and makes aggregate lumps [41]. This results the formation of some big voids on the matrix due to fiber pullout which leads to a brittle kind of failure of the composite when strain is applied. On the other hand, from Figure 8b it is clear that after the addition of MA-g-PB, the fibers are evenly distributed in the matrix without any severe fiber aggregation. An enlarged view of a portion from Figure 8b, it is understood that, the MA-g-PB chemically bound on the fiber surface acts as a lubricant between the stiff fibers which reduces the friction between the fiber during shear mixing and enhance the wetting to disperse fibers more easily and evenly into the polymer matrix. In this case no fibrillation was observed causing any fiber aggregation. To understand the effectiveness of MA-g-PB as an interface modifying coupling agent, analyses were done on the proximal end of the fiber that is buried in the matrix which is in the process of pulling out from the matrix. Figure 9a shows one

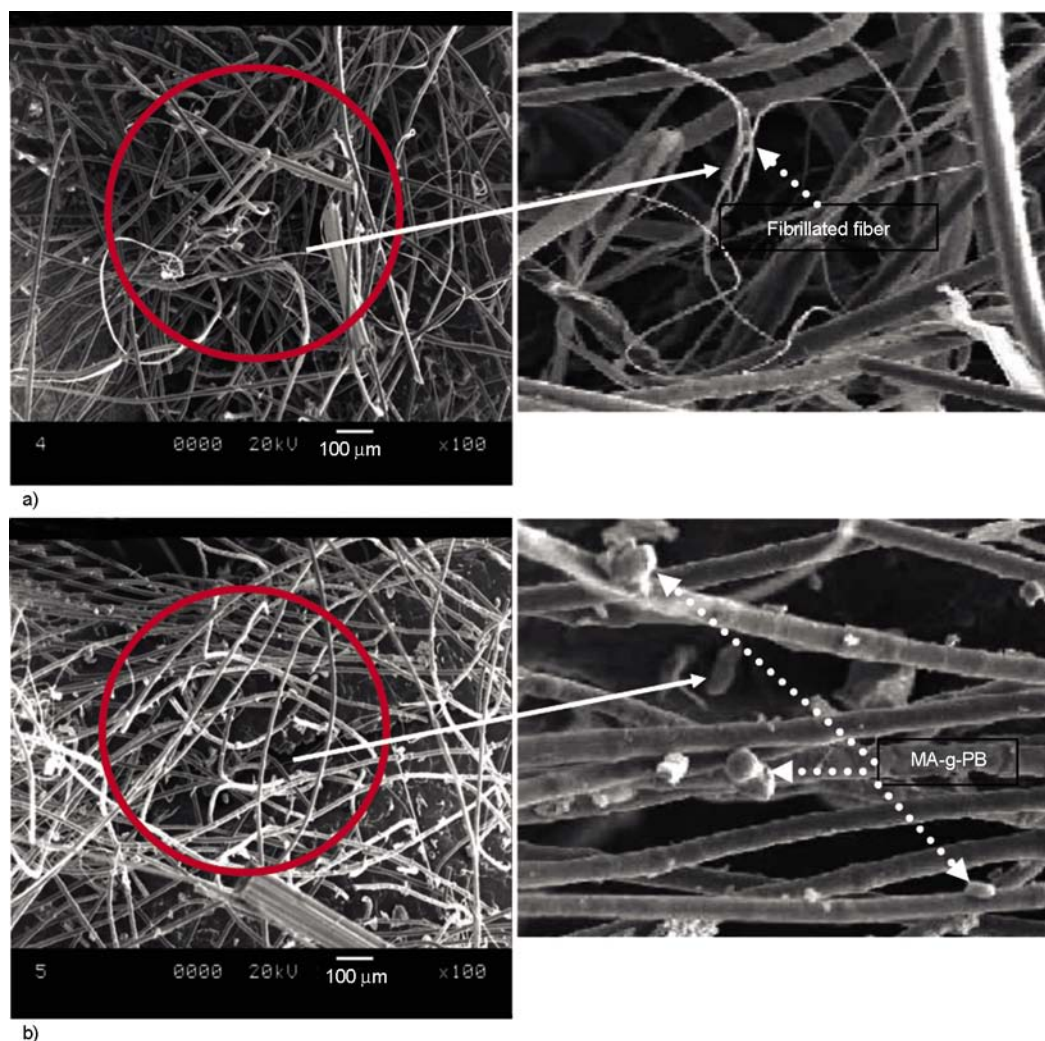


Figure 8. SEM photomicrograph of tensile fractured surfaces of 10 phr 6mm short fiber loaded composites (a) without any treatment (b) with 3 phr MA-g-PB

such picture without any MA-g-PB and Figure 9b with 3 phr of MA-g-PB. A clear debonding gap can be seen at the interface between the fiber and the matrix in composite without any modifier, whereas a tight interface between the fiber and the matrix is established after the addition of MA-g-PB. This SEM observation strongly supports the improved fiber dispersion during the mixing process and the enhancement in tensile properties encountered during the tensile testing.

3.4. Dynamic Mechanical Thermal Analyses (DMTA)

DMA is an effective tool to determine the viscoelastic parameter, such as dynamic storage modulus (E'), glass transition temperature (T_g) and damping ($\tan\delta$) characteristics of polymeric materials. Storage modulus is a measure of the maximum

energy stored in the material during one cycle of oscillation. The T_g is defined as the region where storage modulus increases with increasing frequency at a constant temperature or the temperature at which maximum of the $\tan\delta$ occurs. The ratio between the viscous modulus (E'') to storage modulus is termed as $\tan\delta$, which is normally used to quantify the dissipation of the viscoelastic material. Figure 10a and 10b show the variation of storage modulus (E') and the loss factor ($\tan\delta$) of neat EOC and its composite with a 3 mm aramid fiber having different concentrations as a function of temperature. It can be seen that the storage modulus of the composite is always higher than that of the neat matrix throughout the temperature range and is found to increase as the short fiber content increases. It is also evident from Figure 10b and Table 7 that the mechanical damping efficiency ($\tan\delta$) of the



Figure 9. SEM photomicrographs of tensile fractured surfaces of 10 phr 6 mm short fiber loaded composite at the interface region (a) without any treatment (b) treated with 3 phr MA-g-PB

composites decreases as the fiber loading increase. The increase in E' and the decrease in tan delta peak height can be attributed to the restricted mobility of the polymer chain by the stiff fibers due to the reinforcement imparted by the fibers to the EOC

matrix. To get more insight into the reinforcement of EOC with aramid short fiber, the variation of storage modulus and the relative or normalized storage modulus at various temperatures as a function of fiber loading were analysed and is displayed

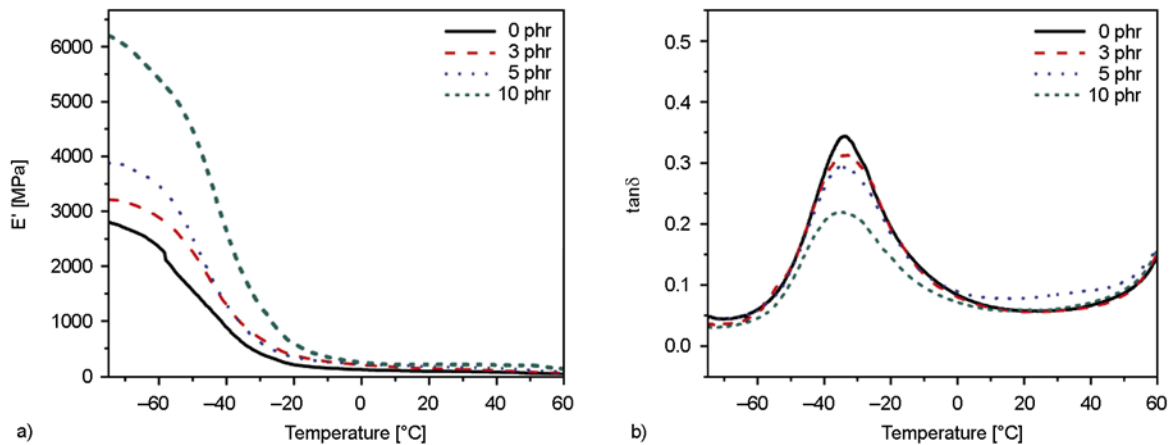


Figure 10. Dynamic mechanical properties of neat EOC and its composites with 3 mm short fiber as a function of fiber loading (a) storage modulus and (b) loss factor

Table 7. Dynamic mechanical properties of the composites as a function of fiber loading

Sample ID	T _g [°C]	Tanδ _{max}	E' at T _g [MPa]
Control	-33.7	0.34	531
3RAF ₃	-33.5	0.31	3169
3RAF ₅	-33.8	0.29	3226
3RAF ₁₀	-33.9	0.21	1697

Table 8. Variation of storage modulus and normalized (relative) storage modulus as a function of fiber loading at different temperature

Sample ID	T _i [°C]	T _{max} [°C]
Neat fiber	487	510
Neat matrix	376	442
3RAF ₃	397	453
3RAF ₅	408	461
3RAF ₁₀	421	466
1RAF ₅	409	463
6RAF ₅	410	463

in Table 8. From the table, it is clear that though the drop in modulus of the composite accelerates as the temperature increases, the relative or normalized drop in modulus decreases with increase in temperature. This may be due to the restriction of the polymer flow because of the fiber- matrix interaction. The effectiveness of Technora fiber on the improvement of storage modulus (*E'*) of EOC as a function of fiber loading was also evaluated on the basis of a coefficient 'C', using the Equation (1):

$$C = \frac{\left(\frac{E'_g}{E'_r}\right)_{comp}}{\left(\frac{E'_g}{E'_r}\right)_{resin}} \quad (1)$$

where *E'_g* and *E'_r* are the storage modulus values in the glassy and rubbery regions respectively [42, 43]. The base matrix used here is considered as the resin. The measured *E'* value at -33 and 20°C were used as *E'_g* and *E'_r* respectively. Generally the lower the value of the constant C, the higher is the effectiveness of filler as a reinforcing agent. In our system, the C value of EOC/SF composite obtained for different fiber loading is given in Table 8. Lowering of 'C' value as a function of fiber loading indicates the effectiveness of aramid fiber as reinforcing filler for EOC matrix. The lowest values of C at highest fiber loaded system indicates an efficient

stress transfer from the matrix to fiber at this concentration.

3.5. Thermal stability of the composites

The thermogravimetric analyses has been performed to understand the degradation and the ther-

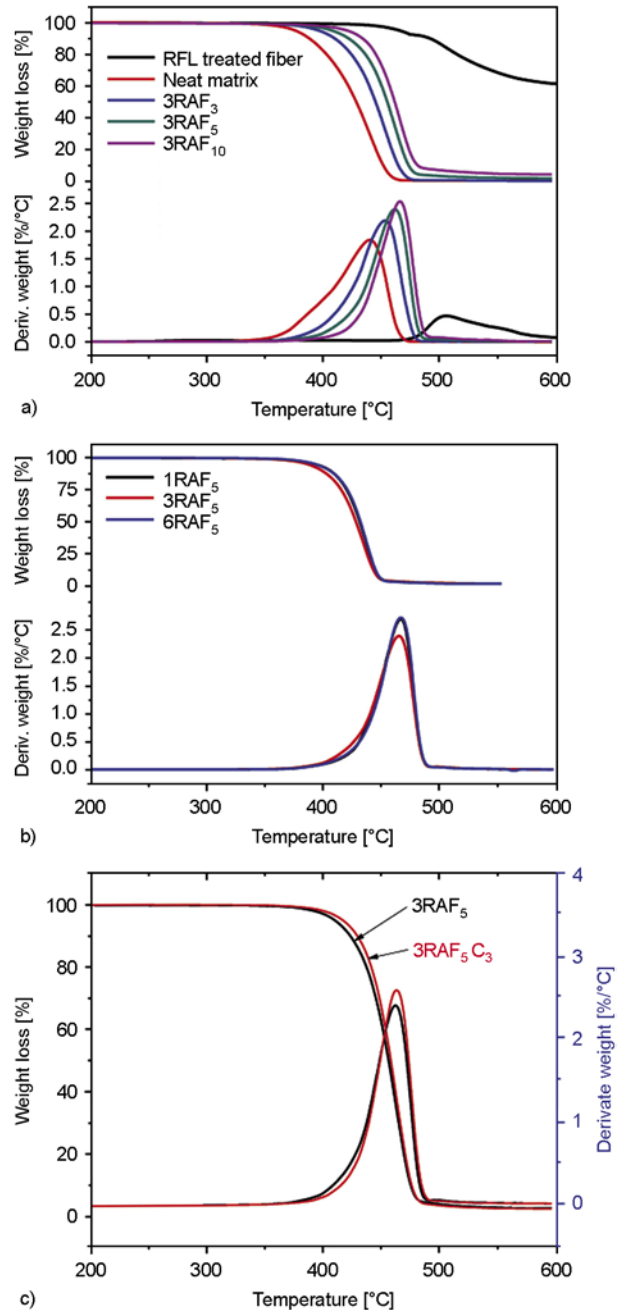


Figure 11. Thermogravimetric and the corresponding differential thermogravimetric curves (DTG): (a) neat EOC matrix, aramid fiber and its composites with 3 mm short fiber as a function of fiber loading (b) 5 phr short fiber loaded composites as a function of fiber length (c) 3 mm 5 phr loaded composite with 3 phr of MA-g-PB

Table 9. Thermogravimetric analyses of the composites as a function of fiber loading and length

Sample ID	Storage modulus (E') at various temperature [MPa]			Relative storage modulus (E_r') at various temperature [MPa]			C-value
	20°C	40°C	60°C	20°C	40°C	60°C	
Control	85	70	33	1	1	1	
3RAF ₃	128	98	48	1.5	1.4	1.45	1.02
3RAF ₅	168	140	69	1.97	2.01	2.10	0.85
3RAF ₁₀	208	196	126	2.44	2.80	3.81	0.84

mal stability of the composites as a function of short fiber loading and length. Figure 11a represents the thermogravimetric curves (TG) and the corresponding differential thermogravimetric curves (DTG) of neat EOC matrix, RFL dipped aramid short fiber and the composites of EOC/aramid fiber as a function of fiber loading at a fixed fiber length of 3 mm. The TG and DTG curves obtained for the composites as a function of short fiber length at a fixed fiber loading of 5 phr is given in Figure 11b. Single stage degradation peak was found in all the cases. Table 9 represents the onset of thermal degradation (T_i), maximum degradation temperature (T_{max}) and the maximum rate of degradation for the EOC/Sort fiber composite as a function of fiber length and loading. It is evident from the Table 9 that the point of onset of degradation of the neat EOC is shifted from 376 to 397°C with the addition of only 3 phr of short fiber and is further increased to 421°C at 10 phr fiber loading. Moreover, the maximum degradation temperature of EOC is also shifted to a higher temperature regime with the incorporation of the short fiber and is increased further as a function of fiber loading. These results confirm that the thermal stability of the EOC has been tremendously improved with the incorporation of short aramid fiber. This improvement in thermal stability can be attributed to the inherent high temperature stability of the aramid fiber and its reinforcing effect on EOC matrix. From the Figure 11b it is clear that variation of short fiber length does not have any significant influence on the thermal degradation behavior of the composite. The incorporation of the MA-g-PB (Figure 11) also doesn't make any significant changes in the thermal behavior of the composite.

4. Conclusions

EOC/short aramid fiber composites were developed with three different fiber lengths (1, 3 and 6 mm) and the mechanical and thermomechanical properties were evaluated in presence of an interface modifying coupling agent. From our observations and analyses the following conclusions can be drawn:

- (I) Incorporation of 1mm short fiber does not affect the original deformation behavior and the mechanical properties to a significant level; however, it offers good thermal stability.
- (II) 3 mm short fiber loaded composite shows an overall good balance in mechanical properties, fiber dispersion and the thermal properties at a fiber loading of 5 phr.
- (III) 6 mm short fiber loaded composite increases the stiffness and thermal stability of the composite by sacrificing the toughness due to severe fiber aggregation.
- (IV) The thermal stability of the composite increases with short fiber loading but, it is independent of fiber length.
- (V) The stress-strain behavior, FTIR analyses and the morphological studies of the tensile fractured surfaces of 6mm short fiber filled composite in presence of MA-g-PB strongly support its efficiency as a potential interface modifier as well as a fine dispersing agent for EOC/Short fiber composite. The intake of 6 mm fiber loading gets enhanced in presence of MA-g-PB without any dispersion problem. It can be used as an impact modifier to maintain the toughness to stiffness balance of the composite using higher fiber loading which is evident from the stress-strain behavior of 20 phr fiber loaded composite with only 3 phr of MA-g-PB.

Acknowledgements

The authors are thankful to Teijin Aramid BV, The Netherlands for providing the Technora short fibres.

References

- [1] Legge N. R., Holden G., Schroeders H. E.: Thermoplastic elastomer: A comprehensive review. Hanser, Munich (1987).
- [2] Jiri G. D.: Handbook of thermoplastic elastomers. William Andrew Publishers, Norwich (2007).
- [3] McNally T., McShane P., Nally G. M., Murphy W. R., Cook M., Miller A.: Rheology, phase morphology, mechanical, impact and thermal properties of polypropylene/metallocene catalysed ethylene 1-octene copolymer blend. *Polymer*, **43**, 3785–3793 (2002).
DOI: [10.1016/S0032-3861\(02\)00170-2](https://doi.org/10.1016/S0032-3861(02)00170-2)
- [4] Da Silva A. L. N., Rocha M. C. G., Coutinho F. M. B., Bretas R., Scuracchio C.: Rheological, mechanical, thermal, and morphological properties of polypropylene/ethylene-octene copolymer blends. *Journal of Applied Polymer Science*, **75**, 692–704 (2000).
DOI: [10.1002/\(SICI\)1097-4628\(20000131\)75:5<692::AID-APP12>3.0.CO;2-Y](https://doi.org/10.1002/(SICI)1097-4628(20000131)75:5<692::AID-APP12>3.0.CO;2-Y)
- [5] Svoboda P., Theravalappil R., Svobodova D., Mokrejs P., Kolomaznik K., Mori K., Ougizawa T., Inoue T.: Elastic properties of polypropylene/ethylene–octene copolymer blends. *Polymer Testing*, **29**, 742–748 (2010).
DOI: [10.1016/j.polymertesting.2010.05.014](https://doi.org/10.1016/j.polymertesting.2010.05.014)
- [6] Babu R. R., Singha N. K., Naskar K.: Interrelationships of morphology, thermal and mechanical properties in uncrosslinked and dynamically crosslinked PP/EOC and PP/EPDM blends. *Express Polymer Letters*, **4**, 197–209 (2010).
DOI: [10.3144/expresspolymlett.2010.26](https://doi.org/10.3144/expresspolymlett.2010.26)
- [7] Babu R. R., Singha N. K., Naskar K.: Studies on the influence of structurally different peroxides in polypropylene/ethylene alpha olefin thermoplastic vulcanizates (TPVs). *Express Polymer Letters*, **2**, 226–236 (2008).
DOI: [10.3144/expresspolymlett.2008.27](https://doi.org/10.3144/expresspolymlett.2008.27)
- [8] Chapleau N., Huneault M. A.: Impact modification of poly(ethylene terephthalate). *Journal of Applied Polymer Science*, **90**, 2919–2932 (2003).
DOI: [10.1002/app.13016](https://doi.org/10.1002/app.13016)
- [9] Aróstegui A., Nazábal J.: Super-toughness in compatibilized poly(butylene terephthalate)/poly(ethylene-octene) copolymer blends. *Polymer Engineering and Science*, **43**, 1691–1701 (2003).
DOI: [10.1002/pen.10143](https://doi.org/10.1002/pen.10143)
- [10] Uthaman N. R., Pandurangan A., Majeed S. M. A.: Blends of polyacetal end ethylene-octene elastomer: Mechanical, dynamic mechanical and morphological properties. *Journal of Polymer Research*, **14**, 441–447 (2007).
DOI: [10.1007/s10965-007-9126-6](https://doi.org/10.1007/s10965-007-9126-6)
- [11] Guerrica-Echevarría G., Eguiazábal J. I., Nazábal J.: Influence of compatibilization on the mechanical behavior of poly(trimethylene terephthalate)/poly(ethylene–octene) blends. *European Polymer Journal*, **43**, 1027–1037 (2007).
DOI: [10.1016/j.eurpolymj.2006.11.036](https://doi.org/10.1016/j.eurpolymj.2006.11.036)
- [12] Yu Z.-Z., Ou Y.-C., Hu G.-H.: Influence of interfacial adhesion on toughening of polyethylene–octene elastomer/nylon 6 blends. *Journal of Applied Polymer Science*, **69**, 1711–1718 (1998).
DOI: [10.1002/\(SICI\)1097-4628\(19980829\)69:9<1711::AID-APP4>3.0.CO;2-E](https://doi.org/10.1002/(SICI)1097-4628(19980829)69:9<1711::AID-APP4>3.0.CO;2-E)
- [13] De S. K., White J. R.: Short fiber polymer composites. Woodhead, Cambridge (1996).
- [14] Chantaratcharoen A., Sirisinha C., Amornsakchai T., Bualek-Limcharoen S., Meesiri W.: Improvement of interfacial adhesion of poly(*m*-phenylene isophthalamide) short fiber–thermoplastic elastomer (SEBS) composites by N-alkylation on fiber surface. *Journal of Applied Polymer Science*, **74**, 2414–2422 (1999).
DOI: [10.1002/\(SICI\)1097-4628\(19991205\)74:10<2414::AID-APP9>3.0.CO;2-V](https://doi.org/10.1002/(SICI)1097-4628(19991205)74:10<2414::AID-APP9>3.0.CO;2-V)
- [15] Ahamad I., Chin T. S., Cheong C. K., Jalar A., Abdullah I.: Study of fiber surface treatment on reinforcement/matrix interaction in twaron fiber/ENR composites. *American Journal of Applied Sciences (Special Issue)*, 14–20 (2005).
- [16] Mori M., Uyama Y., Ikada Y.: Surface modification of aramid fiber by graft polymerization. *Polymer*, **35**, 5336–5341 (1994).
DOI: [10.1016/0032-3861\(94\)90487-1](https://doi.org/10.1016/0032-3861(94)90487-1)
- [17] Amornsakchai T., Sinpatanapan B., Bualek-Limcharoen S., Meesiri W.: Composite of aramid fibre (poly-*m*-phenylene isophthalamide)-thermoplastic elastomers (SEBS): Enhancement of tensile properties by maleated-SEBS compatibiliser. *Polymer*, **40**, 2993–2999 (1999).
DOI: [10.1016/s0032-3861\(98\)00524-2](https://doi.org/10.1016/s0032-3861(98)00524-2)
- [18] Arroyo M., Bell M.: Morphology/behavior relationship and recyclability of composites based on PP/EPDM blends and short aramid fibers. *Journal of Applied Polymer Science*, **83**, 2474–2484 (2002).
DOI: [10.1002/app.10244](https://doi.org/10.1002/app.10244)
- [19] Kutty S. K. N., Nando G. B.: Short kevlar fiber-thermoplastic polyurethane composites. *Journal of Applied Polymer Science*, **43**, 1913–1923 (1991).
DOI: [10.1002/app.1991.070431016](https://doi.org/10.1002/app.1991.070431016)
- [20] Kutty S. K. N., Chaki T. K., Nando G. B.: Thermal degradation of short kevlar fibre thermoplastic polyurethane composite. *Polymer Degradation and Stability*, **38**, 187–192 (1992).
DOI: [10.1016/0141-3910\(92\)90113-J](https://doi.org/10.1016/0141-3910(92)90113-J)
- [21] Akbarian M., Hassanzadeh S., Moghri M.: Short twaron aramid fiber reinforced thermoplastic polyurethane. *Polymers for Advanced Technologies*, **19**, 1894–1900 (2008).
DOI: [10.1002/pat.1225](https://doi.org/10.1002/pat.1225)

- [22] Cerrada M. L., Benavente R., Pérez E.: Effect of short glass fiber on structure and mechanical behavior of an ethylene–1-octene copolymer. *Macromolecular Chemistry and Physics*, **202**, 2686–2695 (2001).
DOI: [10.1002/1521-3935\(20010901\)202:13<2686::AID-MACP2686>3.0.CO;2-L](https://doi.org/10.1002/1521-3935(20010901)202:13<2686::AID-MACP2686>3.0.CO;2-L)
- [23] Cerrada M. L., Benavente R., Pérez E.: Crystalline structure and viscoelastic behavior in composites of a metallocenic ethylene-1-octene copolymer and glass fiber. *Macromolecular Chemistry and Physics*, **203**, 718–726 (2002).
DOI: [10.1002/1521-3935\(20020301\)203:4<718::AID-MACP718>3.0.CO;2-S](https://doi.org/10.1002/1521-3935(20020301)203:4<718::AID-MACP718>3.0.CO;2-S)
- [24] Shibulal G. S., Naskar K.: RFL coated aramid short fiber reinforced thermoplastic elastomer: Mechanical, rheological and morphological characteristics. *Journal of Polymer Research*, **18**, 2295–2306 (2011).
DOI: [10.1007/s10965-011-9643-1](https://doi.org/10.1007/s10965-011-9643-1)
- [25] Akhtar S., De P. P., De S. K.: Short fiber-reinforced thermoplastic elastomers from blends of natural rubber and polyethylene. *Journal of Applied Polymer Science*, **32**, 5123–5146 (1986).
DOI: [10.1002/app.1986.070320530](https://doi.org/10.1002/app.1986.070320530)
- [26] Folkes M. J.: *Short fiber reinforced thermoplastics*. Wiley, New York (1982).
- [27] Chang A., Cheung Y. W., Hiltner A., Baer E.: Relationship of deformation behavior to thermal transitions of ethylene/styrene and ethylene/octene copolymers. *Journal of Polymer Science Part B: Polymer Physics*, **40**, 142–152 (2002).
DOI: [10.1002/polb.10066](https://doi.org/10.1002/polb.10066)
- [28] Tripathi D., Jones F. R.: Single fibre fragmentation test for assessing adhesion in fibre reinforced composites. *Journal of Materials Science*, **33**, 1–16 (1998).
DOI: [10.1023/A:1004351606897](https://doi.org/10.1023/A:1004351606897)
- [29] Androsch R., Stribeck N., Lüpke T., Funari S. S.: Investigation of the deformation of homogeneous poly(ethylene-co-1-octene) by wide- and small-angle X-ray scattering using synchrotron radiation. *Journal of Polymer Science Part B: Polymer Physics*, **40**, 1919–1930 (2002).
DOI: [10.1002/polb.10243](https://doi.org/10.1002/polb.10243)
- [30] Tarfaoui M., Choukri S., Neme A.: Effect of fibre orientation on mechanical properties of the laminated polymer composites subjected to out-of-plane high strain rate compressive loadings. *Composites Science and Technology*, **68**, 447–485 (2008).
DOI: [10.1016/j.compscitech.2007.06.014](https://doi.org/10.1016/j.compscitech.2007.06.014)
- [31] Jang J., Kim H.: Improvement of carbon fiber/PEEK hybrid fabric composites using plasma treatment. *Polymer Composites*, **18**, 125–132 (1997).
DOI: [10.1002/pc.10267](https://doi.org/10.1002/pc.10267)
- [32] Mathew L., Joseph R.: Mechanical properties of short-iora-fiber-reinforced natural rubber composites: Effects of fiber length, orientation, and loading; alkali treatment; and bonding agent. *Journal of Applied Polymer Science*, **103**, 1640–1650 (2007).
DOI: [10.1002/app.25065](https://doi.org/10.1002/app.25065)
- [33] Mahy J., Jennekens L. W., Grabandt O.: The fibre/matrix interphase and the adhesion mechanism of surface-treated Twaron® aramid fibre. *Composites*, **25**, 653–660 (1994).
DOI: [10.1016/0010-4361\(94\)90198-8](https://doi.org/10.1016/0010-4361(94)90198-8)
- [34] Mäder E., Freitag K-H.: Interface properties and their influence on short fibre composites. *Composites*, **21**, 397–402 (1990).
DOI: [10.1016/0010-4361\(90\)90437-2](https://doi.org/10.1016/0010-4361(90)90437-2)
- [35] Guigon M., Klinklin E.: The interface and interphase in carbon fibre-reinforced composites. *Composites*, **25**, 534–539 (1994).
DOI: [10.1016/0010-4361\(94\)90181-3](https://doi.org/10.1016/0010-4361(94)90181-3)
- [36] Lai S-M., Liao Y-C., Chen T-W.: The preparation and properties of compatibilized nylon 6/ABS blends using functionalized polybutadiene. Part I: Impact properties. *Polymer Engineering and Science*, **45**, 1461–1470 (2005).
DOI: [10.1002/pen.20428](https://doi.org/10.1002/pen.20428)
- [37] Lai S-M., Li H-C., Liao Y-C.: Properties and preparation of compatibilized nylon 6 nanocomposites/ABS blends: Part II – Physical and thermal properties. *European Polymer Journal*, **43**, 1660–1671 (2007).
DOI: [10.1016/j.eurpolymj.2007.02.009](https://doi.org/10.1016/j.eurpolymj.2007.02.009)
- [38] Rajput R. S., Rupainwar D. C., Sing A.: A study on styrene maleic anhydride modification by benzoic acid derivatives and dimethyl sulfoxide. *International Journal of Chemical Technology*, **4**, 915–919 (2009).
- [39] Liu X. Y., Dai G. C.: Surface modification and micro-mechanical properties of jute fiber mat reinforced polypropylene composites. *Express Polymer Letters*, **5**, 299–307 (2007).
DOI: [10.3144/expresspolymlett.2007.43](https://doi.org/10.3144/expresspolymlett.2007.43)
- [40] Zeng Z., Ren W., Xu C., Lu W., Zhang Y., Zhang Y.: Maleated natural rubber prepared through mechanochemistry and its coupling effects on natural rubber/cotton fiber composites. *Journal of Polymer Research*, **17**, 213–219 (2009).
DOI: [10.1007/s10965-009-9307-6](https://doi.org/10.1007/s10965-009-9307-6)
- [41] Hashimoto A., Satoh M., Iwasaki T., Morita M.: Fibrillation of aramid fiber using a vibrating ball mill and evaluation of the degree of fibrillation. *Journal of Materials Science*, **37**, 4013–4017 (2002).
DOI: [10.1023/A:1019696614997](https://doi.org/10.1023/A:1019696614997)
- [42] Praveen S., Chattopadhyay P. K., Jayendran S., Chakraborty B. C., Chattopadhyay S.: Effect of nanoclay on the mechanical and damping properties of aramid short fibre-filled styrene butadiene rubber composites. *Polymer International*, **59**, 187–197 (2010).
DOI: [10.1002/pi.2706](https://doi.org/10.1002/pi.2706)
- [43] Sreekumar P. A., Saiah R., Saiter J. M., Leblanc N., Joseph K., Unnikrishnan G., Thomas S.: Dynamic mechanical properties of sisal fiber reinforced polyester composites fabricated by resin transfer molding. *Polymer Composites*, **30**, 768–775 (2009).
DOI: [10.1002/pc.20611](https://doi.org/10.1002/pc.20611)